

DANISH METEOROLOGICAL INSTITUTE

———— **SCIENTIFIC REPORT** ————

03-01

**An Atmospheric Wave Optics
Propagator – Theory and Application**

**Hans-Henrik Benzon, Alan Steen Nielsen
and
Laust Olsen**



COPENHAGEN 2003

ISSN-Nr. 0905-3263
ISSN-Nr. 1399-1949 (Online)
ISBN-Nr. 87-7478-472-2

List of contents

1	Introduction	5
2	An Atmospheric Wave Propagator	6
2.1	<i>Coordinate Systems</i>	7
2.1.1	The J2000 Coordinate System	9
2.1.2	The Earth Frame	9
2.1.3	Geodetic Coordinates.....	10
2.1.4	Moving Occultation Plane Systems.....	10
2.1.5	Occultation Plane System.....	12
2.1.6	Unmoving GPS System	12
2.2	<i>Coordinate Transformations</i>	13
2.2.1	J2000 to Earth Frame.....	13
2.2.2	Earth frame to J2000.....	15
2.2.3	Geodetic to Earth Frame.....	15
2.2.4	Earth Frame to Geodetic Coordinate System.....	16
2.2.5	J2000 to Occultation Plane	17
2.2.6	Occultation Plane to Unmoving GPS System.....	19
2.3	<i>Initialisation of the Atmosphere Model/GRIB File.....</i>	20
2.4	<i>Atmospheric Refractivity</i>	20
2.5	<i>Determination of the Neutral Atmosphere Propagation Area</i>	22
2.6	<i>Ray Tracing in the Neutral Atmosphere</i>	24
2.7	<i>Wave Propagation from the GPS Satellite to the 1. Screen.....</i>	25
2.8	<i>Wave Propagation between the Screens in the Neutral Atmosphere.....</i>	26
2.9	<i>Wave Propagation from a Screen to the LEO Orbit.....</i>	33
3	Simulation Results	36
4	Validation of the Wave Propagator.....	41
5	Conclusion.....	58
5.1	<i>Acknowledgement.....</i>	58
6	Appendices	59
	Appendix A: Wave Propagation Flow Chart	59
	Appendix B: Coordinate Transformations.....	61
	Appendix C: GRIB Files	72
	Appendix D: Propagation Area in the Neutral Atmosphere	78
	Appendix E: Forward Propagation from the GPS Satellite to the First Screen..	79

Appendix F: Forward Propagation from the First to the Last Screen	80
Appendix G: Algorithm for Propagation between Two Non-Parallel Lines	83
Appendix H: Difference and relative difference plots.....	85
7 References	90

Abstract

In this report we present documentation and a specification of the algorithms defining a wave optics simulator tool as well as source code examples of the wave optic propagator. These project tasks and objectives are fully described in the ESTEC contract No. 15946/02/NL/SF.

We give a general description of radio wave propagation in the atmosphere and a specific description of a wave propagator developed by M.E. Gorbunov.

The forward wave optics propagator (WOP) is capable of including model atmospheric data and also real data from NWP analysis as a basis for the simulations.

The document is organised into 7 chapters: the first one contains the introduction, and the following chapter is a description of the wave propagator and a description of coordinate systems and transformations. We also discuss the atmospheric model (MSIS90), how to determine physical parameters and describe the equation behind ray tracing in the neutral atmosphere.

In chapter three we present simulation results of phase and amplitude from a wave propagator using an ECHAM GRIB file. The validation of the wave propagator is performed in chapter four while chapter five contains conclusion of the results under consideration.

Besides, the document is prolonged by a number of appendixes in chapter 6 that in more detail describe the algorithms used in the wave propagator.

Finally, the document is completed in chapter 7 with a list of references that has been used in this document.

1 Introduction

Ray Tracing is a very popular technique in computer graphics used for creating realistic pictures of scenes that have a defined 3-D structure. A multitude of imaginary rays are sent from the viewer through the screen and into the 3-D geometry. If a particular ray hits some object, the "imprint" of that object will appear on the screen at the place where the ray intersected it.

The atmospheric ray tracers based on geometrical optics give very realistic results in many cases. An atmospheric ray tracer is based on the geometrical optic approximation – the limiting form of Maxwell's equations when $\lambda \rightarrow 0$, which is only valid when the signal frequency is high and the density of the medium is low, and when we consider a reasonable smooth atmosphere. Furthermore, most ray tracers are based on an assumption of single ray propagation, i.e., multipath propagation is not taken into account. Multipath propagation occurs in the transition zone where the geometrical optics approximation is valid to non-validity of this approximation.

The atmosphere of the Earth can produce large gradients – both vertical and horizontal – that cause multipath propagation and also even total failure of the geometrical optics approximation. Large gradients most often occur in the lower troposphere in connection with inversion layers and water vapour. Water vapour is highly variable both vertically and horizontally whereas inversion layers primarily have large vertical gradients. Large vertical gradients can also occur around the tropopause. Extra information can be gained from the use of an atmospheric forward wave propagator based directly on the solution of the wave equation for

electromagnetic fields. The current propagator presented in this document is based on a two-dimensional wave propagation description, which is able to handle multipath situations.

Wave propagation in the atmosphere is based on the solution of the Helmholtz wave equation. In practice this can be done by solving the parabolic equation approximation of the Helmholtz wave equation. This approach applies a full wave, forward scatter model that is capable of predicting propagation of arbitrary atmospheric refractivities. The primary limitations of this technique are that it neglects the backscattered field, and accurate calculations are restricted to near-horizontal propagation directions.

In the following, the wave propagation will be described in detail. First, the theoretical derivation of the method will be given together with the theoretical limitations of the method. After this the algorithm description follows. These descriptions show how the methods can be implemented. Also some comments are given on where improvements/changes might be necessary depending on the context of application of the algorithms.

2 An Atmospheric Wave Propagator

The propagator makes use of a ray tracer in order to locate the area in which the field will propagate. The wave propagation in the troposphere/stratosphere is based on the waves propagating from a set of thin screens.

The forward wave propagation between the screens is based on the expansion of the field in a set of plane waves. This can be implemented using the fast Fourier transform (FFT) and thus significantly increasing the execution speed of the propagator. Spatial frequencies are used in the Fourier transform calculations. The wave propagator can, however, be improved in some areas. The split-step Fourier solution can be extended from the current 2-D version to a 3-D version. Furthermore, the standard parabolic equation used here can be substituted with a parabolic equation that is valid in a wider-angle span around the horizon.

Slower, but more accurate methods, such as the finite-difference method, can be used to propagate the electromagnetic wave between the screens in the neutral atmosphere. An alternative approach is to approximate the neutral atmosphere with (a leaky) wave-guide. The wave propagation in the neutral atmosphere can then be found from the electromagnetic mode theory.

The propagation of the wave from the last screen to the LEO orbit is performed using the 1-D version of the Fresnel diffraction integral. This is nearly the same integral used in the back propagation algorithm (Meincke 1998). The only difference is a change of the sign in the complex exponent. This will make the wave propagate in the opposite direction compared to the back propagation case. Figure 2.1 below summarises the different calculation steps performed by the atmospheric wave propagator. The following sections describe the equations needed to perform the calculations listed in the flowchart.

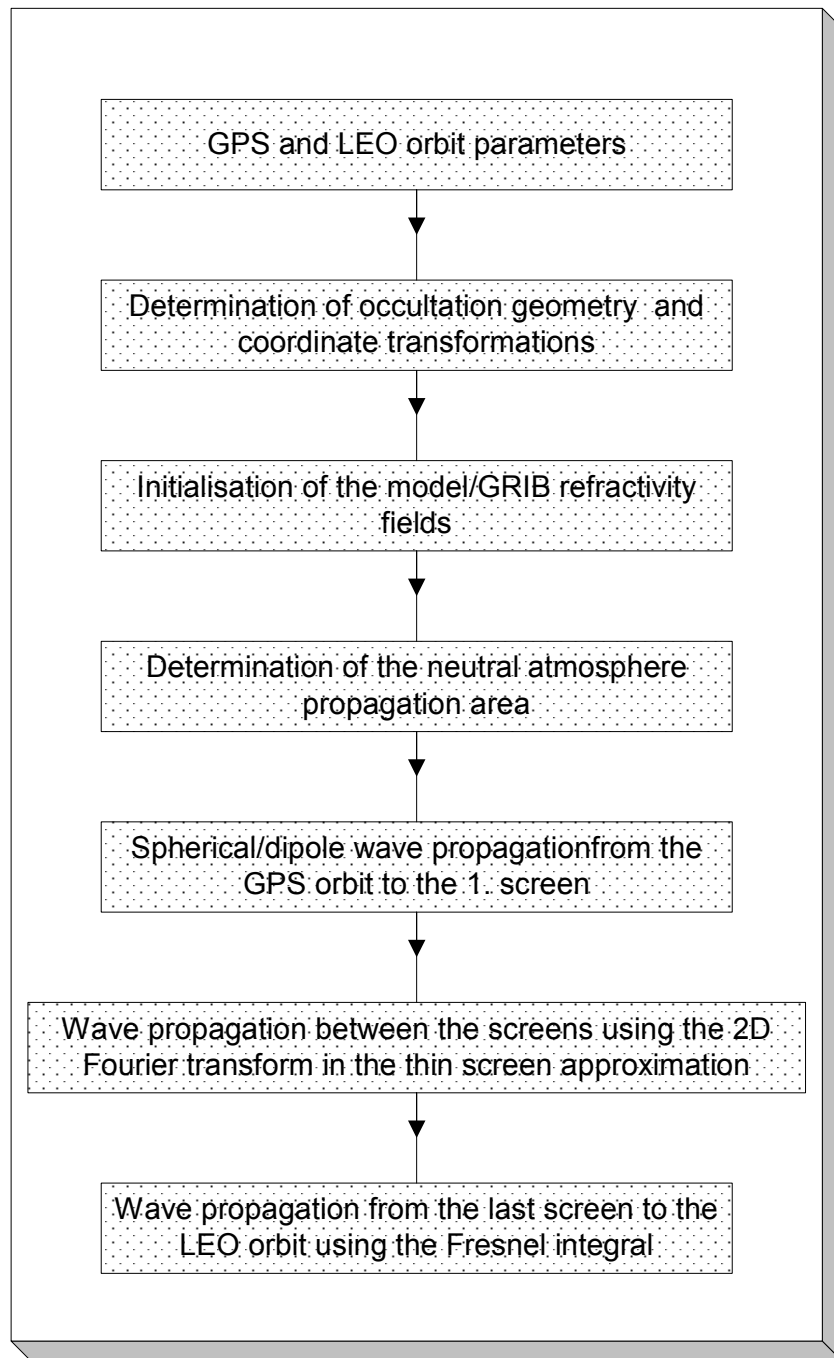


Figure 2-1: The large box shows the different calculation steps performed by the atmospheric wave propagator.

2.1 Coordinate Systems

Figure 2.2 below shows a schematic drawing of the occultation geometry (GPS and LEO orbits) and the positions of the thin screens, aligned with the Y-axis, in the neutral atmosphere. A spherical wave is assumed to propagate from the GPS to the 1.

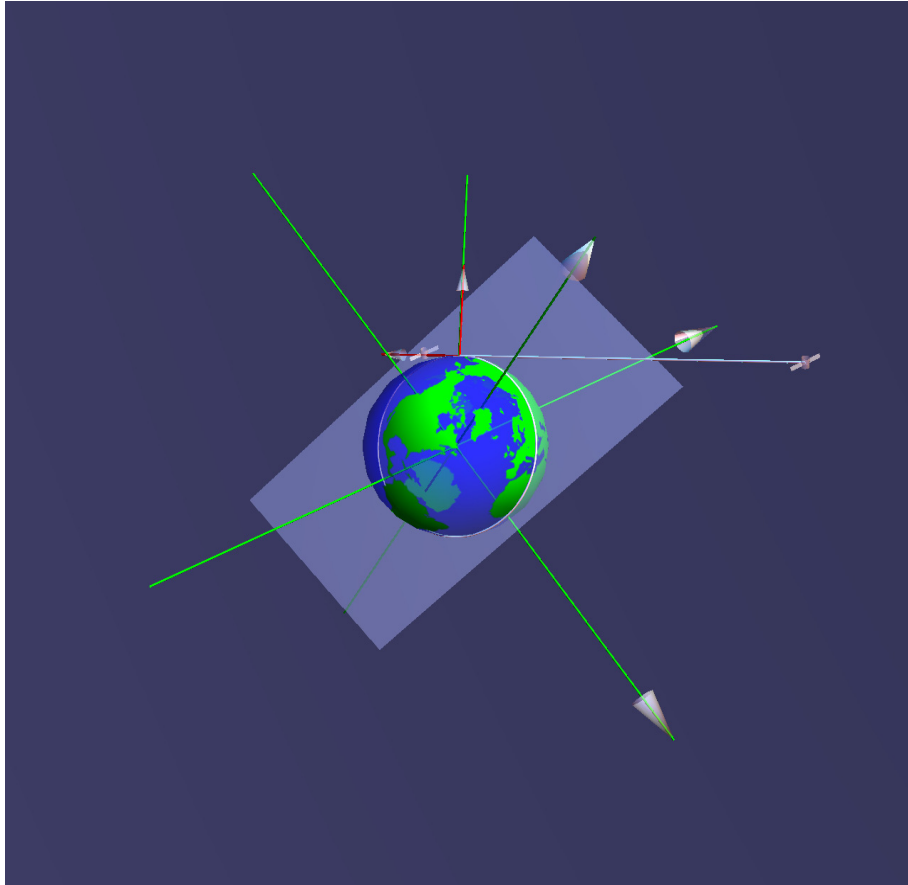


Figure 2-3: A 3-D view of the occultation geometry and the coordinate system used in the wave propagator. The LEO satellite is seen right above the surface boundary of the Earth and the GPS satellite is located to the right.

The following pages give, in a summarised form, a description of all the coordinate systems used in the wave propagator and the corresponding transformations. The goal is to get a 2-D coordinate system where the GPS satellite has zero velocity. This coordinate system describes the plane in which the occultation takes place.

We start out by listing all the used coordinate systems and describe how they are defined (see Appendix B for further details).

2.1.1 The J2000 Coordinate System

A Cartesian coordinate system fixed to the stars. Satellite positions are given relative to this coordinate system. The Z-axis coincides with the Earth's rotation axis, which is not perpendicular to the Earth's orbit. Instead, the Earth's axis is tilted 23.5 degrees away from the perpendicular. The Earth constantly maintains this tilted orientation as it orbits the Sun. The Origin is situated at the Earth's centre so that the X- and Y-axis span the equatorial plane.

2.1.2 The Earth Frame

A Cartesian coordinate system fixed to the centre of the Earth (see Figure 2.4). The Z-axis coincides with the Earth's rotation axis. The X-axis goes through the

Greenwich meridian and the Y-axis through 90 degrees east. The origin is situated at the Earth's centre so that the X- and Y-axis span the equatorial plane.

2.1.3 Geodetic Coordinates

A Geodetic Reference System is used (see Figure 2.4). The coordinates are geodetic latitude (angle between equatorial plane and reference ellipsoid surface normal at the point), longitude (angle between Greenwich meridian plane and meridional plane through the point) and height above reference ellipsoid (reckoned along the reference ellipsoid surface normal).

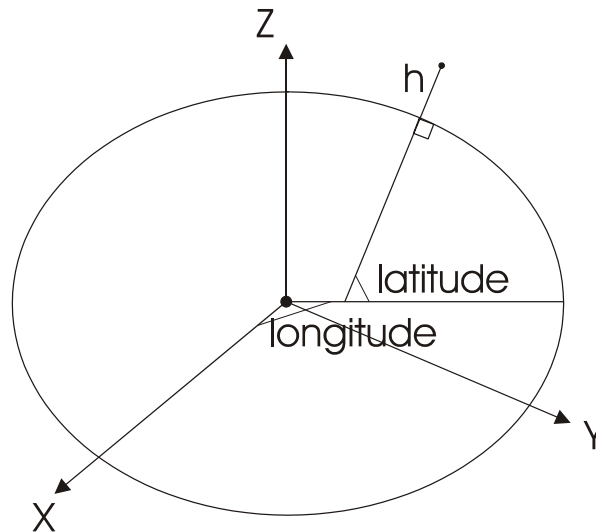


Figure 2-4: Cartesian fixed Earth frame and geodetic coordinates.

2.1.4 Moving Occultation Plane Systems

The two-dimensional occultation plane coordinate systems are based on a defined "occultation point" that is determined by the following procedure:

Assuming spherical symmetry of the Earth and zero refraction angle, then the ray perigees for each set of simultaneous satellite positions during an occultation is determined (that is the points closest to the centre of a spherical Earth of the straight lines between the GPS and LEO satellites). Note that since we approximate the ray paths by straight lines the perigee can be beneath the Earth surface (see Figure 2.5).

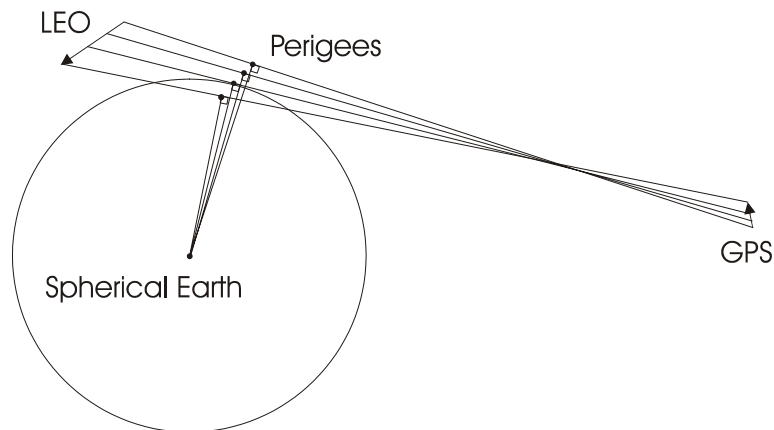


Figure 2-5: Occultation geometry.

Then the coordinates of all the points are transformed to geodetic coordinates and the point with smallest height above the reference ellipsoid (reckoned along the reference ellipsoid surface normal) is chosen. Again note that this height might be negative. The height of this point is set to zero and the new point is the occultation point (see Figure 2.6).

The whole problem is discretized by the sampling rate. Let us call the time index i and let it have the value i_{occ} at the time of smallest geodetic height.

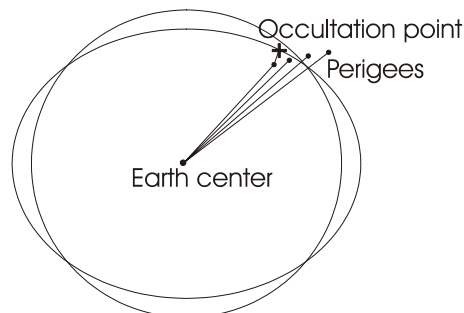


Figure 2-6: Nearest points of rays, perigees, and corresponding occultation point. Both the spherical Earth approximation and the reference ellipsoid are drawn.

The moving occultation plane contains the GPS and LEO satellites and the local curvature centre for the reference ellipsoid at the fixed occultation point. Since the satellites are moving the orientation of the plane relative to other coordinate systems changes during an occultation event. The moving occultation plane coordinate systems are orthogonal two-dimensional coordinate systems. Their origins are at the fixed local curvature centre.

The X-axis is approximately directed along the instantaneous GPS-occultation point line and is shown in Figure 2.7 as the AX vector. The Y-axis is directed approximately normal to the ellipsoid and is shown in Figure 2.7 as the AY vector.

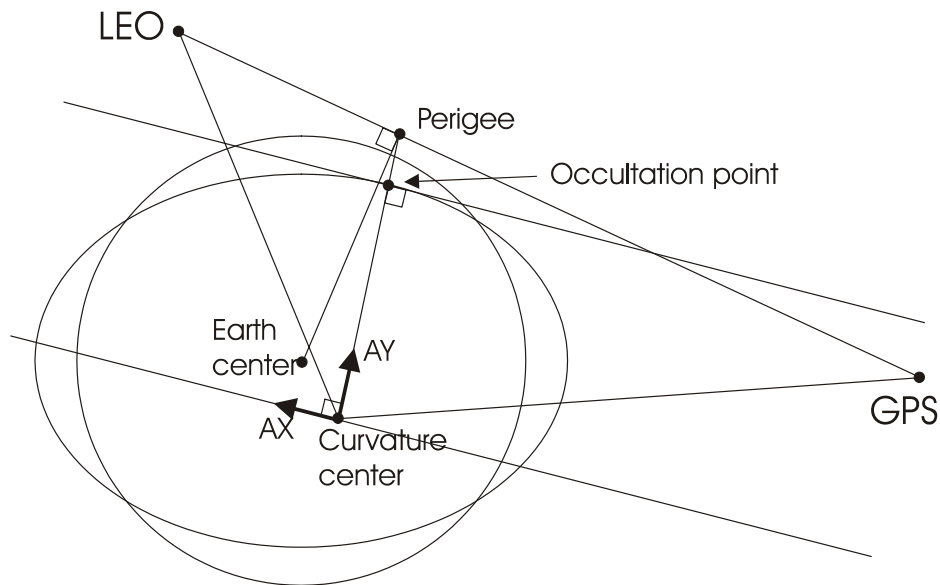


Figure 2-7: Two-dimensional occultation-plane coordinate system.

2.1.5 Occultation Plane System

The occultation plane coordinate system is the moving occultation plane system at the time $i = i_{occ}$ (see section 2.1.4).

2.1.6 Unmoving GPS System

Compared to the occultation plane system the zero of the Y-axis in the unmoving GPS coordinate system is translated by R_c , the local radius of curvature. The GPS satellite X-coordinate is set to the value it has at the time $i = i_{occ}$, i.e., when the ray traverses deepest into the atmosphere. The LEO X-coordinate is transformed in a way so that the total bending angle remains the same for a given impact parameter. The unmoving GPS system is sketched in Figure 2.8. The E_x basis vector is nearly parallel to the GPS-occultation point connection line which is nearly tangential to the ellipsoidal Earth. E_y is normal to E_x and directed outwards from the Earth and thereby nearly parallel to the local curvature radius vector. The only difference between (A_x, A_y) and (E_x, E_y) is a translation.

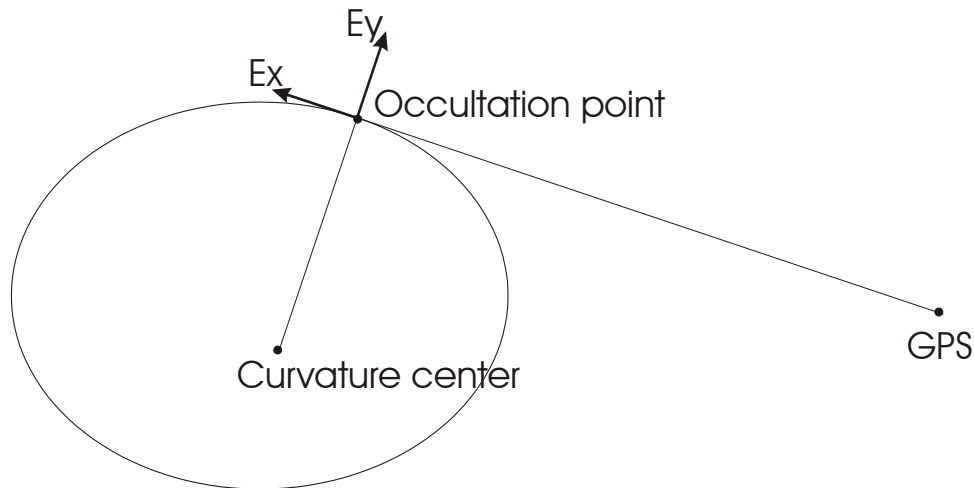


Figure 2-8: Unmoving GPS coordinate system. E_x is not exactly parallel to the tangent of the ellipsoid point.

2.2 Coordinate Transformations

The following sections explain the transformation matrices between the coordinate systems.

2.2.1 J2000 to Earth Frame

Since the Z-axis is common to both systems the transformation is a rotation about this axis. The rotation angle is found by converting Greenwich Apparent Sidereal Time (GAST) to an angle γ by the conversion factor $2\pi/86400$ [rad/s]. Sidereal time is based on the rotation of the Earth relative to space (the fixed stars) and is therefore equivalent to an angle. We anticipate in the context that GAST is approximately equal to Greenwich Mean Sidereal Time (GMST).

First, the Julian day (JD) number, which is the number of days elapsed since noon January 1, 4713 B.C in the Julian calendar, has to be calculated. This date is the same as -4712 January 1 since the chronology is 2BC, 1BC, 1AD, 2AD and -2, -1, 0, 1, 2. The following algorithm works for dates later than 1582 AD when Pope Gregory reformed the Julian calendar and introduced the Gregorian calendar. The operator $\text{int}[\]$ takes the integer part of the real number in the brackets. A date in the Gregorian calendar is represented as Y, M and DM corresponding to year, month and day-of-month number respectively. The first day in a month is day 1. If $M < 3$ then $Y1 = Y - 1$ and $M1 = M + 12$. If $M \geq 3$ then $Y1 = Y$ and $M1 = M$.

$$A = \text{int} \left[\frac{Y1}{100} \right] \quad (2-1)$$

$$B = 2 - A + \text{int} \left[\frac{A}{4} \right] \quad (2-2)$$

$$C = \text{int}[365.25 \cdot Y1] \quad (2-3)$$

$$D = \text{int}[30.6001 \cdot (M1+1)] \quad (2-4)$$

$$JD = B + C + D + DM + 1720994.5 \quad (2-5)$$

The parameter B is due to the rule of the Gregorian calendar that says that although divisible by 4, years divisible by 100 is not leap years unless they are also divisible by 400. The +2 constant in B corrects for the calendar revision in 1582 where 10 days were omitted and the above leap year rule was introduced.

The factor 30.6001 is an appropriate number that makes D exactly 63 bigger than the number of days from $Y1$ January day 1.5 to $Y1$ $M1$ day 1.5 where $M1=3,4,\dots,14$.

The constant 1720994.5 comes from the 1721058 days from -4712 January 1 noon to year 0 January 1 noon, minus 63 days that is counted too much in D , minus 1 day due to the convention that the first day in a month is designated 1 not zero, plus 1 day due to that the leap day in year 0 is not included in D , and at last -0.5 is due to the convention that JD is counted up to Greenwich noon, but we count up to the midnight before.

Then we can form the following parameter

$$T_u = \frac{JD - 2451545.0}{36525} \quad (2-6)$$

where the numerator is the number of days elapsed since JD 2451545, which corresponds to 2000 January 1, 12 hr UT1, and the denominator is the number of days in a century. T_u is then Julian centuries elapsed since 2000 January 1 noon.

Then GMST of 0h UT1 of the given day is given by the formula

$$\begin{aligned} \text{GMST of 0 h UT1} = & 24110.54841 + 8640184.812866 \cdot T_u \\ & + 0.093104 \cdot T_u^2 - 6.2 \cdot 10^{-6} \cdot T_u^3 \end{aligned} \quad (2-7)$$

which is counted in seconds. Then we have to add the contribution according to the time of day (tod) namely

$$\text{tod(UT1)} = \text{hour} \cdot 3600 + \text{minute} \cdot 60 + \text{seconds} + D \text{ sec} \quad (2-8)$$

where $D \text{ sec}$ is the time elapsed since the start of the occultation, and hour, minute and seconds denote the starting time of the occultation.

Universal time UT1 is approximately related to sidereal time by a constant conversion factor 1.0027379093 so that

$$\text{tod}(\text{sidereal}) = \text{tod}(\text{UT1}) \cdot 1.0027379093 \quad (2-9)$$

and since one mean sidereal day is defined as 24 sidereal hours (86400 seconds) GMST can be obtained as

$$\text{GMST} = \text{mod}(\text{GMST of 0 h UT1} + \text{tod}(\text{sidereal}), 86400) \quad (2-10)$$

Finally, GMST is converted into an angle

$$\gamma = \text{GMST} \cdot \frac{2\pi}{86400} [\text{rad} / \text{s}] \quad (2-11)$$

The transformation can be summarised in matrix notation as

$$\begin{pmatrix} x_E \\ y_E \\ z_E \end{pmatrix} = \begin{bmatrix} \cos \gamma & \sin \gamma & 0 \\ -\sin \gamma & \cos \gamma & 0 \\ 0 & 0 & 1 \end{bmatrix} \begin{pmatrix} x_{2000} \\ y_{2000} \\ z_{2000} \end{pmatrix} \quad (2-12)$$

2.2.2 Earth frame to J2000

The transformation from the Earth frame to J2000 is given by the inverse of Eq. 2-12 and can be written as

$$\begin{pmatrix} x_{2000} \\ y_{2000} \\ z_{2000} \end{pmatrix} = \begin{bmatrix} \cos \gamma & -\sin \gamma & 0 \\ \sin \gamma & \cos \gamma & 0 \\ 0 & 0 & 1 \end{bmatrix} \begin{pmatrix} x_e \\ y_e \\ z_e \end{pmatrix} \quad (2-13)$$

2.2.3 Geodetic to Earth Frame

The “radius of curvature in the prime vertical” rcp is given by

$$rcp = \frac{a}{\sqrt{1 - (2 - f)f \sin^2 \varphi}} \quad (2-14)$$

where f is the reference ellipsoid flatness, a is the major semi axis and φ is geodetic latitude. If λ is geodetic longitude and h is geodetic height the Earth frame coordinates are given by

$$x_E = \cos \varphi \cdot \cos \lambda \cdot (rcp + h) \quad (2-15)$$

$$y_E = \cos \varphi \cdot \sin \lambda \cdot (rcp + h) \quad (2-16)$$

$$z_E = \sin \varphi \cdot (rcp \cdot (1 - f)^2 + h) \quad (2-17)$$

Since this is a non-linear relationship it cannot be written in matrix form.

2.2.4 Earth Frame to Geodetic Coordinate System

There is no closed form of this transformation. φ , λ and h all have to be determined either by iteration or approximate formulas. We give an approximation method here. The longitude is given by

$$\lambda = \arctan\left(\frac{y_E}{x_E}\right) \quad (2-18)$$

We define some convenient parameters.

$$R_{xy} = \sqrt{x_E^2 + y_E^2} \quad (2-19)$$

$$\Theta = \arctan\left(\frac{z_E \cdot a}{R_{xy} \cdot b}\right) \quad (2-20)$$

then the latitude is

$$\varphi = \arctan\left(\frac{z_E + e \cdot b \cdot \sin^3 \Theta}{R_{xy} - e \cdot a \cdot \cos^3 \Theta}\right) \quad (2-21)$$

and with

$$\arg = (b^2 - z_E^2) \cos^2 \varphi + (a^2 - R_{xy}^2) \sin^2 \varphi + 2R_{xy} \cdot z_E \cos \varphi \sin \varphi \quad (2-22)$$

the height above the reference ellipsoid becomes (Gorbunov, private communication)

$$\vec{NL} = \frac{\vec{RLEO} - \vec{RLC} - \left((\vec{RLEO} - \vec{RLC}) * \vec{NG} \right) * \vec{NG}}{\left\| \vec{RLEO} - \vec{RLC} - \left((\vec{RLEO} - \vec{RLC}) * \vec{NG} \right) * \vec{NG} \right\|} \quad (2-25)$$

where $RLEO$ defines the LEO position vector. The local radius of curvature is given by

$$R_c = \frac{1}{\frac{\cos^2 \alpha}{rcm} + \frac{\sin^2 \alpha}{rcp}} \quad (2-26)$$

where α is the angle between geographic north and the occultation plane intersection with the local horizontal plane, and rcp and rcm are the parallel and meridian radii of curvature, respectively.

$$rcp = \frac{a}{(1 - e^2 \sin^2 \varphi)^{1/2}} \quad (2-27)$$

$$rcm = \frac{a(1 - e^2)}{(1 - e^2 \sin^2 \varphi)^{3/2}} \quad (2-28)$$

Here a is the major semi axis of the Earth, e is the eccentricity of the Earth and φ is the geodetic latitude. Now an approximation of the geometry in the problem has to be done, in order to create vectors AX parallel to the straight line from the GPS to the occultation point, and vectors AY perpendicular to AX and nearly parallel to the curvature radius. We now assume that the angle between the NG vector and the curvature radius can approximately be determined by

$$\cos(\beta) = \frac{R_c}{\left\| \vec{RGPS} - \vec{RLC} \right\|} \quad (2-29)$$

which is a good approximation since the curvature radius is perpendicular to the reference ellipsoid tangent that is nearly parallel to the straight line between the GPS and the occultation point. We then have that

$$\sin(\beta) = \sqrt{1 - \cos^2(\beta)} \quad (2-30)$$

and by trigonometry it can be derived that

$$\overrightarrow{AX} = \cos(\beta) \cdot \overrightarrow{NL} - \sin(\beta) \cdot \overrightarrow{NG} \quad (2-31)$$

is the wanted X-axis unit vector. Similarly the Y-axis unit vector is given by

$$\overrightarrow{AY} = \sin(\beta) \cdot \overrightarrow{NL} + \cos(\beta) \cdot \overrightarrow{NG} \quad (2-32)$$

The coordinates of the satellites in the moving occultation planes are determined simply by forming the dot products between the J2000 position vectors and these basis vectors. In these coordinate systems the GPS Y-coordinate is nearly constant.

The coordinates in the moving occultation coordinate systems are used as approximate values of the coordinates in the (fixed) occultation plane coordinate system, i.e., the rotation of the Earth is neglected during the occultation.

2.2.6 Occultation Plane to Unmoving GPS System

First the Y coordinates are translated

$$YLEO_{\text{unmov}}(i) = YLEO(i) - R_c \quad (2-33)$$

$$YGPS_{\text{unmov}}(i) = YGPS(i) - R_c \quad (2-34)$$

We want the GPS to be fixed at its coordinates at the time when the ray penetrates deepest into the atmosphere. The Y-coordinate is constant in the occultation plane system, but the X-coordinate needs to be transformed in the following way. In order not to change the Doppler shift, i.e., total bending angle, we first form $F(i)$ (Gorbunov, Gurvich & Bengtsson 1996)

$$F(i) = \frac{XLEO(i) \cdot XGPS(i)}{XLEO(i) - XGPS(i)} \quad (2-35)$$

for each set of satellite positions. $XLEO$ and $XGPS$ are the LEO and GPS occultation plane X-coordinates respectively. Then the new LEO X-coordinates are given by

$$XLEO_{\text{unmov}}(i) = \frac{F(i) \cdot XGPS(i_{occ})}{F(i) - XGPS(i_{occ})} \quad (2-36)$$

and the GPS position can be fixed, i.e., $XGPS_{\text{unmov}}(i) = XGPS(i_{occ})$ for all values of i .

2.3 Initialisation of the Atmosphere Model/GRIB File

The refractivity field used by the wave propagator can be determined from two different models such as:

1) a MSIS90 model which is an empirical model describing the climatologically features of the atmosphere. It is based on temperature, density and composition data from a comprehensive summary of rocket flights, satellites and incoherent scatter radar, including data from high solar activity. The original version of the model was introduced in 1977 and has been improved and revised regularly since then. The latest version of MSIS (MSIS90) now extends into the mesosphere and lower atmosphere in order to provide a single analytic model for calculating temperature and density profiles, representative of the climatologically average for various geophysical conditions. It includes a longitudinal variability linked to the planetary waves activity, and time dependence from the solar activity. While month-to-month details are not completely represented, lower atmosphere temperature data are fit to an overall standard deviation of 3 K and pressure to 2 %. Comparisons with measured data indicate that the model represents reasonably well current knowledge of the climatologically average.

2) a Numerical Weather Prediction model (NWP). In this case the data is contained in a so-called GRIB file.

GRIB is the **World Meteorological Organization (WMO)** format for **GRI**dded **B**inary data. It is widely used in the international meteorological community, for the interchange of gridded weather data fields. GRIB data is also self-describing, meaning that the information needed to read the file is present within the file. Each GRIB file is composed of a series of GRIB records. One GRIB record holds the gridded data for one parameter at one time and at one level. Each GRIB record is composed of 6 sections. Section 4 contains the data itself. The other sections give the information required to read the GRIB record, and information on the meteorological parameter contained in the record, the level the record refers to and the type of grid the parameter is on. Section 1, known as the product definition section, and section 2, known as the grid definition section, are the information sections most frequently referred to by users of GRIB data. The product definition section (section 1) contains information about the parameter, level type, level and date of the record. The grid definition section (section 2) contains information on the grid, for instance whether the grid is regular, and the resolution of the grid.

Normally the refractivity is not directly found in the GRIB file, but can be calculated from the temperature, pressure and humidity fields found in the file. The refractivity fields must be known with a high resolution in the area of the occultation. Interpolation is needed in order to get the high resolution of the field (see Appendix C for details).

2.4 Atmospheric Refractivity

The atmospheric profiling technique provides measurements of the Doppler shift of the probing GPS signals that have passed through the limb of the atmosphere. The magnitude of the shift is related to the atmosphere's refractivity gradients along the path of the signal. These in turn are related to the atmosphere's temperature, pressure and humidity fields.

Provided that the signal has sufficiently high quality (i.e., signal-to-noise) and that other variables of the experiment (e.g. the positions of the transmitter and receiver) are known to sufficient accuracy, information on the temperature and humidity fields can be retrieved. More specifically, from series of measurements obtained during the occultation event, the profiles of temperature and humidity close to the tangent point of the signal path can be estimated.

The occultation technique is defined by geometry, where the transmitter and the receiver are positioned relative to the Earth in such an arrangement, that the radio wave signal traverses the atmosphere from the ionosphere to the limb of the Earth and back again to the LEO satellite. The propagation path of the GPS electromagnetic wave through the atmosphere will be influenced by the dispersive characteristics of the medium, due to ionised and neutral parts of the gas in the atmosphere. The results are bending and change in the phase and amplitude of the transmitted signals. Refractivity index generally decreases with radius in the neutral atmosphere, which causes a ray to bend by an angle α towards the planet.

In order to derive atmospheric properties from retrieved profiles of the real component of the atmospheric refractive index, n , it is necessary to know how these properties influence n . In this context we only consider microwave wavelengths in the Earth's atmosphere, and n contains contributions from four main sources. These are, in order of importance, the dry atmosphere (dry term), water vapour (wet term), free electrons in the ionosphere (ionospheric term), and liquid water (scattering term). Their effects are given to first order by the following equation

$$N = (n - 1) \times 10^6 \cong 77.6 \frac{P}{T} + 3.73 \times 10^5 \frac{P_w}{T^2} + 4.03 \times 10^7 \frac{n_e}{f^2} + 1.4W \quad (2-37)$$

where N is refractivity, P is atmospheric pressure in mbar. T is atmospheric temperature in Kelvin, P_w is water vapour partial pressure mbar, n_e is electron density per cubic meter, f is transmitter frequency in Hertz, and W is liquid water content in grams per cubic meter. The GPS satellites continuously radiate signals at two different frequencies in order for the users to separate the frequency dependent propagation delays due to ionospheric refractivity from other effects like the temperature and moisture of the neutral atmosphere.

The dry refractivity term is due to polarisability of molecules in the atmosphere, i.e., the ability of an incident electric field to induce an electric dipole in the molecules. Dry refractivity is proportional to the molecular number density and is dominant below 60-90 km. The moist refractivity term is due primarily to the large permanent dipole moment of water vapour and becomes significant in the lower troposphere.

The ionospheric term in Eq. (2-37), which is a first order approximation to the Appleton-Hartree equation, is mainly due to free electrons in the ionosphere and becomes important above 60-90 km. The scattering term in Eq. (2-37) is due to liquid water droplets suspended in the atmosphere. This term is small compared to the others and is accordingly neglected.

2.5 Determination of the Neutral Atmosphere Propagation Area

Figure 2.10 below shows the wave propagation area in the neutral atmosphere. The area limits are defined by the four parameters $Xmin$, $Xmax$, $Ymin$ and $Ymax$.

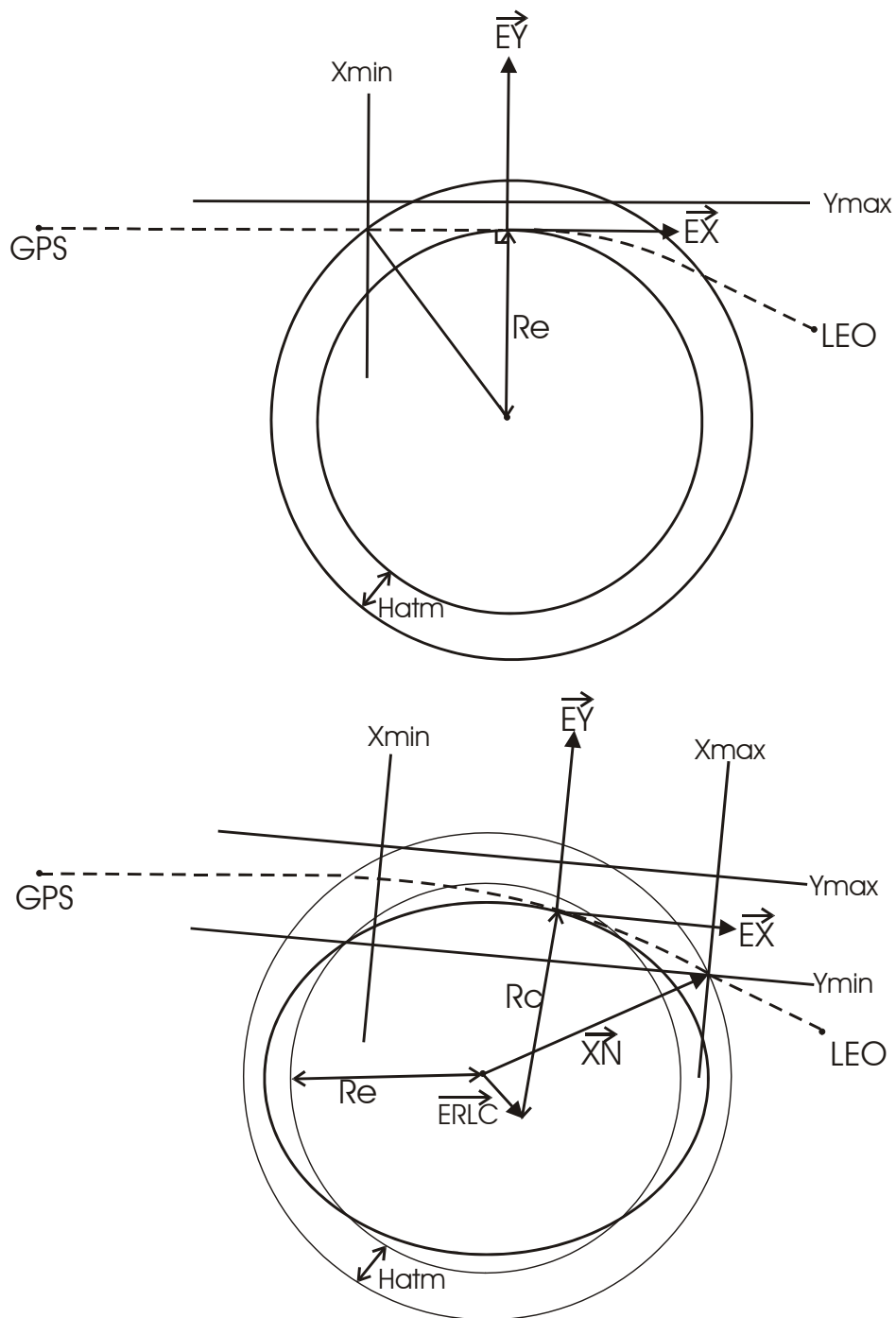


Figure 2-10: The upper figure depicts the Earth spherical approximation used for determination of $Xmin$. The lower figure is a more realistic description of the occultation geometry where the Earth flattening is taken into account. The \vec{XN} vector defines the values $Xmax$ and $Ymin$.

The height of the atmosphere and the maximum height of the neutral atmosphere occultations are represented by the two parameters H_{atm} and H_{max} . The local curvature radius of the Earth is denoted by R_c , and the geometric mean radius of the

Earth is denoted by R_e . The two parameters X_{min} and Y_{max} are defined as the X-value where the field enters the atmosphere and the maximum Y-value of the occultation, respectively. The parameters are given by

$$X_{min} = -\sqrt{(R_e + H_{atm})^2 - R_e^2} \quad (2-38)$$

$$Y_{max} = H_{max} + D_{ya} \quad (2-39)$$

where H_{max} is the selected upper boundary of the screens, and D_{ya} is the extent apodization zone (see section 2.8).

It can be seen from geometrical considerations (Figure 2.10 and 2.11) and from ray tracing that the area limiting parameters X_{max} and Y_{min} are given by

$$X_{max} = \vec{E}_x * (\vec{XN} - \vec{ERLC}) \quad (2-40)$$

$$Y_{min} = \vec{E}_y * (\vec{XN} - \vec{ERLC}) - R_e - D_{ya} \quad (2-41)$$

The \vec{XN} vector can be found from the following procedure: determine by ray tracing the point at the top of the atmosphere with the largest X and the smallest Y-value, which rays can reach without intersecting the Earth. That means that the \vec{XN} vector ranges from the centre of the Earth to the (Y_{min}, X_{max}) point. The latter can be defined by the ray that leaves the atmosphere having the smallest Y-value (Y_{min}) and the largest X-value (X_{max}) at the atmospheric edge.

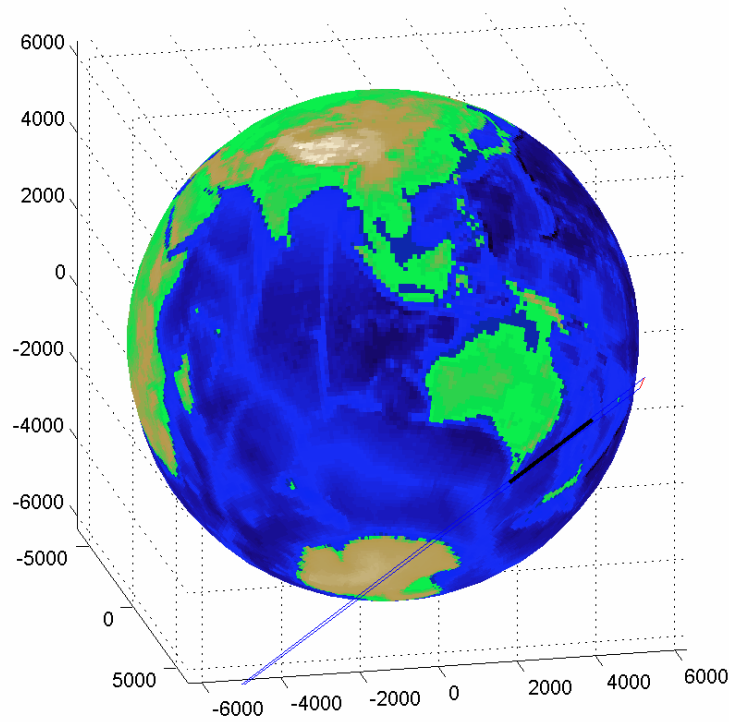


Figure 2-11: The figure depicts the propagation area in the neutral atmosphere together with the first and last rays propagating between the GPS and LEO satellites. A short red line, on the right side of the figure, shows the trajectory of the LEO satellite during the occultation.

2.6 Ray Tracing in the Neutral Atmosphere

It is known from geometrical optics that the propagation of rays are determined by the *eikonal* equation given by

$$\frac{\partial^2 S}{\partial X^2} + \frac{\partial^2 S}{\partial Y^2} = n(X, Y)^2 \quad (2-42)$$

where the gradient of S gives the direction of the ray. The function S is often called *the eikonal*, and Eq. (2-42) is the basic equation of geometrical optics. The equation, as described in Eq. (2-42) is valid for the two-dimensional cases, but can easily be extended to three dimensions. n represents the index of refraction of the medium in which the rays propagate and (X, Y) are the coordinates in the Cartesian coordinate system. By rewriting this equation in a new ray based coordinate system we obtain the following equation

$$\frac{d}{ds} \left[n(\vec{r}) \frac{d\vec{r}}{ds} \right] = \nabla n(\vec{r}) \quad (2-43)$$

where s denotes the ray path. Under the assumption that $\frac{d}{ds}[n(\vec{r})\frac{d\vec{r}}{ds}] \approx n(\vec{r})\frac{\partial^2\vec{r}}{\partial s^2}$ the equation above can be given by the following two coupled differential equations

$$\begin{aligned}\frac{\partial\vec{r}}{\partial s} &= \vec{U} \\ \frac{\partial\vec{U}}{\partial s} &= \frac{1}{n(\vec{r})}\vec{U}\end{aligned}\tag{2-44}$$

These coupled differential equations, that determine the ray propagation in a medium where the index of refraction as a function of position \vec{r} is given by, $n(\vec{r})$, can for example be solved using the Runge-Kutta technique.

2.7 Wave Propagation from the GPS Satellite to the 1. Screen

The wave propagating from the GPS satellite to the 1. screen can either be approximated by a spherical wave or by the field from a vertical magnetic dipole. The field from the spherical wave is determined by the following equation

$$E(\vec{R}) = E_0 \frac{\exp(ik_T |\vec{R}|)}{\sqrt{|\vec{R}|}}\tag{2-45}$$

\vec{R} is the radius vector from the GPS satellite to the point on the 1. screen where the field is evaluated. The wave emitted from the GPS satellite corresponds to the solution of the Helmholtz equation with a source located at the position of the GPS satellite. Since the WOP is a two-dimensional wave propagation model we need the solution of the two-dimensional Helmholtz equation. This is the reason for the square root in the denominator of Eq. 2-45. E_0 and k_T is a scaling constant and the free space wave number, respectively (see Appendix E for details). The harmonic time dependence of the signal has here been suppressed. The equation below can be used if a vertical magnetic dipole is used as the electromagnetic source

$$E_\phi(\vec{R}) = E_0 \frac{\exp(ik_T |\vec{R}|)\sin(\theta)}{|\sqrt{|\vec{R}|}}\tag{2-46}$$

$$H_\theta(\vec{R}) = \frac{1}{\eta} E_\phi(\vec{R})$$

where $\eta \approx 120\pi$ and the constant, E_0 , can be found from the current and diameter of the loop that generates the vertical magnetic dipole. The electric and magnetic field components are expressed in a spherical coordinate system. The electric and magnetic field components, not described in the equation above, can all be set equal to zero. The two equations for the E_ϕ and H_θ components are only valid in the far field where

terms proportional with r^{-2} and r^{-3} have neglected. The electric field from the dipole is depicted in the Figure 2.12.

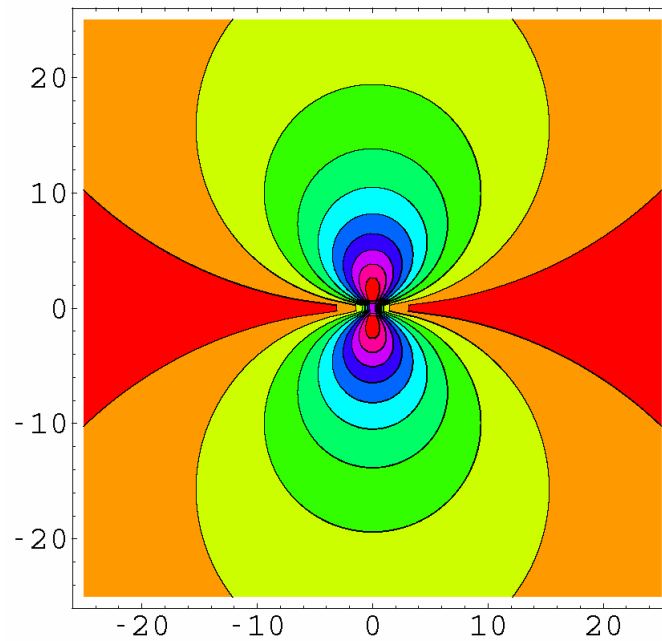


Figure 2-12: The Figure shows the field from the vertical magnetic dipole in the horizontal plane.

2.8 Wave Propagation between the Screens in the Neutral Atmosphere

The wave propagation between the screens in the neutral atmosphere will be described in this section. The solution of the external boundary problem for the Helmholtz equation in the form of the Fresnel integral is especially simple when the electromagnetic field is propagating between two parallel lines. The FFT technique can in this case be used to speed up the computations.

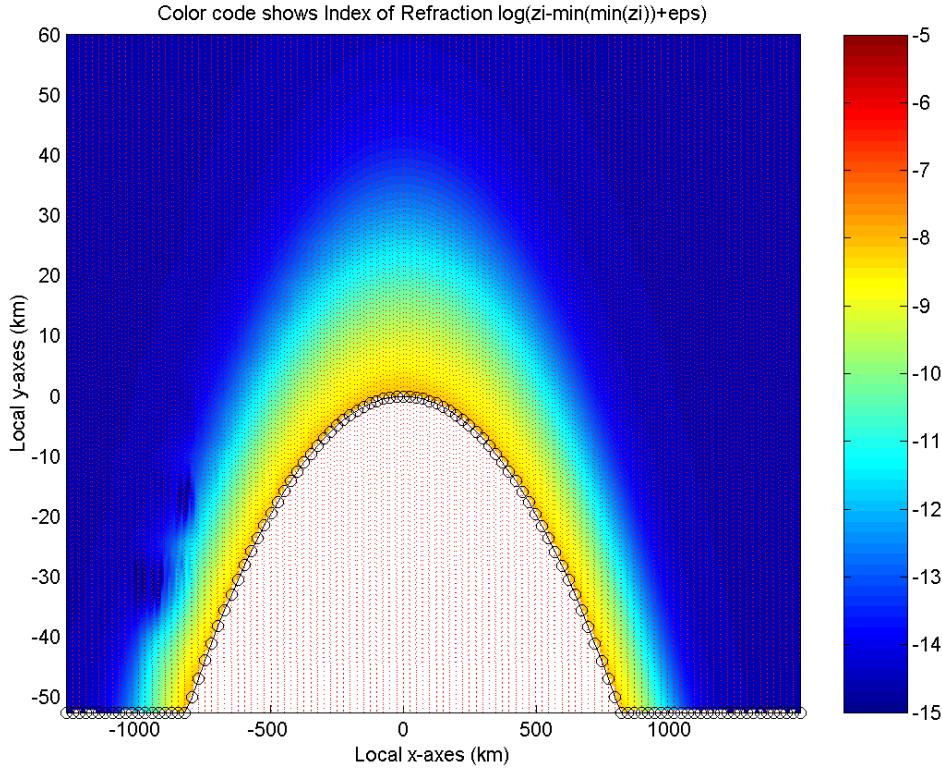


Figure 2-13: The screens and the refractivity in the neutral atmosphere. The dotted red lines denote the screens. The refractivity profile is calculated with the use of the ECHAM model and expressed in the local (X,Y) coordinate system. The white area in the figure represents the Earth. Multipath is expected to appear in the region from -700 km to -1000 km, where the refractivity symmetry is broken. The colour bar denotes the logarithm of the refractivity.

The field component, ψ , of the electromagnetic wave can in the normal Cartesian coordinate system be expressed by the following 2-D scalar wave equation

$$\frac{\partial^2 \psi}{\partial x^2} + \frac{\partial^2 \psi}{\partial y^2} + k^2 n^2 \psi = 0 \quad (2-47)$$

where k and n represent wave number and index of refraction. In general, the refractive index varies with range X and height Y and therefore Eq. 2.47 is not exact. It is however a good approximation provided the variations of n remain slow on the scale of a wavelength.

It is now common practice to use the reduced function u given by

$$u(x, y) = e^{-ikx} \psi(x, y) \quad (2-48)$$

The reduced function will be slowly varying along the X-axis for propagation angles close to the paraxial direction (the horizontal direction), which gives it convenient numerical properties. The wave equation for the reduced function must be given by

$$\frac{\partial^2 u}{\partial x^2} + 2ik \frac{\partial u}{\partial x} + \frac{\partial^2 u}{\partial y^2} + k^2(n^2 - 1)u = 0 \quad (2-49)$$

This equation can be formally factored as

$$\left(\frac{\partial}{\partial x} + ik\left(1 - \sqrt{\frac{1}{k^2} \frac{\partial^2}{\partial y^2} + n^2(x, y)}\right)\right)\left(\frac{\partial}{\partial x} + ik\left(1 + \sqrt{\frac{1}{k^2} \frac{\partial^2}{\partial y^2} + n^2(x, y)}\right)\right)u = 0 \quad (2-50)$$

The square root term in this equation represents an operator acting on the reduced function u . Some of the solutions to this differential equation can be found by solving the differential equations corresponding to each of the two factors in the equation above. We must therefore solve the following pseudo-differential equations

$$\frac{\partial u}{\partial x} = -ik\left(1 - \sqrt{\frac{1}{k^2} \frac{\partial^2}{\partial y^2} + n^2(x, y)}\right)u \quad (2-51)$$

$$\frac{\partial u}{\partial x} = -ik\left(1 + \sqrt{\frac{1}{k^2} \frac{\partial^2}{\partial y^2} + n^2(x, y)}\right)u \quad (2-52)$$

The solutions to the first of these equations correspond to waves travelling along the positive X-direction (forward propagation) while solutions to the last equation correspond to waves travelling along the negative X-direction (backward propagation). The two differential equations are therefore called the *outgoing* and *incoming* parabolic wave equations, respectively. Adding the solutions of the two parabolic equations give us the solution to the original equation. However, in the following we will restrict ourselves to the solutions of the outgoing parabolic equation that solve for energy propagating in a paraxial cone centred on the positive X-direction.

Approximating the square root operator by a 1. order Taylor expansion $\left(\sqrt{\frac{1}{k^2} \frac{\partial^2}{\partial y^2} + n^2(x, y)} \approx \frac{1}{2k^2} \frac{\partial^2}{\partial y^2} + \frac{n^2(x, y)}{2} + \frac{1}{2}\right)$ results in the following standard parabolic equation (SPE)

$$\frac{\partial^2 u(x, y)}{\partial y^2} + 2ik \frac{\partial u(x, y)}{\partial x} + k^2(n^2(x, y) - 1)u(x, y) = 0 \quad (2-53)$$

The equation is valid for propagation angles close to the horizon (the paraxial approximation). More refined approximations to the square root operator result in equations valid for wider propagation angles. The SPE can be solved using a number of different techniques. One of them is the split-step/sine transform solution, which gives an efficient and fast solution to the SPE. The split-step/sine transform solution to SPE is given by (Levy 2000):

$$u(x + \Delta x, y) = e^{\frac{ik(n^2-1)\Delta x}{2}} S^{-1} \left\{ e^{-\frac{i\pi^2 p^2 \Delta x}{2k}} S\{u(x, y)\} \right\} \quad (2-54)$$

S and S^{-1} represent here the sine and inverse sine transformations, respectively. The sine transform of the function $u(x, y)$ with respect to height is given by the following equation

$$S\{u(x, y)\} = U(x, p) = \int_0^{\infty} u(x, y) \sin(2\pi p y) dy \quad (2-55)$$

The transformed variable, p , can be thought of as the wave numbers for the plane waves in which the field is expanded.

Another approximation to the square root operator is given by the following equation

$$\sqrt{\frac{1}{k^2} \frac{\partial^2}{\partial y^2} + n^2(x, y)} \approx \sqrt{\frac{1}{k^2} \frac{\partial^2}{\partial y^2} + 1 + n(x, y) - 1} \quad (2-56)$$

This operator is valid for a wider span of propagation angles. The corresponding split-step/sine transform solution for this wider angle parabolic equation (WPE) is given by

$$u(x + \Delta x, y) = e^{ik(n-1)\Delta x} S^{-1} \left\{ e^{ik\Delta x \left(\sqrt{1 - \frac{\pi^2 p^2}{k^2}} - 1 \right)} S\{u(x, y)\} \right\} \quad (2-57)$$

This equation will be used in the wave propagator because it is valid for a broader range of propagation angles compared to SPE.

The split-step/sine transform solution can be thought of as a field propagating through a number of phase screens. The distance between the screens is Δx . The field propagates along the positive X-axis and the screens are all orthogonal to the X-axis. The expression within the inverse sine transform operator propagates the field a distance Δx , while the first exponential in the equation (Eq. 2-54) give us the impact on the field of the phase screen. This solution decouples the diffractive effects, included in the operations performed by the sine transform operator, from the refractive effects performed by the first exponential in the equation. This decoupling results in a small error.

The electromagnetic field must satisfy the electromagnetic boundary conditions on the screens in the neutral atmosphere. We therefore define an apodization zone where the electromagnetic field falls off following an exponential function. The apodization zone is found on the top and bottom of all of the screens in the neutral atmosphere and the field here is given by

$$U_{\text{new}} = e^{-((Y-YU)/(Dya/3))^2} U_{\text{old}} \text{ for } Y > YU = Y_{\text{max}} - 0.75Dya \quad (2-58)$$

and

$$U_{\text{new}} = e^{-((YD-Y)/(Dya/3))^2} U_{\text{old}} \text{ for } Y < YD = Y_{\text{min}} + 0.75Dya \quad (2-59)$$

where Y gives us the position on the screen and Y_{max} and Y_{min} are the Y-coordinate for the largest and smallest positions on the screen. Dya is the size of the apodization area on the top and bottom of the screen. The value of this parameter should be around 5 km. $U_{\text{new}}(Y)$ and $U_{\text{old}}(Y)$ is the value of the complex field before and after the apodization of the field.

The resolution, i.e., the distance between the points on the screen, is determined from the following equation

$$\Delta y \leq \frac{\lambda}{4\sin(\varepsilon_{\text{max}})} \quad (2-60)$$

where ε_{max} is the maximum propagation angle from the horizon to be represented without distortion. For the spherical wave this opening angle can be calculated as

$$\varepsilon_{\text{max}} = \max(\text{abs}(Y_{\text{max}}/X_{\text{GPS}}, \text{abs}(Y_{\text{min}}/X_{\text{GPS}})) \quad (2-61)$$

The minimum number of point on the screen is

$$N_{\text{min}} = \frac{4L}{\lambda} \sin(\varepsilon_{\text{max}}) \quad (2-62)$$

There is also an upper limit for the number of points on the screen given by:

$$N_{\text{max}} = \frac{4L}{\lambda} \sin(\alpha_{\text{max}}) \quad (2-63)$$

where α_{max} is the maximum bending angle found from ray-tracing. If the Doppler phase is greater than $\pi/2$ and the current number is less than N_{max} , then it is necessary to double the number of points on the next screen.

The equations above are correct under the assumption of a wave propagating along the X-axis in a Cartesian coordinate system. In our case the wave is travelling along the spherical Earth with heights measured along radials passing through the Earth's centre. It will be shown that the equations are still valid when the so-called *Earth flattening transformation* (Levy 2000) is used (see Figure 2.14 below). However, in the current WOP implementation this transformation has not been included.

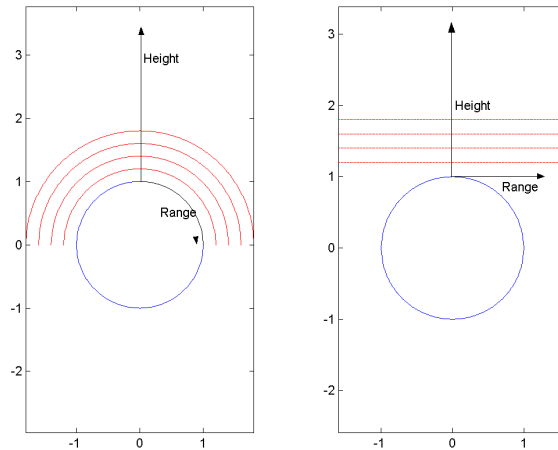


Figure 2-14: The figure shows the so-called *Earth flattening transformation* where concentric shells representing ranges and heights are mapped to parallel planes.

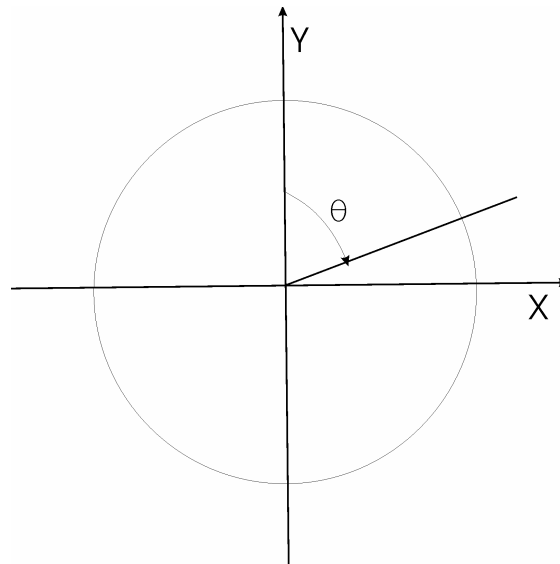


Figure 2-15: The (X,Y) coordinate system

We have to use Maxwell's equations expressed in a spherical coordinate system, given by (r, θ, ϕ) , as a starting point. We end up having a particular simple form of the wave equation under the assumptions of a:

1. vertical magnetic dipole as the radiating source, in which case the components E_r, E_θ, H_ϕ are all zero

or a

2. vertical electric dipole as the radiating source, in which case the components H_r , H_θ , E_ϕ are all zero.

The wave equation gets the same form, when expressed in terms of the function ψ , in these two cases if we use the following equations in the case of a vertical magnetic dipole and a vertical electric dipole, respectively.

$$\begin{aligned} E_\phi &= \frac{1}{\sqrt{kr \sin(\theta)}} \psi \\ H_\phi &= \frac{n}{\sqrt{kr \sin(\theta)}} \psi \end{aligned} \quad (2-64)$$

The wave equation in a 2-D Cartesian coordinate system (X,Y), for the function ψ , will now in both of these cases take the well-known form

$$\frac{\partial^2 \psi}{\partial X^2} + \frac{\partial^2 \psi}{\partial Y^2} + k^2 n^2(X,Y) \psi = 0 \quad (2-65)$$

We now have to define a transformation that maps concentric circles on to straight lines. The points (X,Y) are now understood to be points in the complex plane. The X and Y-coordinates can be expressed with the use of the height h above the surface and the angle θ , where the distance travelled along the surface of the Earth is approximately given by θR_e (see Figure 2.15). The radius of the Earth is again denoted by R_e .

$$\begin{aligned} X &= (R_e + h) \sin(\theta) \\ Y &= (R_e + h) \cos(\theta) \end{aligned} \quad (2-66)$$

The following conformal transformation transform the complex points (X,Y) into a new set of complex points (x,y)

$$\begin{aligned} \xi &= iR_e \log\left(\frac{\zeta}{iR_e}\right) \\ \zeta &= X + iY \\ \xi &= x + iy \end{aligned} \quad (2-67)$$

From these equations we obtain

$$\begin{aligned} x &= R_e \theta \\ y &= R_e \log\left(1 + \frac{h}{R_e}\right) \end{aligned} \quad (2-68)$$

The wave equation now has to be expressed in the new coordinate system. Using the properties of the conformal transformation it can be shown that the wave equation is given by

$$\frac{\partial^2 \psi}{\partial x^2} + \frac{\partial^2 \psi}{\partial y^2} + k^2 \tilde{n}^2 e^{2y/R_e} \psi = 0 \quad (2-69)$$

where

$$\tilde{n}(x, y) = n(x, h) \quad (2-70)$$

Under the assumption that y is approximately equal to h we immediately obtain the following equation

$$\frac{\partial^2 \psi}{\partial x^2} + \frac{\partial^2 \psi}{\partial h^2} + k^2 m^2(x, h) \psi = 0 \quad (2-71)$$

where m is the modified index of refraction given by

$$m(x, h) = n(x, h) + h / R_e \quad (2-72)$$

The above equation can, with the appropriate boundary conditions, be solved using the Fourier split-step algorithm. This approach to perform modelling of electromagnetic wave propagation in the troposphere has the advantages of being a full-forward-wave calculation that requires relatively few approximations and accommodates lateral as well as vertical in-homogeneities in the refractive conditions (Kuttler & Dockery 1991).

2.9 Wave Propagation from a Screen to the LEO Orbit

In this section we will explain the equations that determine the propagation of the field from the last phase screen to the LEO orbit (for details we refer to Appendix G). The split-step Fourier transform approach cannot be used in this case because the phase screens and the LEO orbits are not parallel.

If the electric field, E_0 , is known all over a distant line S , $E(\vec{x})$ can be found at a given point \vec{x} . This is the two dimensional solution for the external boundary problem for the Helmholtz equation (Chew 1995, sect. 8.1)

$$E(\vec{x}) = \left(\frac{k_T}{2\pi} \right)^{1/2} \int_S E_0(\vec{y}) \cos \varphi_{xy} \frac{\exp(ik_T |\vec{x} - \vec{y}| - i\pi/4)}{|\vec{x} - \vec{y}|^{1/2}} dS_y \quad (2-73)$$

The solution (2-73) is the free space solution for a straight line S . In (2-73) k_T is the free space wave number, φ_{xy} is the angle between the normal \vec{n}_y to S and the vector $\vec{x} - \vec{y}$. The harmonic time dependence of the signal has been suppressed. The atmosphere is sufficiently tenuous to justify the use of the scalar version of the wave equation (Tatarski 1967). Because the scalar version of the wave equation applies, the same equation applies to the magnetic field, and thus it is only necessary to consider the electric field in the following. The solution is an approximation that can be used under the assumption that the line, S , is distant from the measurement point, i.e., y -points on S must fulfil the relation $k_T |\vec{x} - \vec{y}| \gg 1$. It has been assumed that the necessary corrections of the signal for receiver effects and relativistic effects have been performed to give the total measured phase of the signal. This solution can be used to describe the field measured at the LEO if the field is known on the last phase screen, S .

The integral (2-73) can be evaluated using a standard numerical integration routine. The integration is performed over a certain part of the last screen determined by the stationary phase technique. For every point, (x_L, y_L) on the

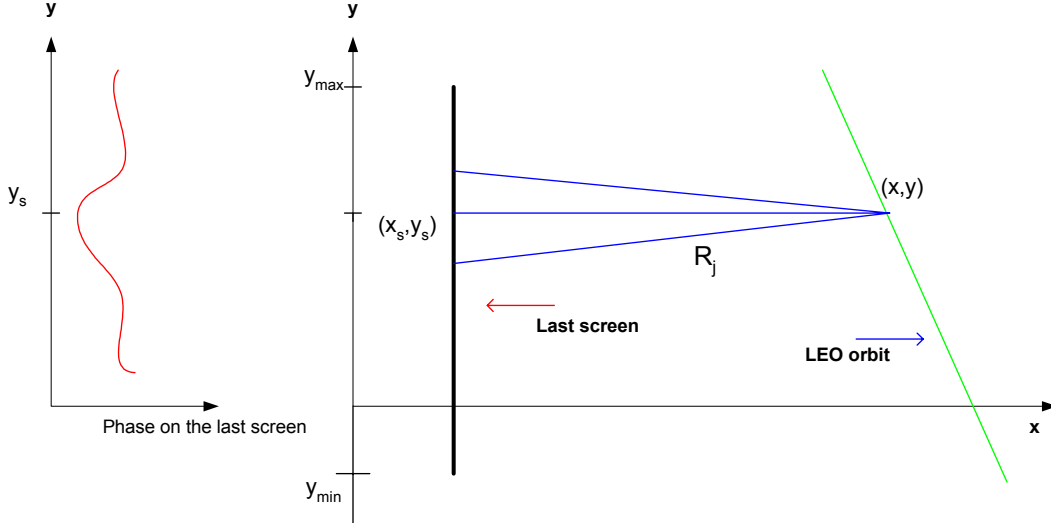


Figure 2-16: The sketch shows the concept of the stationary phase method. The red curve shows the accumulated phase along the last screen (thick line). The green line (LEO orbit) is the rightmost line. The geometric rays (blue) are indicated by an index j . For a point (x, y) on the LEO orbit the distance of the point on the screen is calculated and used in the calculation of the virtual phase. The position on the screen with the smallest virtual phase represents the stationary phase point for an individual point (x, y) on the LEO orbit.

LEO orbit the virtual phases (VP's) are calculated on the last phase screen using the following equation:

$$VP(i)=k_i*((x-x_s(i))^2+(y-y_s(i))^2)^{1/2} + PS(i) \quad (2-74)$$

where PS is the calculated phase on every point (x_s, y_s) on the last screen. The index, i , corresponds to samples on the last screen. The stationary phase is then the smallest value of the virtual phase given by $SP=min(VP)$.

The (2-73) integral must be solved for every point along the LEO orbit. If the computation time is an important concern the Fresnel integral can be solved using the stationary phase technique. The standard unwrapping routine, given by the equation below, must be used to calculate the accumulated phase from the phase of the complex signal.

$$Phase(i)=Phase(i-1)+modulo(Phase(i)- Phase(i-1)+\pi, 2*\pi)- \pi \quad (2-75)$$

This must be performed for all the samples i in the phase array.

The integration limits are deduced by the stationary phase point plus/minus the distances corresponding to phase changes of $10*\pi$ (see Appendix G).

If the stationary phase point is above or below the last screen, i.e., $y_{SP}>y_{max}$ or $y_{SP}<y_{min}$ the point on the LEO orbit in consideration, it is discarded. If the stationary phase point is within the range of the screen, but one of the integration limits, as described above, extends outside the screen, then the phase is extrapolated linearly and the amplitude is considered constant (see Appendix G).

The boundary problem of the Helmholtz equation, which leads to the solution (2-73) for the measured electric field, in general have two solutions. The solution, which describes the propagation of the electric field (2-73), propagates outwards from the line, S . The other solution propagates inwards, and can be considered to be the inverse solution to the boundary problem of the Helmholtz equation. This inverse solution is given by

$$E_0(\vec{y}) = \left(\frac{k_T}{2\pi} \right)^{1/2} \int_{S_L} E(\vec{x}) \cos \varphi_{xy} \frac{\exp(-ik_T |\vec{x} - \vec{y}| + i\pi/4)}{|\vec{x} - \vec{y}|^{1/2}} dS_L \quad (2-76)$$

where S_L denotes the LEO orbit.

Due to the similarity with the solution that describes the propagation of the signal, the inverse solution is denoted as the *back-propagation solution*. This solution can be used to derive the field, E_0 , at the line, S , if the field, E , at the LEO satellite is known. The back propagation algorithm has been described in the rapport “Analysis and Definition of Algorithms for Atmospheric Diffraction Effects” by Meincke (2000).

3 Simulation Results

We will in this section present the results of simulations performed with the wave propagator. The propagator is used on a meteorological ECHAM GRIB file. The numerical ECHAM model is based on the weather forecast model of the European Centre for Medium Range Weather Forecasts (ECMWF). Numerous modifications have been applied to this model at the Max Planck Institute for Meteorology and the German Climate Computing Centre (DKRZ) to make it suitable for climate forecasts and it is now a model of the fourth generation. A detailed description of the ECHAM4 model can be found in Roeckner et al. (1995).

The occultations have been selected so the wave propagating from the GPS satellite to the LEO satellite will enter areas in the neutral atmosphere where there are strong variations in the index of refraction, which results in diffraction/multipath. Two different wave propagation simulations have been selected and presented in the following 8 figures. The simulated amplitude and phase signals for the L1 and L2 waves, measured on board the LEO satellite, are shown in the figures below. Especially the amplitude signals exhibit strong signs of multipath effects. The variation in the amplitudes and phases of the electromagnetic field, in the neutral atmosphere, are shown with a colour code in separate plots. Again we see strong signs of multipath in the amplitude plots. The amplitude and unwrapped phase variation along phase screen no. 70 have also been plotted in two of the figures below. Phase screen no. 70 is placed on the local x-axis at an x-value of 447.96 km.

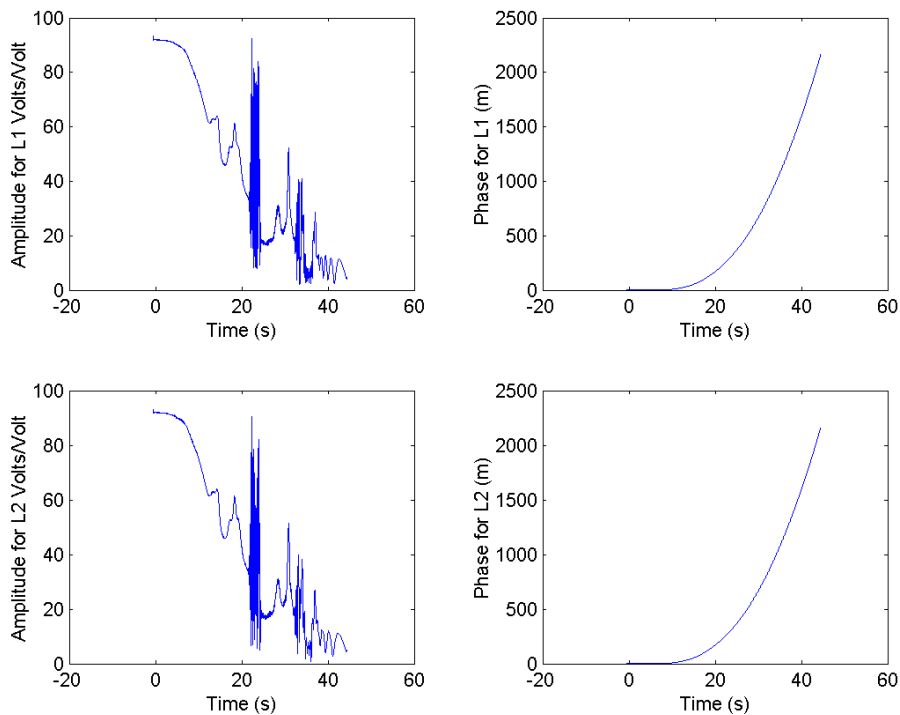


Figure 3-1: Amplitude and phases simulated with the use of a wave propagator. The L1 and L2 waves have traversed a region with strong variations in the atmospheric refractivity structure. The GPS and LEO orbits used in this simulation are identical to the orbits found in GPS/MET occultation no. 62 from February 2, 1997.

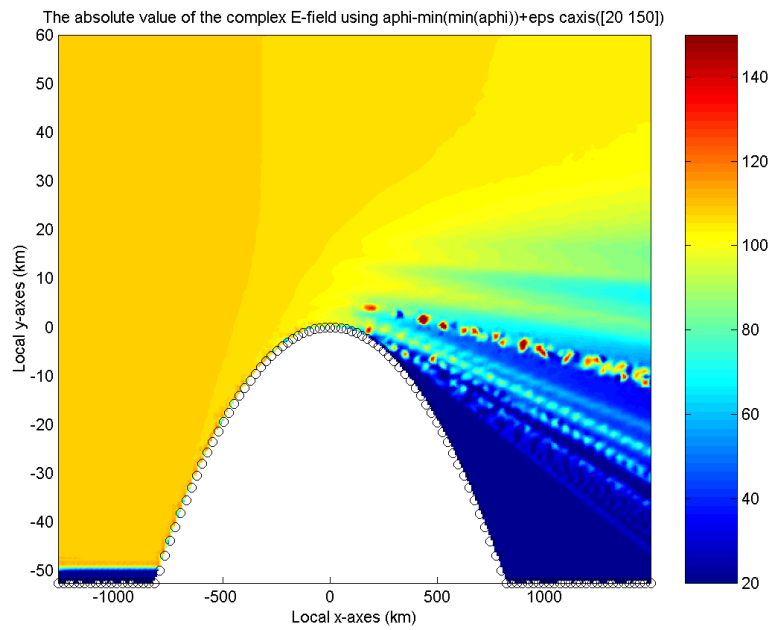


Figure 3-2: The colour code shows the variation of the amplitude over the screens simulated with the use of a wave propagator. The white area of the figure represents the Earth. The plot is based on the same data as the plots in the above figure. The colour bar denotes the variation in the field amplitude found in the plot.

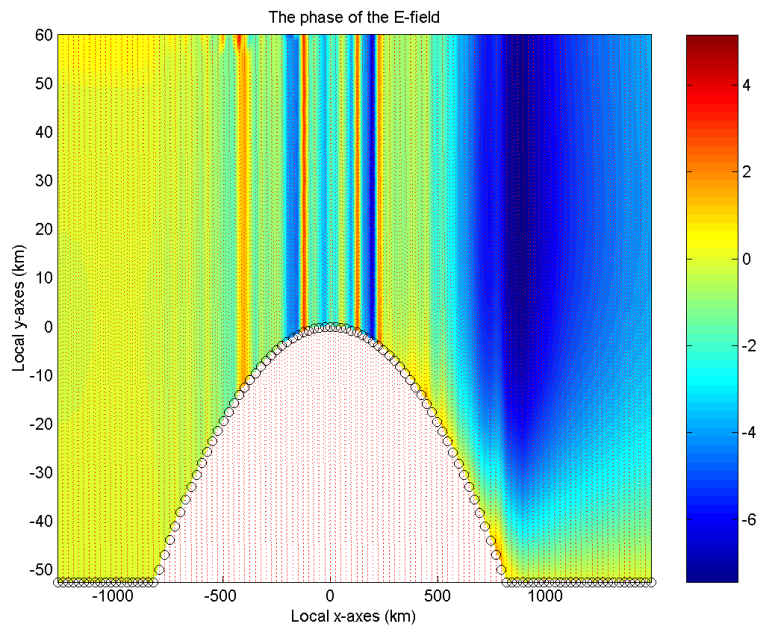


Figure 3-3: The colour code shows the variation of the unwrapped phase over the screens simulated with the use of a wave propagator. The white area in the figure represents the Earth. The plot is based on same data as the plots in the above figure. The colour bar denotes the unwrapped phase of the electromagnetic field.

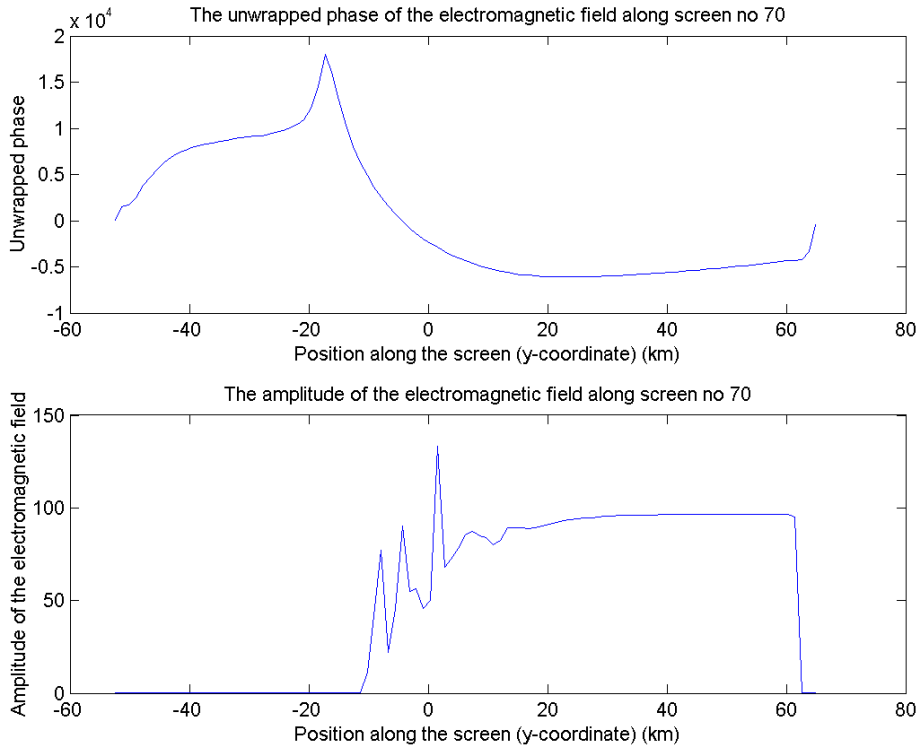


Figure 3-4: The two figures show the amplitude and phase of the electromagnetic field as a function of the position along phase screen no. 70. There are a total of 112 phase screens in the simulation.

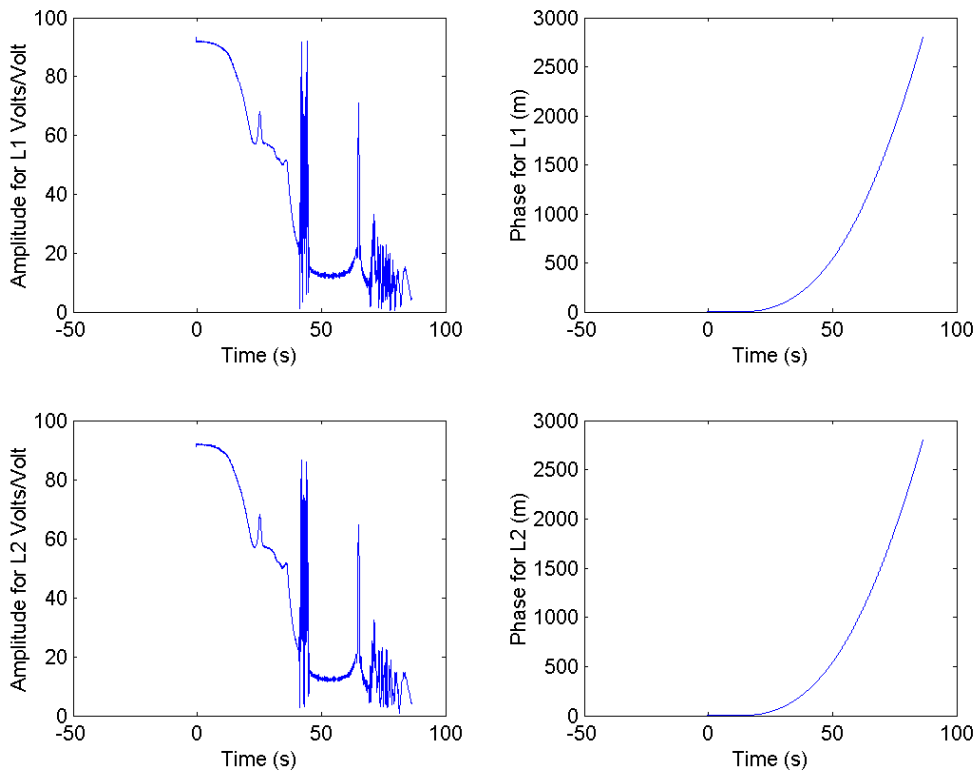


Figure 3-5: Amplitude and phases simulated with the use of a wave propagator. The L1 and L2 waves have traversed a region with strong variations in the atmospheric refractivity structure. The GPS and LEO orbits used in this simulation are identical to the orbits found in GPS/MET occultation no. 681 from the February 2, 1997.

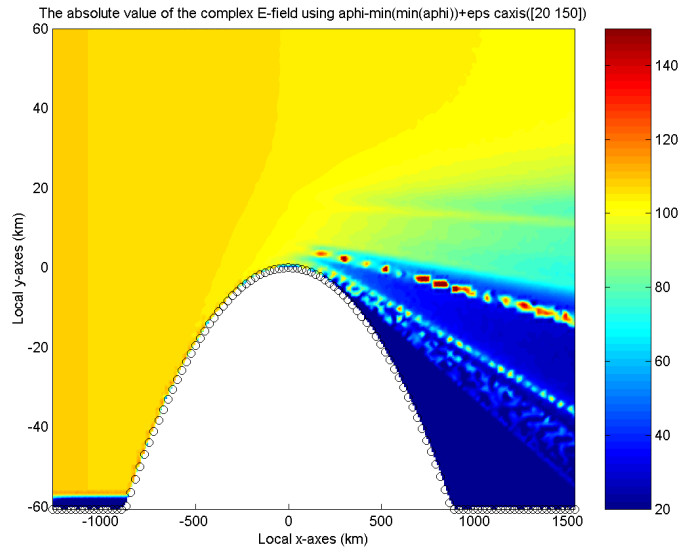


Figure 3-6: The colour code shows the variation of the amplitude over the screens simulated with the use of a wave propagator. The white area of the figure represents the Earth. The plot is based on same data as the plots in the above figure. The colour bar denotes the variation in the field amplitude found in the plot.

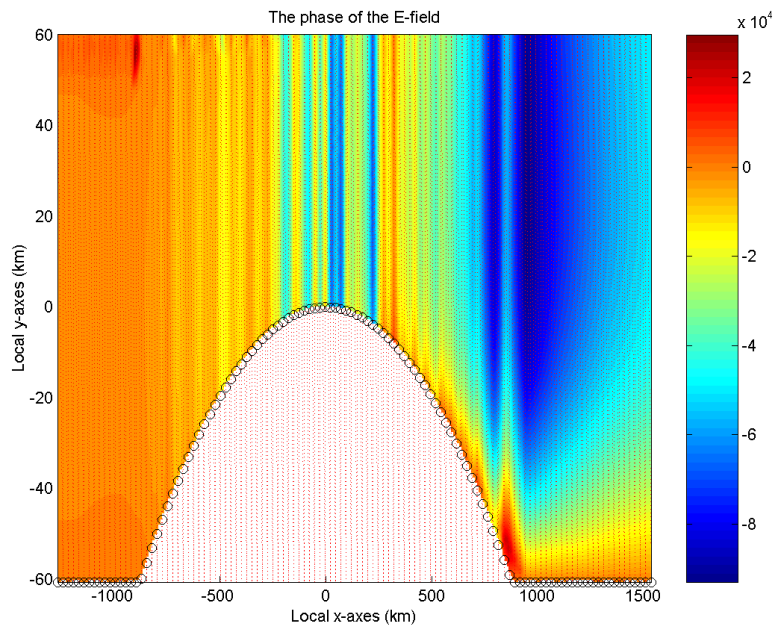


Figure 3-7: The colour code shows the variation of the unwrapped phase over the screens simulated with the use of a wave propagator. The white area in the figure represents the Earth. The plot is based on same data as the plots in the above figure. The colour bar denotes the unwrapped phase of the electromagnetic field.

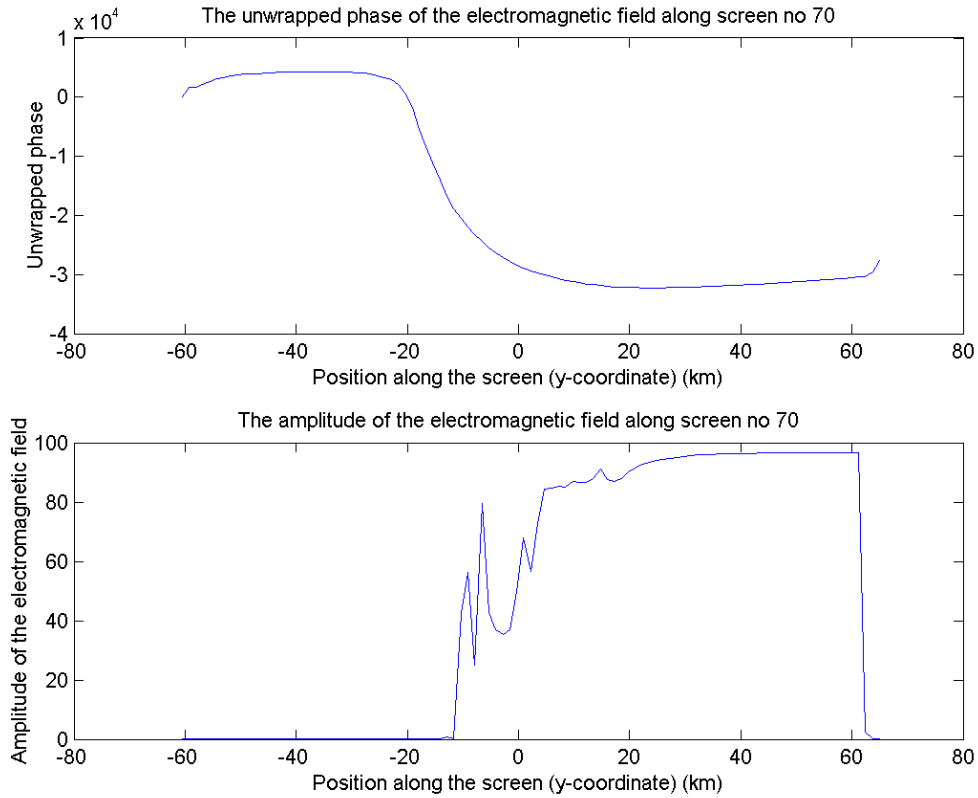


Figure 3-8: The two figures show the amplitude and phase of the electromagnetic field as a function of the position along phase screen no. 70. There are a total of 112 phase screens in the simulation.

4 Validation of the Wave Propagator

The wave propagator described above will be validated in this section. We have chosen to validate the WOP using a known phantom refractivity profile. The phantom refractivity profile N is given as function of the height h by the following equation

$$N(h) = 315e^{-0.136km^{-1}h} + Be^{-(h-BH)^2/0.05km} \quad (4-1)$$

where BH is the height position of the bump in the refractivity and B is the size of this bump. The first part of Eq. (4-1) is the refractivity of the reference atmosphere defined by the International Telecommunications Union [ITU, 1981]. The second part of the equation determines the strength and position of the refractivity bump. It is this bump that can generate multipath effects.

The multipath level is determined by the value of the B parameter. The wave propagator can be validated by comparing the bending angle calculated from the model refractivity profile (using an inverse Abel transform) with the bending angle versus impact parameter profile calculated with use of the wave propagator. The inverse Abel transform calculations on the model refractivity profiles have been performed in collaboration with Dr. Stig Syndergaard from the Institute of Atmospheric Physics at The University of Arizona.

The wave propagator is used on the phantom profile with some arbitrarily chosen GPS and LEO orbits. From L1 and L2 amplitude and phase output we calculate bending angle as function of impact parameter using either the *standard bending angle algorithm* or the *back propagation algorithm*. The former algorithm uses only phases of the occultation signals, whereas the latter algorithm makes use of phase as well as amplitude of the occultation signal. The back propagation algorithm is used when we have a high degree of multipath. The standard bending angle algorithm is used in all validation cases. The different steps needed in the wave propagator validation are summarised in Figure 4.1 below.

In the following pages results of simulations are presented. Simulations of four different values of the B parameters ($B=0$, $B=5$, $B=10$ and $B=20$) have been performed for a bump placed at a height of 5 km (see Fig. 4.2). The chosen B parameters range from no multipath up to a very high multipath level. Up to four figures are shown for each of the B parameter values. The measured amplitude at the LEO orbit and the bending angle vs. impact parameter (calculated using one or two or three algorithms) are shown as the first and second plot. The calculated bending angles based on the WOP occultation signals are compared to the calculated model bending angles in the second plot. In the cases of strong multipath (for $B=10$ and $B=20$) there will be a plot of the bending angle versus impact parameter calculated using the Radio Holographic technique and the back propagation algorithm together with the calculated model bending angle profile. Bending angle vs. impact parameter is calculated for the entire spectrum (Fourier spectrogram) of the occultation signal. The Fourier spectrogram is calculated with the use of the *Short-Time Fourier Transformation*. Finally, as the last plot, we present a 2-D colour plot that depicts the amplitude of the electromagnetic field in the neutral atmosphere. The effects of multipath can also be seen in these plots. The number of screens has been set to 1200 in the 4 simulations.

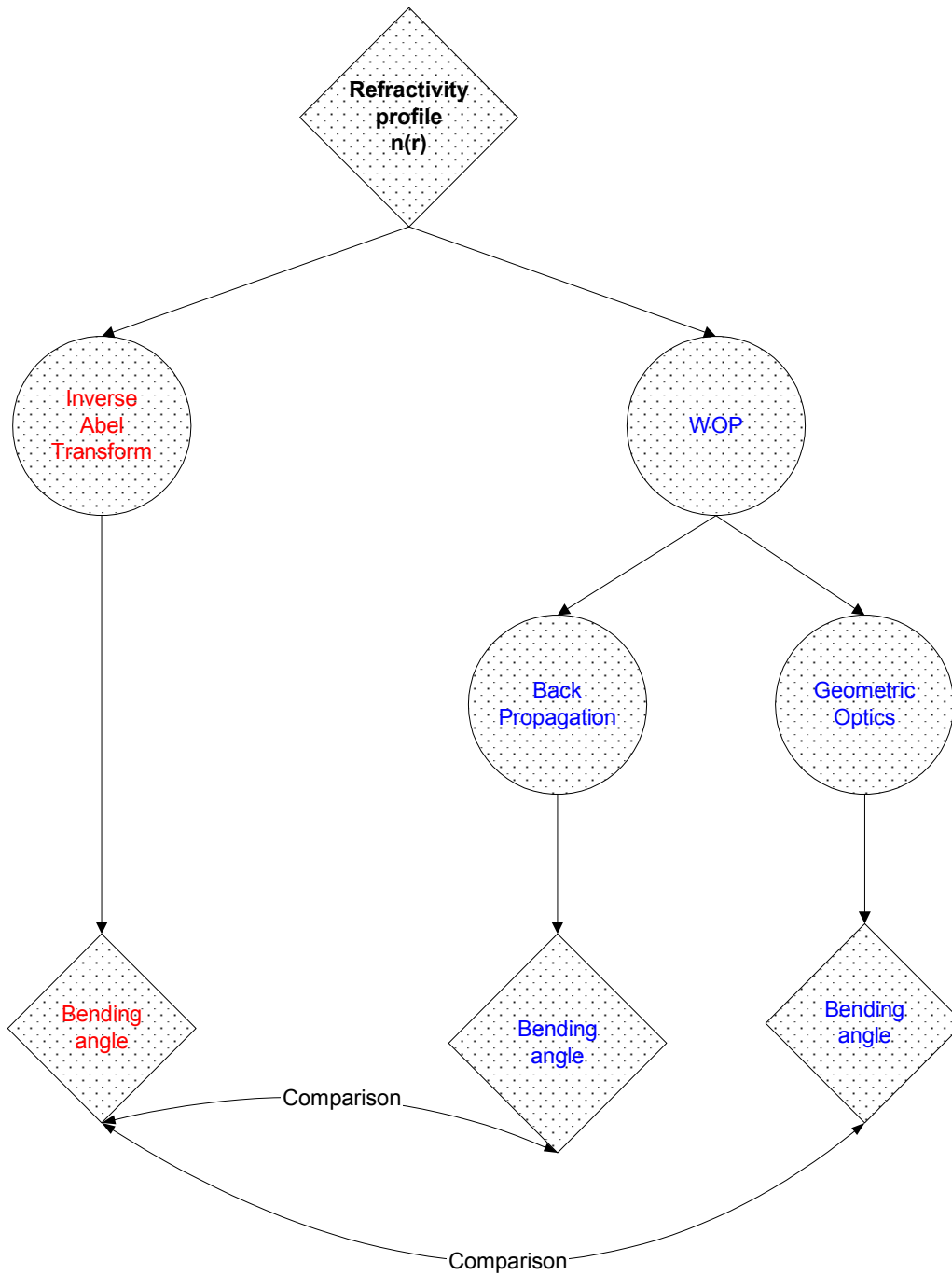


Figure 4-1: The figure depicts the method used in the validation of the WOP based on the phantom refractivity profile.

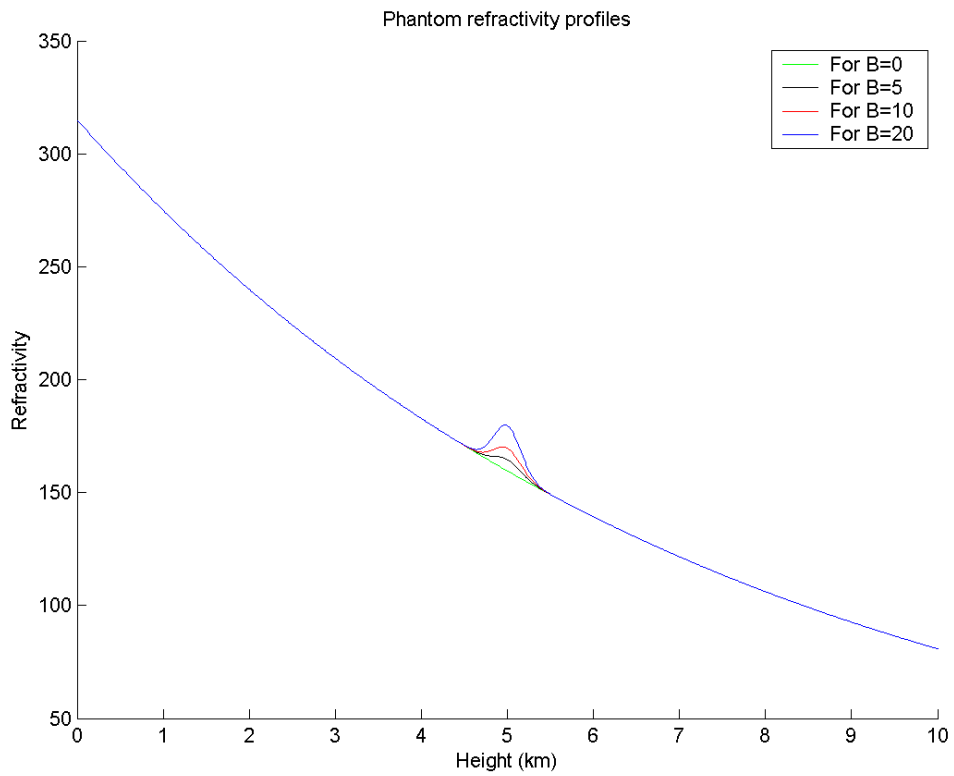


Figure 4-2: The plot shows the refractivity profile for the following values of B ($B=0$ $B=5$ $B=10$ $B=20$).

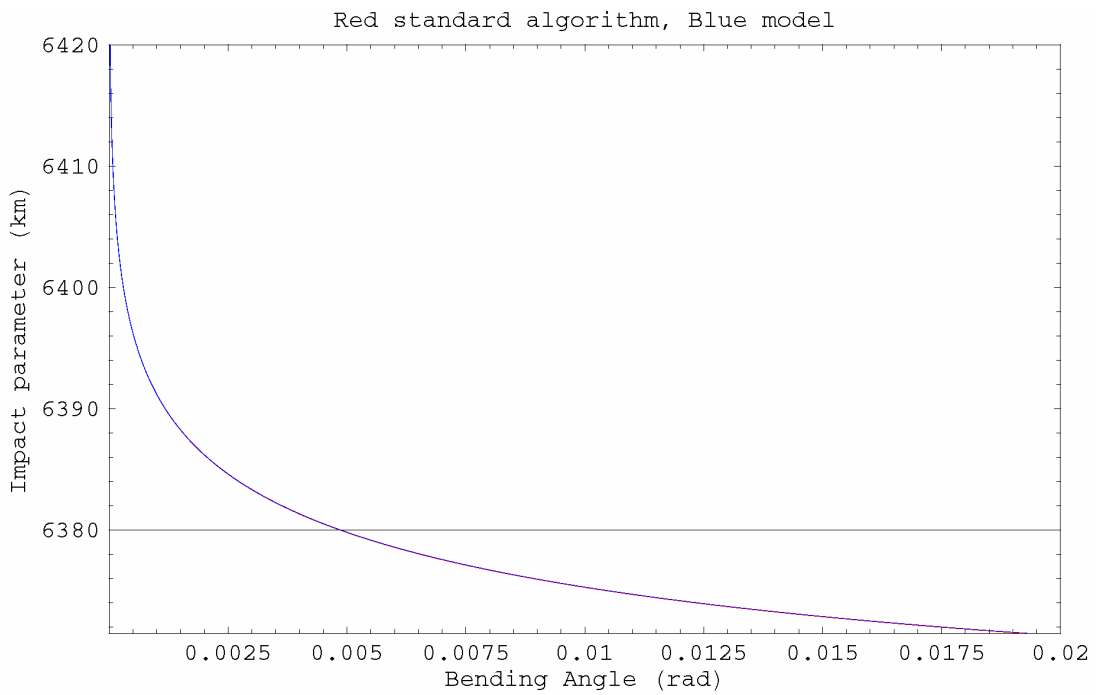
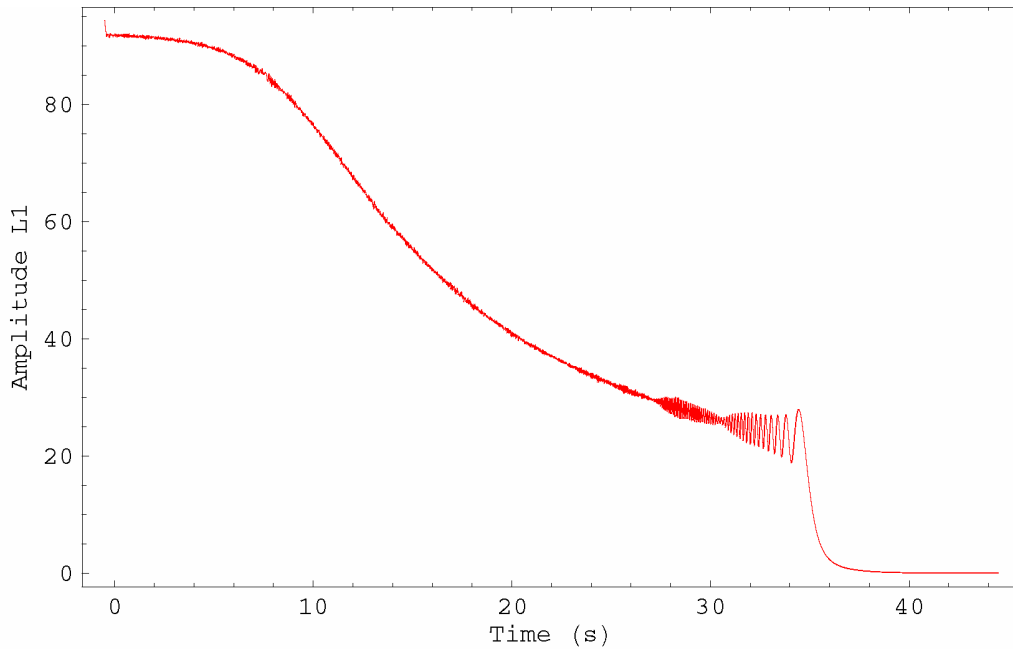


Figure 4-3: Simulation parameters $B=0$ and $BH=5$ km. The upper plot shows the simulated amplitude and the lower plot shows the calculated bending angle (red curve) as a function of impact parameter together with the model bending angle profile (blue curve).

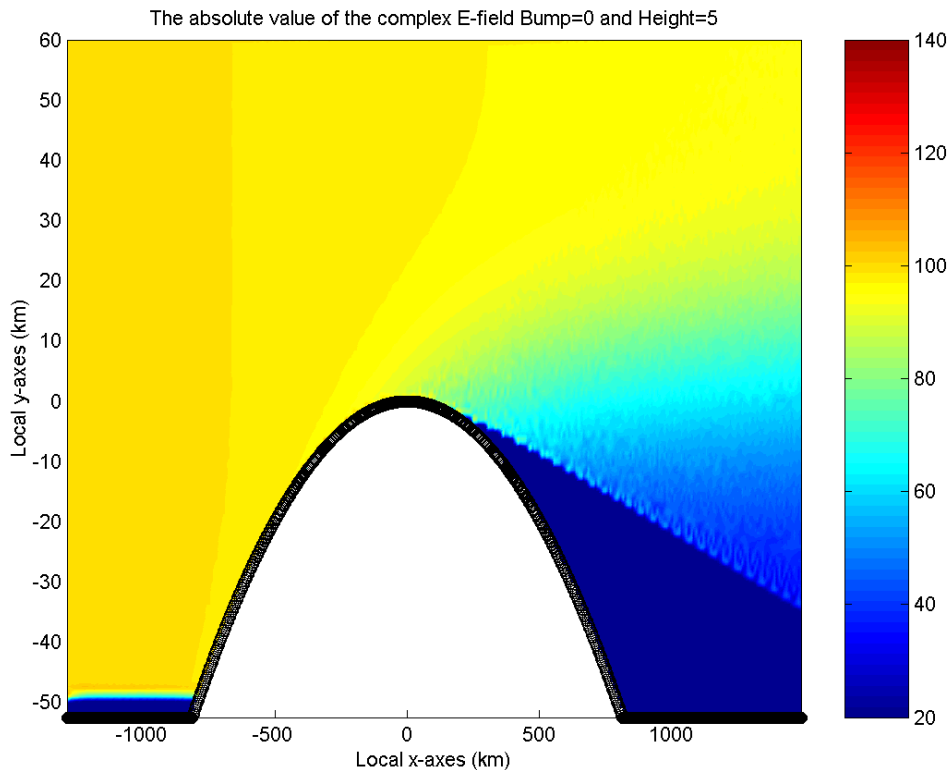


Figure 4-4: Simulation parameters $B=0$ and $BH=5 \text{ km}$. The plot shows a colour plot of the field in the neutral atmosphere. There are no signs of multipath in this plot. The blue colour shows the geometric shadow zone.

No multipath ($B=0$)

In the amplitude versus time plot we see an abrupt exponential drop in the curve at approximately 36 seconds. The limb of the Earth can explain this drop. The smaller fluctuations also seen in the plot are due to boundary effects. Approximations for the boundary conditions are used in the WOP.

We notice from the bending angle versus impact parameter plot that there is a very good agreement between the model bending angle profile and the profile calculated using the occultation signal from the WOP. This bending angle profile (standard algorithm) is calculated using the occultation signal phases and the GPS and LEO satellite positions and velocities.

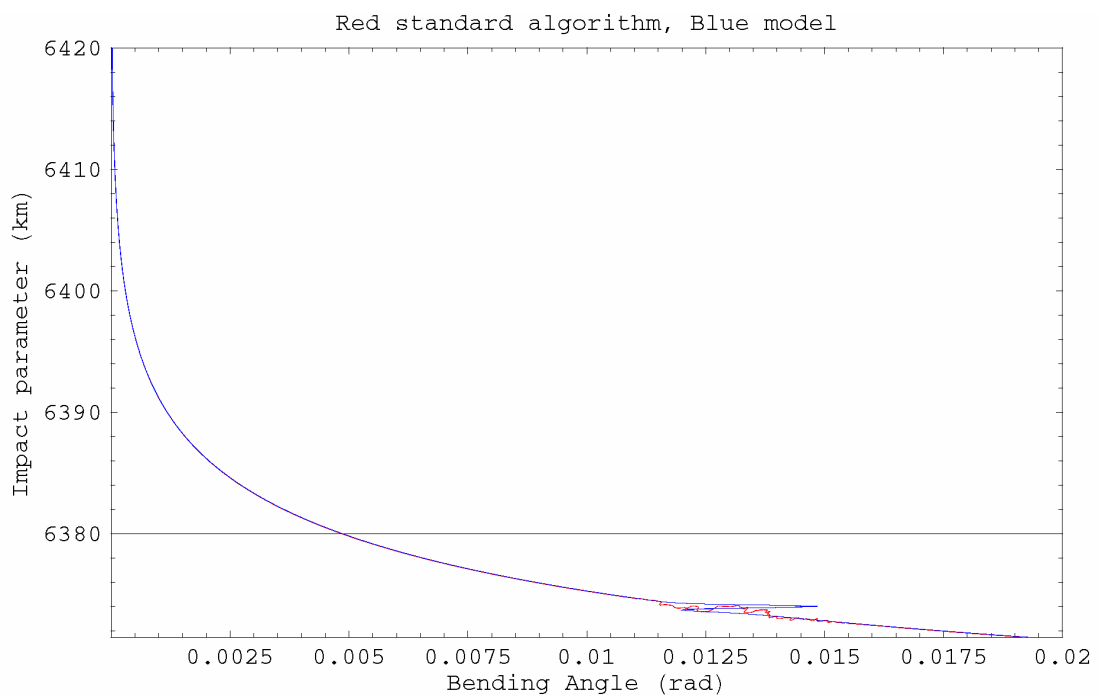
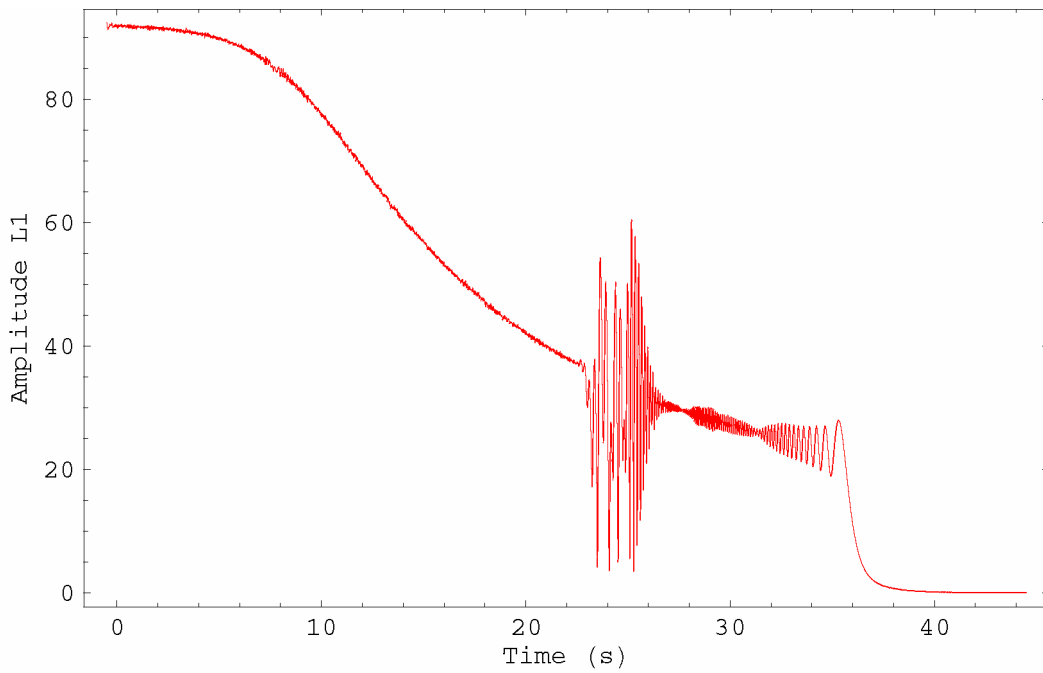


Figure 4-5: Simulation parameters $B=5$ and $BH=5$ km. The upper plot shows the simulated amplitude and the lower plot shows the calculated bending angle (red curve) as a function of impact parameter together with the model bending angle profile (blue curve).

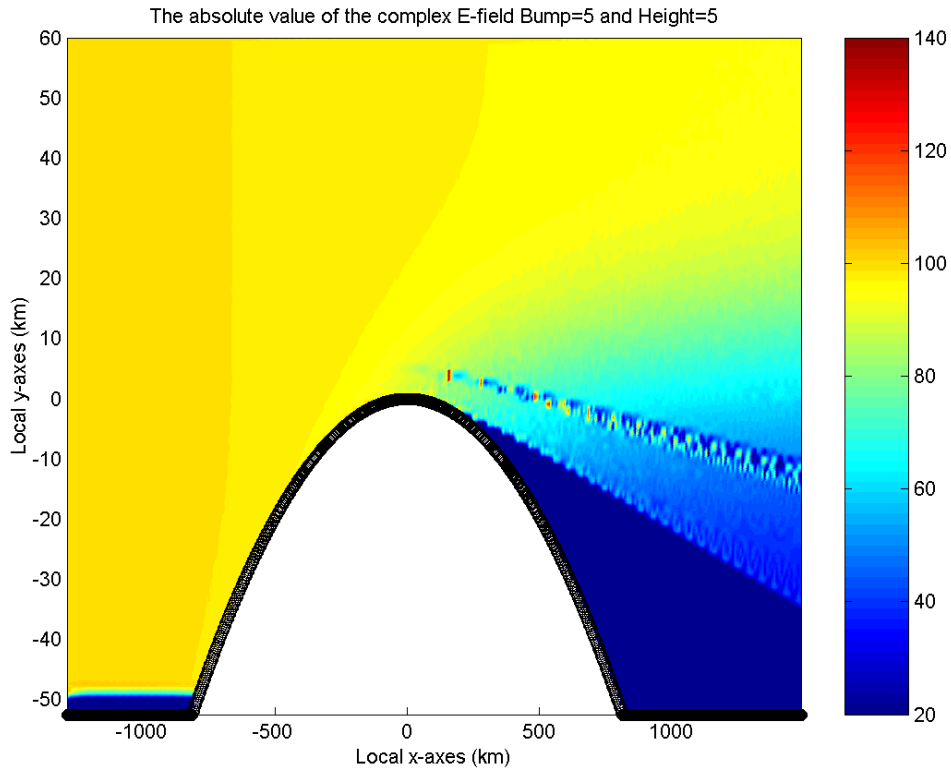


Figure 4-6: Simulation parameters $B=5$ and $BH=5$ km. The plot shows a colour plot of the field in the neutral atmosphere. Signs of multipath are noticed in this plot. The blue colour shows the geometric shadow zone.

Low multipath level ($B=5$)

We notice from the bending angle versus impact parameter plot that there is a relative good agreement between the model bending angle profile and the profile calculated using the occultation signal from the WOP. The S signature in the model bending angle profile is a sign of multipath. This S signature can however (as expected) not be resolved when we use the standard bending angle algorithm. The plot of the absolute value of the complex field in the neutral atmosphere shows also clear signs of the multipath effects present in the occultation signal.

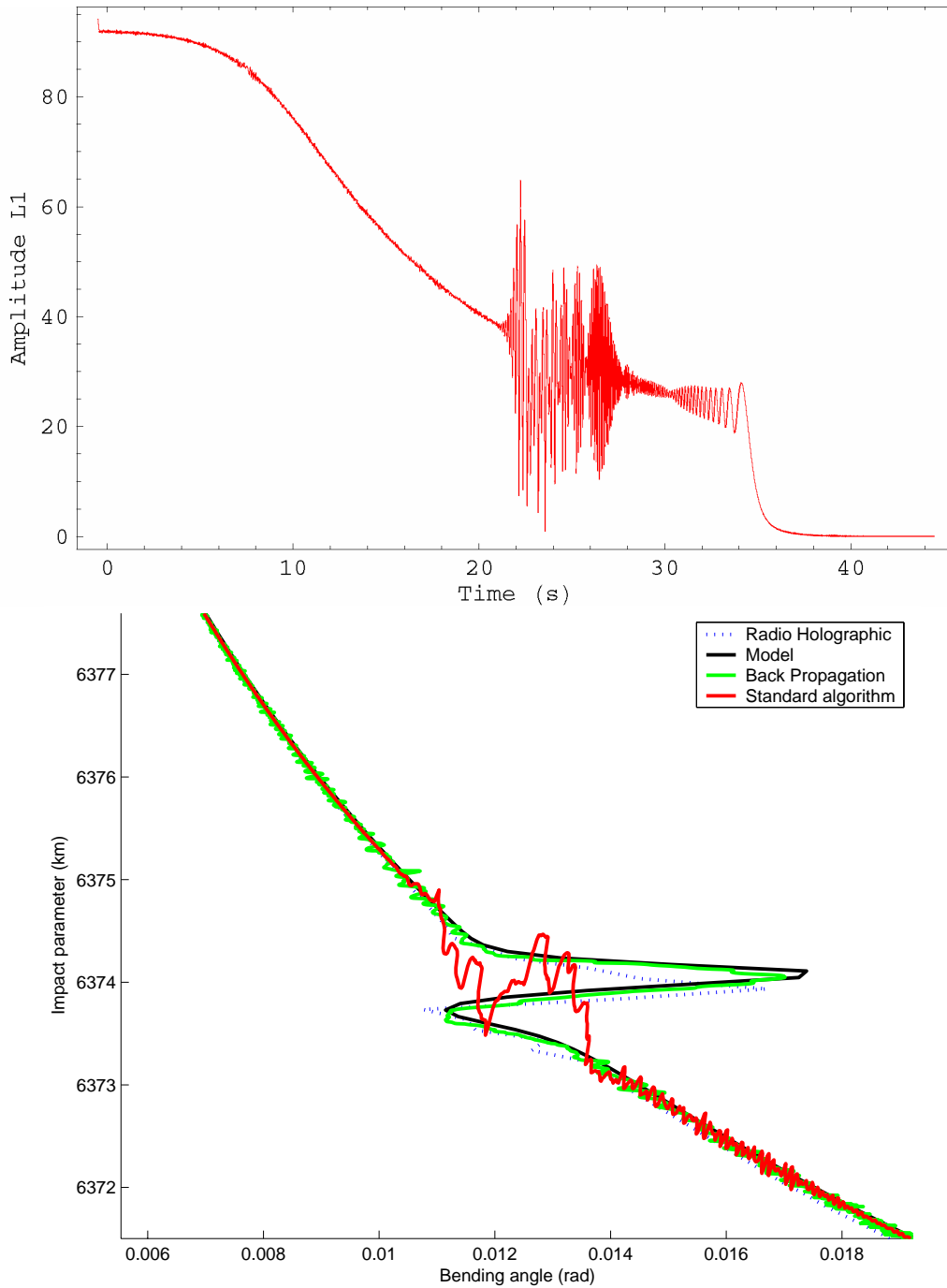


Figure 4-7: Simulation parameters $B=10$ and $BH=5$ km. The upper plot shows the simulated amplitude and the lower plot shows the calculated bending as a function of impact parameter. The bending angle is calculated using the following algorithms: the standard algorithm, the back propagation algorithm, the radio holographic algorithm and finally the model bending angle profile.

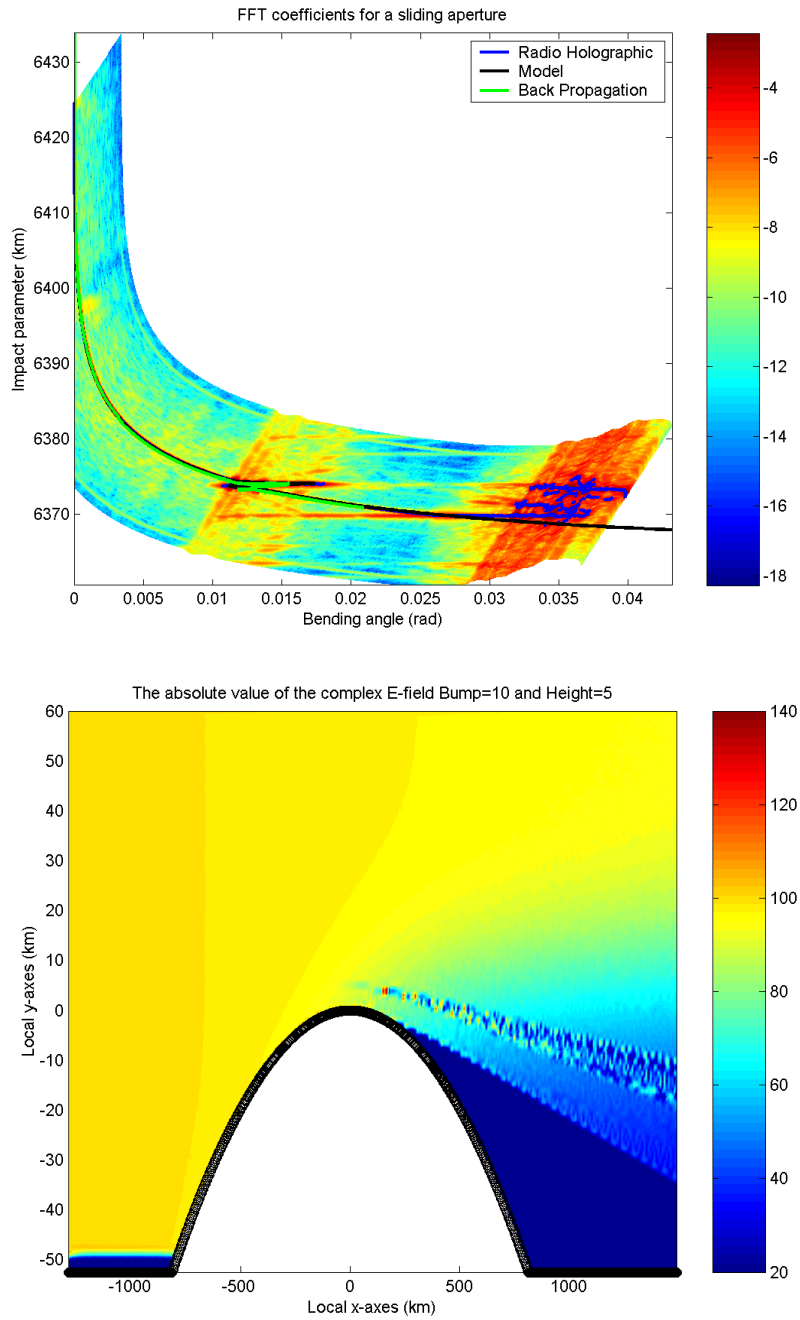


Figure 4-8: Simulation parameters $B=10$ and $BH=5$ km. The upper plot shows the bending angle profile calculated using 3 different algorithms. Also shown is the bending angle versus impact parameter calculated for the entire spectrum of the occultation signal. The lower plot shows a colour plot of the field in the neutral atmosphere. There are strong signs of multipath in this plot. The blue colour shows the geometric shadow zone.

Medium multipath level ($B=10$)

We notice from the bending angle versus impact parameter plot that the agreement between the model bending angle profile and the bending angle profile calculated using the standard algorithm is not so good close to the S signature. The agreement between the model and the radio holographic bending angle profiles are however excellent in this case. The bending angle profile calculated with the use of the back propagation algorithm also indicate the position of the peak in the bending angle but gives in general a less precise result compared to the Radio Holographic technique. The back propagation plane is placed at a distance of 100 km from the occultation point. A different position of the back propagation plane could lead to a bending angle profile where the S signature could be better result. Difference plots and relative difference plots between the bending angle model and bending angles calculated using the Radio Holographic/Back propagation methods can be found in Appendix H.

The plot of the absolute value of the complex field in the neutral atmosphere shows also clear signs of the multipath effects present in the occultation signal.

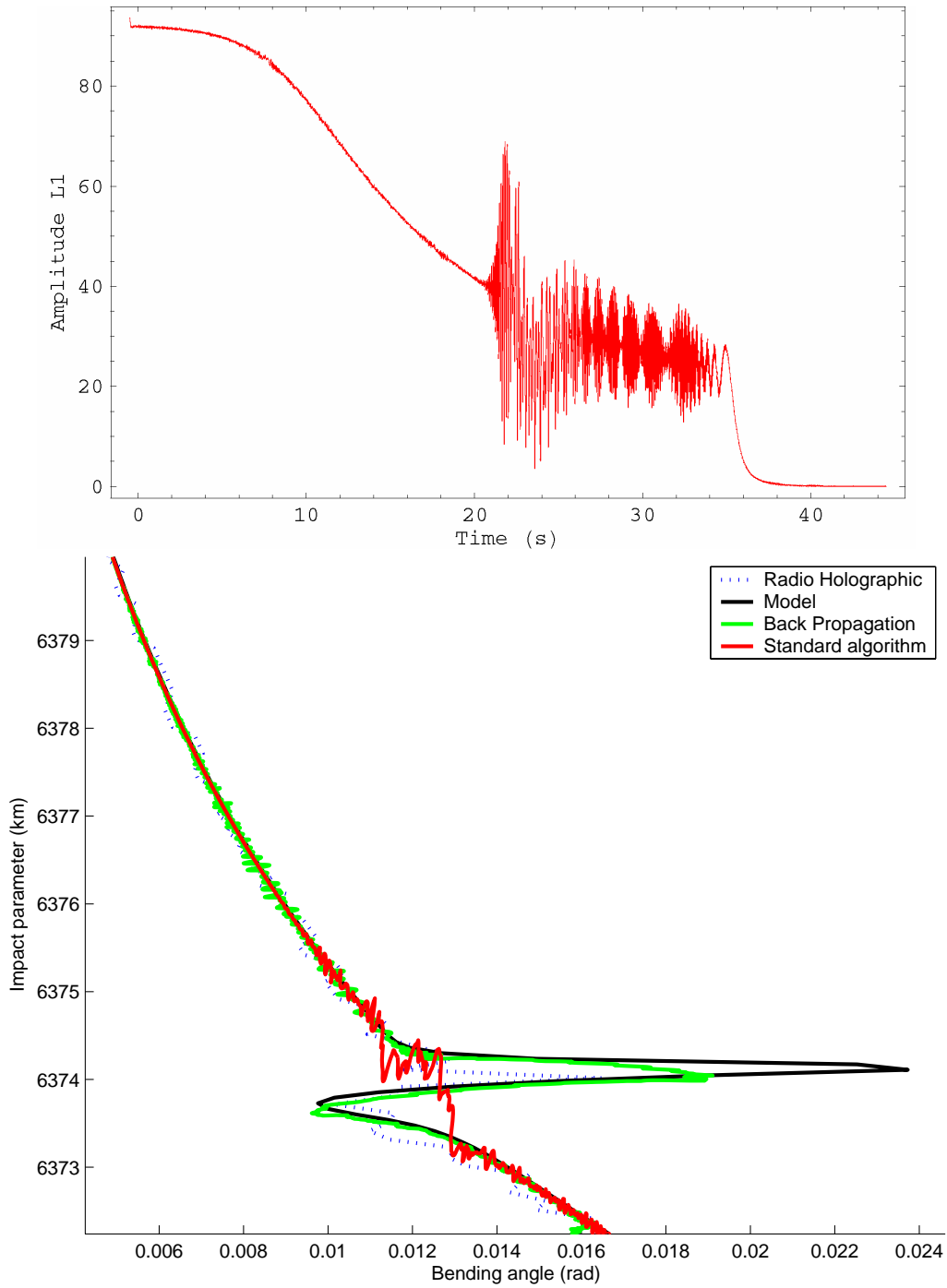


Figure 4-9: Simulation parameters $B=20$ and $BH=5$ km. The upper plot shows the simulated amplitude and the lower plot shows the calculated bending as a function of impact parameter. The bending angle is calculated using the following algorithms: the standard algorithm, the back propagation algorithm, the radio holographic algorithm and finally the model bending angle profile.

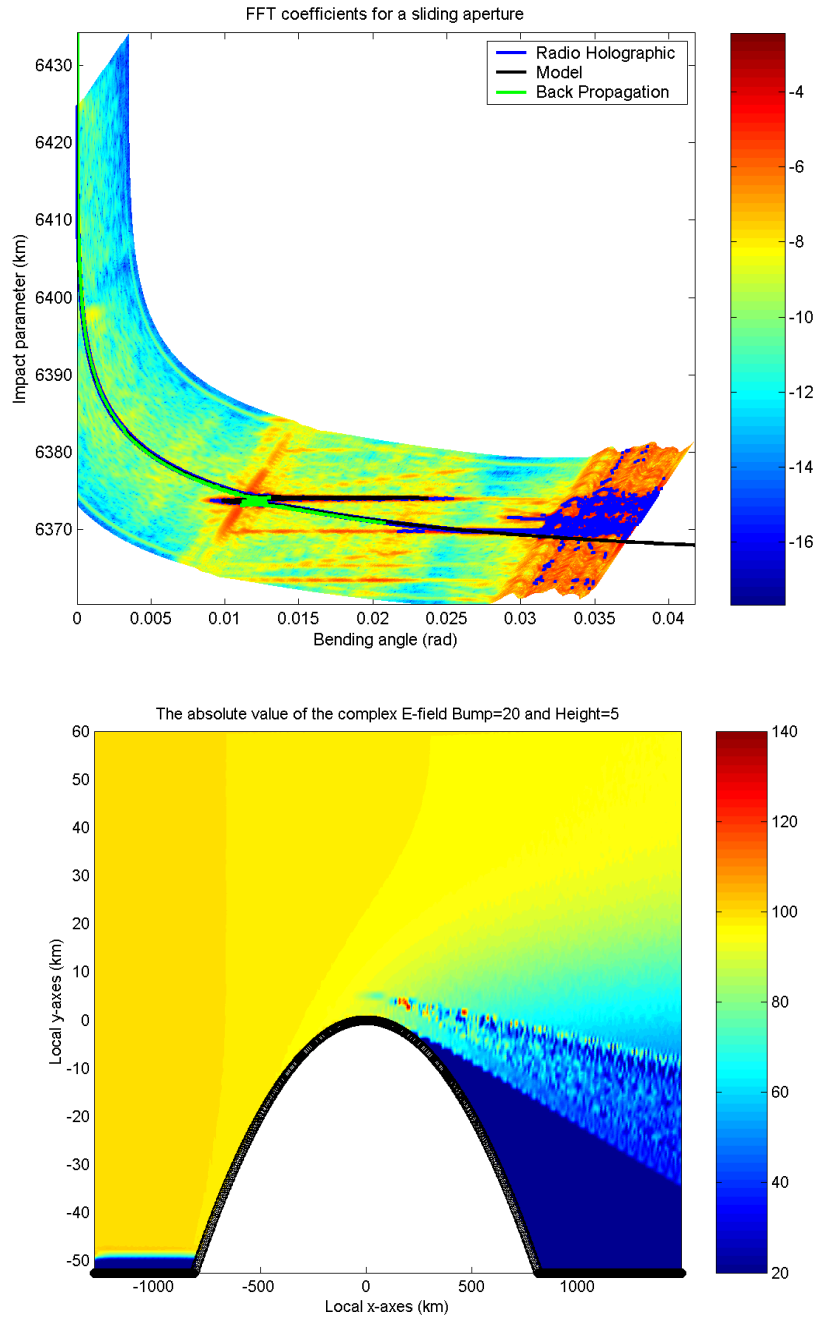


Figure 4-10: Simulation parameters $B=20$ and $BH=5 \text{ km}$. The upper plot shows the bending angle profile calculated using 3 different algorithms. Also shown is the bending angle versus impact parameter calculated for the entire spectrum of the occultation signal. The lower plot shows a colour plot of the field in the neutral atmosphere. There are strong signs of multipath in this plot. The blue colour shows the geometric shadow zone.

High multipath level ($B=20$)

We notice from the bending angle versus impact parameter plot that the agreement between the model bending angle profile and the bending angle profile calculated using the standard algorithm is not so good close to the S signature. The agreement between the model and the radio holographic bending angle profiles are not so good

for $B=20$ as for $B=10$. The radio holographic technique gives however a better result than the back propagation technique.

The back propagation plane is in these simulations placed at a distance of 100 km from the occultation point. A different position of the back propagation plane could lead to a bending angle profile where the S signature could be resolved more properly. The very large peak in the bending angle over a very small distance in the impact parameter is the reason for the weaker performance of the radio holographic technique in its present implementation. A wider bump would increase the precision of the bending angle profile calculated using the radio holographic algorithm. Difference plots and relative difference plots between the bending angle model and bending angles calculated using the Radio Holographic/Back propagation methods can be found in Appendix H.

The plot of the absolute value of the complex field in the neutral atmosphere also exhibits clear sign of the multipath effects present in the occultation signal.

The simulations discussed above shows that there is a good agreement between the model bending angle profiles and the profiles calculated from the phases and amplitudes found from WOP simulations.

This leads to the conclusion that the implementations of the wave propagator, the back propagation algorithm, and the standard bending angle algorithm etc. all are consistent with each other and give the expected results.

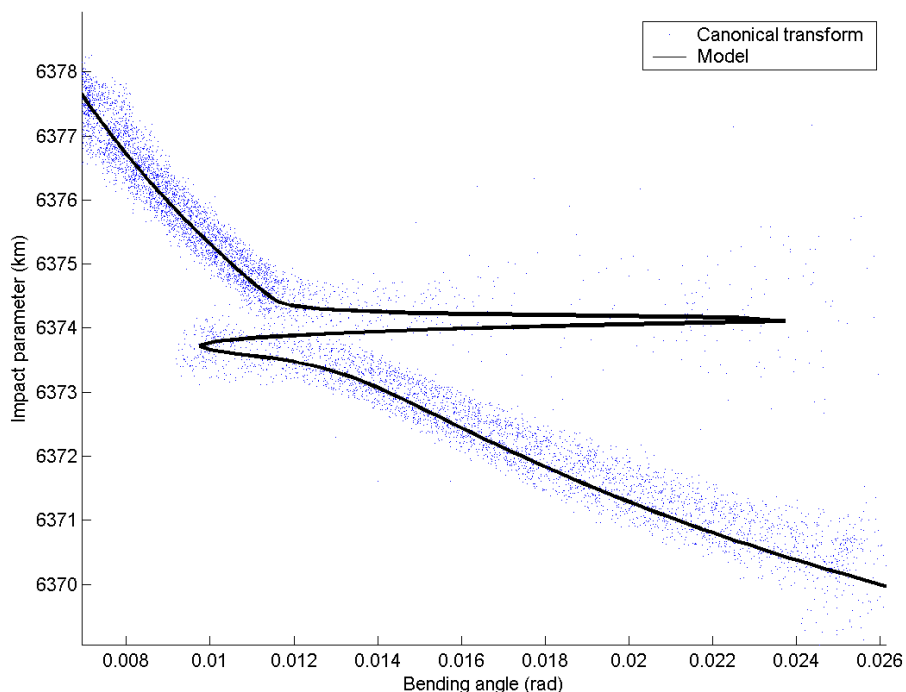


Figure 4-11: Simulation parameters $B=20$ and $BH=5$ km. The plot shows the bending angle vs. impact parameter calculated using canonical transform (blue dots). The model is shown as the solid black line.

Canonical transform result: ($B=20$ and $BH=5$ km)

As part of the validation we have included a plot showing the preliminary results of the canonical transformation compared to the model bending angle (Figure 4.11). In this case the result from the canonical transformation is not better than the one obtained using radio holographic method. However, we will expect that canonical transformation, when fully implemented, should be able to produce superior results compared to the other retrieval methods presented in this document.

Full Spectrum Inversion

Full Spectrum Inversion (FSI) is a new and very promising inversion technique (Jensen et al. 2002) that gives very accurate results when used on a phantom refractivity profile. This method gives more accurate results than the back propagation and the radio holographic method. It can therefore be use to estimate the errors of the wave propagator. The method is applied to the following phantom refractivity profile

$$\begin{aligned} N_A(h) &= 400 \exp(-h/8\text{km}) \\ N_B(h) &= N_B(h) \left[1 - 0.05 \left(\frac{2}{\pi} \right) \tan^{-1} \left(\frac{h - 7\text{km}}{0.05 \text{ km}} \right) \right] \end{aligned} \quad (4-2)$$

The figure below shows the bending angles calculated directly from the phantom refractivity profile and from a wave propagation simulation. We notice that there is a very nice agreement between the two curves and that FSI is able to re-create the very narrow S-signature. The GPS and LEO orbits are the same as in the previous examples.

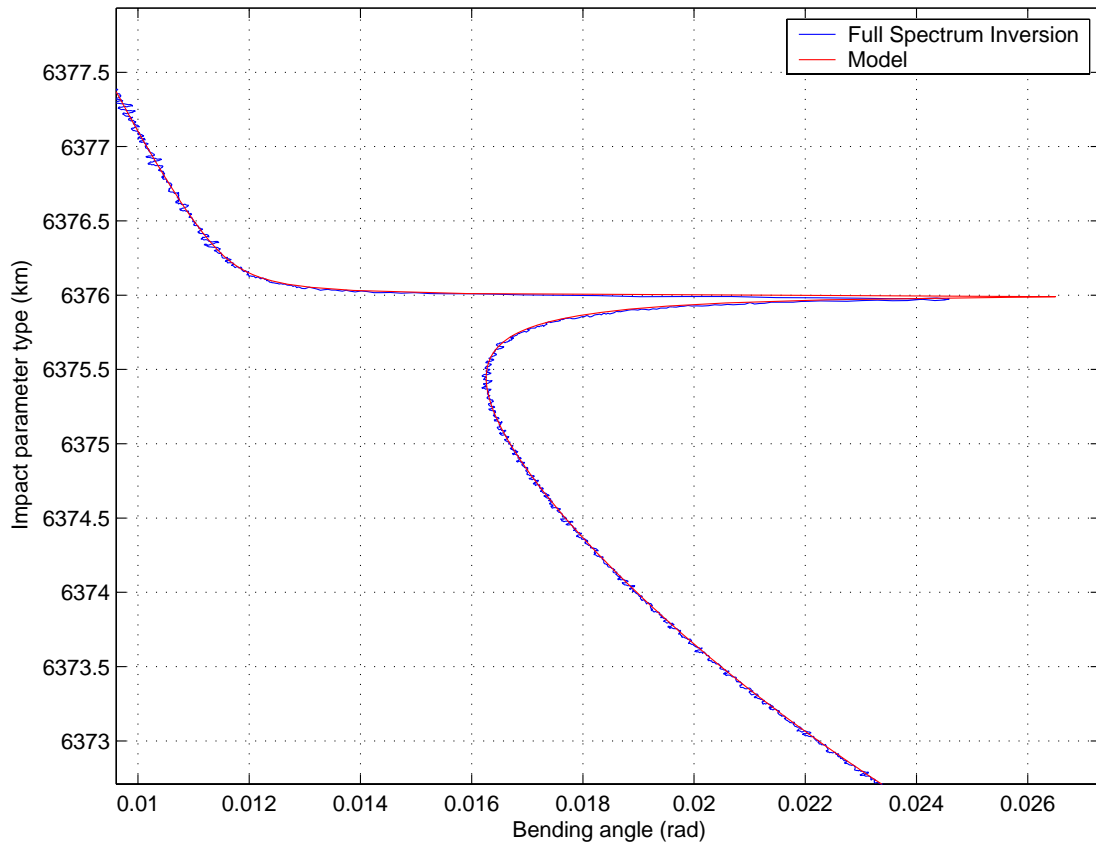


Figure 4-12: The plot shows the bending angle vs. impact parameter calculated using the FSI method (blue curve) together with the model (red curve).

The deviation in percent between the two curves is shown in the plot below and is seen to be very small indicating that the combined error of the wave propagator and the retrieval method must be small. The high peak found at an impact parameter of approximately 6376.3 km can be removed if a moving average scheme is applied to the FSI algorithm. The combined relative error is seen to increase with the impact parameter.

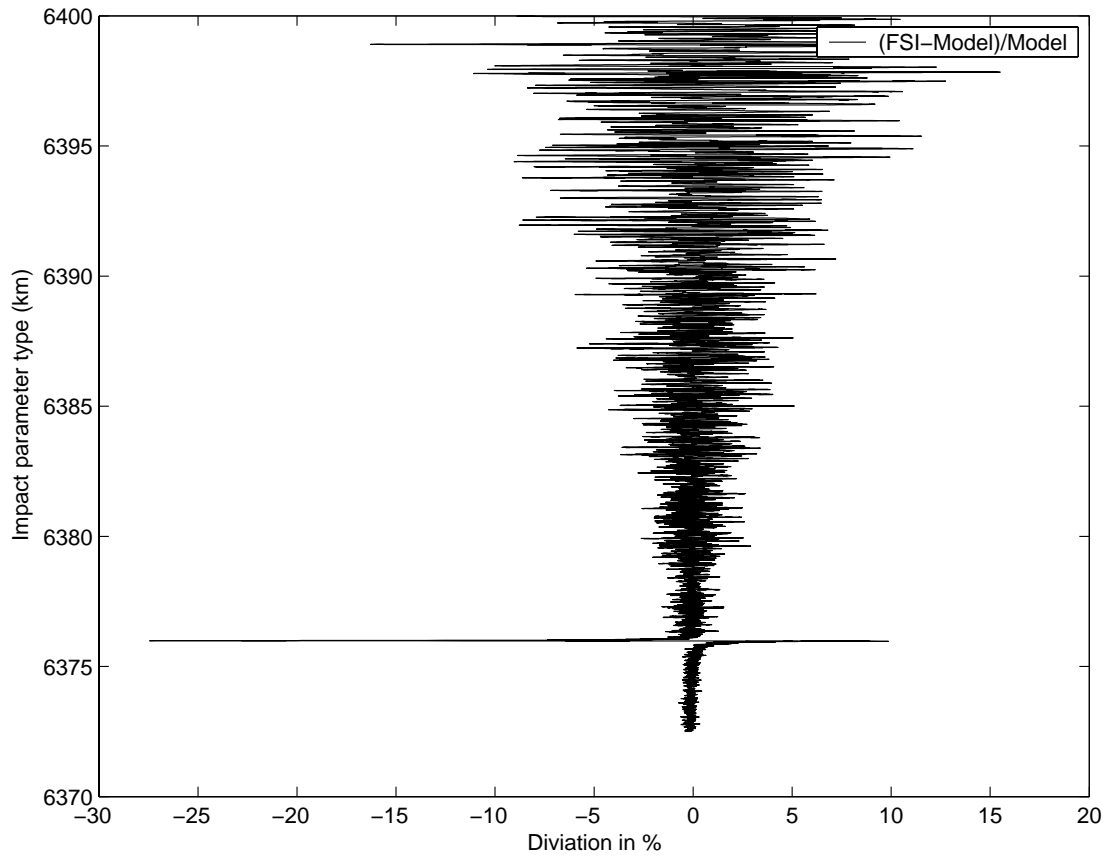


Figure 4-13: The relative difference between the model and the Full Spectrum Inversion (FSI) bending angle profiles.

5 Conclusion

This report has described the electromagnetic theory and mathematical algorithms needed to make a software implementation of a wave propagator to be used in the neutral atmosphere. The limitations and approximations used in the wave propagator have also been discussed in detail.

From the simulations and the validation method described it seems likely that the implementations of the wave propagator, the radio holographic method and the standard bending angle algorithm etc. all are consistent with each other and give the expected results. We also show that the newly developed Full spectrum Inversion (FSI) method performs very well with respect to resolve multipath structures in WOP simulations.

5.1 Acknowledgement

We are very grateful to M.E. Gorbunov for providing us with his wave optics propagator tool and for useful discussions during the development of this report.

6 Appendices

The important sections of the program will, in the following appendices (A-G), be described in more detail. The order of which the appendices appear reflects the algorithm flow in the wave propagator, as depicted in Figure A.0-1 below.

Appendix A: Wave Propagation Flow Chart

The flow chart below gives a detailed view of the computational flow of the wave propagator.

Wave Propagator flow chart

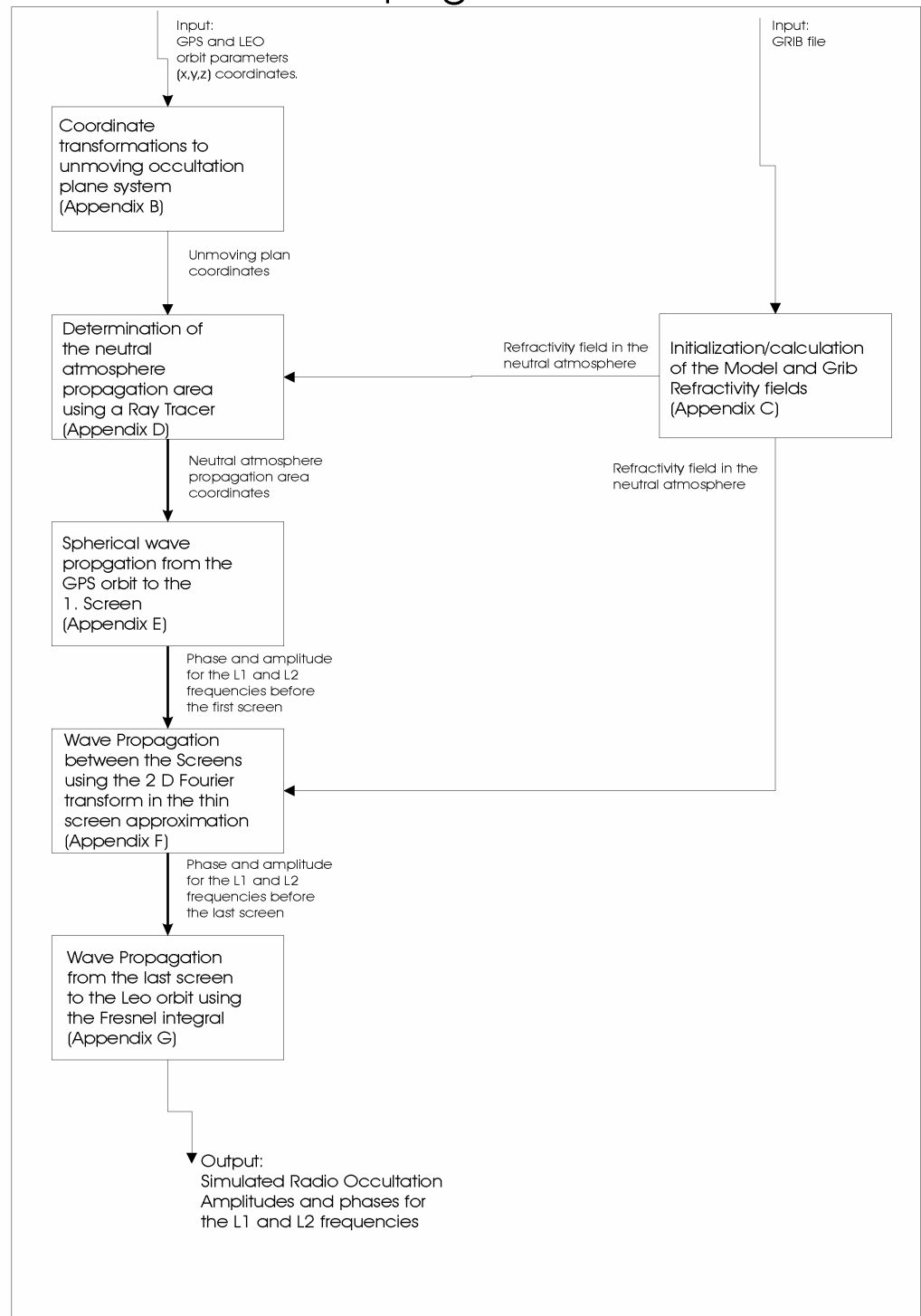


Figure A.0-1: A flow chart representing the computational flow in a Wave Propagator. The algorithms and the input/output for each of the boxes in the diagram are described in the following appendices.

Appendix B: Coordinate Transformations

Transformation from J2000 to Earth Frame Coordinates

Objectives: To transform from J2000 to Earth Frame Coordinates.

Input parameters:

1. Year of occultation, Y .
2. Month of occultation, M .
3. Day of month of occultation, DM .
4. Coordinates in the J2000 system, $(x_{2000}, y_{2000}, z_{2000})$
5. Hour (starting time of occultation)
6. Minute (starting time of occultation)
7. Seconds (starting time of occultation)
8. $Dsec$ (time elapsed since the start of the occultation)

Output parameters:

1. Coordinates in the Earth Frame, (x_E, y_E, z_E)

Constants:

1. Constant term in JD determination, 1720994.5 days.
2. 36525 days per century.
3. JD of January 1, 2000, namely 2451545.0.
4. The conversion factor 1.0027379093 between sidereal and universal time.
5. 86400 seconds per day.
6. The numerical constants 24110.54841, 8640184.812866, 0.093104 and 0.0000062 in the formula that determines GMST of 0h UT1.

The Julian day number, JD , is determined as follows. The operator $\text{int}[\]$ takes the integer part of the real number in the brackets. The first day in a month is day 1.

For each occultation

```
If M<3
    then Y1=Y-1 and M1=M+12
elseif M≥3
    then Y1=Y and M1=M.
endif
```

$$A = \text{int}\left[\frac{Y1}{100}\right] \quad (\text{B-1})$$

$$B = 2 - A + \text{int}\left[\frac{A}{4}\right] \quad (\text{B-2})$$

$$C = \text{int}[365.25 \cdot Y1] \quad (\text{B-3})$$

$$D = \text{int}[30.6001 \cdot (M1 + 1)] \quad (\text{B-4})$$

$$JD = B + C + D + DM + 1720994.5 \quad (\text{B-5})$$

Form the parameter

$$T_u = \frac{JD - 2451545.0}{36525} \quad (\text{B-6})$$

then GMST of 0h UT1 of the given day, is given by the formula

$$\begin{aligned} \text{GMST of 0h UT1} = & 24110.54841 + 8640184.812866 \cdot T_u \\ & + 0.093104 \cdot T_u^2 - 6.2 \cdot 10^{-6} \cdot T_u^3 \end{aligned} \quad (\text{B-7})$$

which is counted in seconds. The contribution according to the time of day (tod) is

$$\text{tod(UT1)} = \text{hour} \cdot 3600 + \text{minute} \cdot 60 + \text{seconds} + D \text{ sec} \quad (\text{B-8})$$

In sidereal time tod is

$$\text{tod(sidereal)} = \text{tod(UT1)} \cdot 1.0027379093 \quad (\text{B-9})$$

GMST is then obtained as

$$\text{GMST} = \text{mod}(\text{GMST of 0h UT1} + \text{tod(sidereal)}, 86400) \quad (\text{B-10})$$

Finally, GMST is converted into an angle

$$\gamma = \text{GMST} \cdot \frac{2\pi}{86400} [\text{rad} / \text{s}] \quad (\text{B-11})$$

end for each occultation.

For each sample
Do the following transformation

$$\begin{pmatrix} x_E \\ y_E \\ z_E \end{pmatrix} = \begin{bmatrix} \cos \gamma & \sin \gamma & 0 \\ -\sin \gamma & \cos \gamma & 0 \\ 0 & 0 & 1 \end{bmatrix} \begin{pmatrix} x_{2000} \\ y_{2000} \\ z_{2000} \end{pmatrix}. \quad (\text{B-12})$$

end for each sample.

Transformation from Geodetic to Earth Frame Coordinates

Objectives: To transform from Geodetic to Earth Frame coordinates

Input parameters:

1. Geodetic coordinates (φ, λ, h)

Output parameters:

1. Coordinates in the Earth Frame, (x_E, y_E, z_E)

Constants:

1. The Earth's semi major axis, $a=6378137$ meter.
2. The Earth's flattening, $f=1/298.2572$.

Algorithm

For each sample:

First calculate

$$rcp = \frac{a}{\sqrt{1 - (2 - f)f \sin^2 \varphi}} \quad (\text{B-13})$$

then

$$x_E = \cos \varphi \cdot \cos \lambda \cdot (rcp + h) \quad (\text{B-14})$$

$$y_E = \cos \varphi \cdot \sin \lambda \cdot (rcp + h) \quad (\text{B-15})$$

$$z_E = \sin \varphi \cdot (rcp \cdot (1 - f)^2 + h) \quad (\text{B-16})$$

end for each sample.

Transformation from Earth Frame to Geodetic Coordinates

Objectives: To transform from Earth Frame to Geodetic coordinates

Input parameters:

1. Coordinates in the Earth Frame, (x_E, y_E, z_E)

Output parameters:

1. Geodetic coordinates (φ, λ, h)

Constants:

The following constants are used in the program:

1. The Earth's eccentricity squared $e = e^2 = 0.006694380$
2. The Earth's major semi axis $a=6378137$ meters.
3. The Earth's minor semi axis $b=6356752,3$ meters.

All constants are in according to the Geodetic Reference System 1980.

Algorithm

This is an approximate method.

For each sample

The longitude is given by

$$\lambda = \arctan\left(\frac{y_E}{x_E}\right) \quad (\text{B-17})$$

Define some convenient parameters.

$$R_{xy} = \sqrt{x_E^2 + y_E^2} \quad (\text{B-18})$$

$$\Theta = \arctan\left(\frac{z_E \cdot a}{R_{xy} \cdot b}\right) \quad (\text{B-19})$$

then the latitude is

$$\varphi = \arctan\left(\frac{z_E + e \cdot b \cdot \sin^3 \Theta}{R_{xy} - e \cdot a \cdot \cos^3 \Theta}\right) \quad (\text{B-20})$$

and with

$$\arg = (b^2 - z_E^2) \cos^2 \varphi + (a^2 - Rxy^2) \sin^2 \varphi + 2Rxy \cdot z_E \cos \varphi \sin \varphi \quad (\text{B-21})$$

the height above the reference ellipsoid become

$$h = \frac{-(-b^2 Rxy \cos \varphi - a^2 z_E \sin \varphi + ab\sqrt{\arg})}{b^2 \cos^2 \varphi + a^2 \sin^2 \varphi} \quad (\text{B-22})$$

end for each sample.

Transformation from J2000 to Occultation Plane Coordinates

Objectives: To transform from J2000 to Occultation Plane coordinates.

Input parameters:

1. GPS and LEO position vectors in J2000, \overline{RGPS} and \overline{RLEO} .
2. The Earth's semi major axis, a .
3. The Earth's eccentricity, e .
4. The geodetic latitude, ϕ , of the occultation point.

Output parameters:

1. Basis vectors, AX and AY , for the moving occultation plane coordinate systems.
2. GPS and LEO positions, both represented here as $(x_{\text{mov}}, y_{\text{mov}})$, in moving occultation plane coordinates.

Constants:

No constants are used in the program.

Algorithm:

For each sample

The unit vectors \overline{NG} and \overline{NL} is determined

$$\overline{NG} = \frac{\overline{RGPS} - \overline{RLC}}{\|\overline{RGPS} - \overline{RLC}\|} \quad (\text{B-23})$$

and

$$\overline{NL} = \frac{\overline{RLEO} - \overline{RLC} - ((\overline{RLEO} - \overline{RLC}) * \overline{NG}) * \overline{NG}}{\|\overline{RLEO} - \overline{RLC} - ((\overline{RLEO} - \overline{RLC}) * \overline{NG}) * \overline{NG}\|} \quad (\text{B-24})$$

The local radius of curvature is given by

$$R_c = \frac{1}{\frac{\cos^2 \alpha}{rcm} + \frac{\sin^2 \alpha}{rcp}} \quad (\text{B-25})$$

where

$$rcp = \frac{a}{(1 - e^2 \sin^2 \varphi)^{1/2}} \quad (\text{B-26})$$

$$rcm = \frac{a(1 - e^2)}{(1 - e^2 \sin^2 \varphi)^{3/2}} \quad (\text{B-27})$$

The angle between the NG vector and the curvature radii can be determined approximately by

$$\cos(\beta) = \frac{R_c}{\|\overrightarrow{RGPS} - \overrightarrow{RLC}\|} \quad (\text{B-28})$$

then

$$\sin(\beta) = \sqrt{1 - \cos^2(\beta)}. \quad (\text{B-29})$$

The Moving Occultation Plane Systems basis vectors are

$$\overline{AX} = \cos(\beta) \cdot \overline{NL} - \sin(\beta) \cdot \overline{NG} \quad (\text{B-30})$$

and

$$\overline{AY} = \sin(\beta) \cdot \overline{NL} + \cos(\beta) \cdot \overline{NG}. \quad (\text{B-31})$$

The coordinates of the GPS or LEO satellite in the Moving Occultation Planes are given by

$$x_{\text{mov}} = \overline{AX} * ((x_{2000} - x_{RLC}), (y_{2000} - y_{RLC}), (z_{2000} - z_{RLC})) \quad (\text{B-32})$$

and

$$y_{\text{mov}} = \overline{AY} * ((x_{2000} - x_{RLC}), (y_{2000} - y_{RLC}), (z_{2000} - z_{RLC})) \quad (\text{B-33})$$

where $(x_{2000}, y_{2000}, z_{2000})$ and $(x_{\text{mov}}, y_{\text{mov}})$ are the position of either the LEO or the GPS satellite.

end for each sample.

The coordinates in the moving occultation coordinate systems are used as approximate values of the coordinates in the (fixed) occultation plane coordinate system.

Transformation from Occultation Plane to Unmoving GPS System Coordinates

Objectives: To transform from Occultation Plane to unmoving GPS System coordinates

Input parameters:

1. Coordinates of LEO and GPS satellites in Occultation Plane system, $(XLEO, YLEO)$ and $(XGPS, YGPS)$.
2. Time index of ray of lowest height, $iocc$.

Output parameters:

1. LEO and GPS coordinates in Unmoving GPS system, $(XLEO_{unmov}, YLEO_{unmov})$ and $(XGPS_{unmov}, YGPS_{unmov})$, respectively.

Constants:

No constants are used in the program.

Algorithm:

For each sample

Form the function $F(i)$

$$F(i) = \frac{XLEO(i) \cdot XGPS(i)}{XLEO(i) - XGPS(i)} \quad (\text{B-34})$$

where i is the time index. Then the new LEO coordinates are given by

$$XLEO_{unmov}(i) = \frac{F(i) \cdot XGPS(iocc)}{F(i) - XGPS(iocc)} \quad (\text{B-35})$$

and

$$YLEO_{unmov}(i) = YLEO(i) - R_c \quad (\text{B-36})$$

The GPS coordinates for each sample is set to

$$XGPS_{unmov}(i) = XGPS(iocc) \quad (\text{B-37})$$

and

$$YGPS_{unmov}(i) = YGPS(iocc) - R_c \quad (\text{B-38})$$

end for each sample.

Appendix C: GRIB Files

GRIB is a WMO format for gridded data. GRIB is used by the operational meteorological centres for storage and the exchange of gridded fields. GRIB's major advantages are files are typically 1/2 to 1/3 of the size of normal binary files (floats), the fields are self-describing, and GRIB is an open, international standard.

The World Meteorological Organization (WMO) Commission for Basic Systems (CBS) Extraordinary Meeting Number VIII (1985) approved a general purpose, bit-oriented data exchange format, designated FM 92-VIII Ext. GRIB (GRIdded Binary). It is an efficient vehicle for transmitting large volumes of gridded data to automated centers over high-speed telecommunication lines using modern protocols. By packing information into the GRIB code, messages (or records - the terms are synonymous in this context) can be made more compact than character oriented bulletins, which will produce faster computer-to-computer transmissions. GRIB can equally well serve as a data storage format, generating the same efficiencies relative to information storage and retrieval devices.

Changes and extensions to GRIB were approved at the regular meeting of the WMO/CBS in February 1988; additional changes were introduced at the CBS/WGDM/Sub-Group on Data Representation (SGDR) meetings in May 1989 and in October 1990. The 1990 changes were of such structural magnitude as to require a new Edition of GRIB, Edition 1, which this document describes. Further augmentations and interpretations were made by the SGDR in September 1993, with approval by the WGDM in February 1994. These changes did not result in a new Edition to GRIB, but did change some of the Tables, resulting a new Table Version number for them (2). The changes from Version 1 were mainly additions of new parameters or more precise definition of existing ones. Additional changes to the GRIB Tables were adopted at an Expert Meeting of the SGDR in September 1995, which now brings us to Table Version 3.

It is not anticipated that there will be any large-scale structural changes to GRIB for at least four to five years, or more. The SGDR is undertaking a thorough review of the present and future requirements that GRIB is supposed to satisfy. The plan is to design a major revision of GRIB capable of accommodating these requirements and more, without "straining" the structure of the data representation form. Some things are getting a little strained even now.

Note: the Edition number is placed in the same location, relative to the start of the GRIB message, for all Editions. Thus, decoding programs can detect which Edition was used to construct a particular GRIB message and behave accordingly. This is useful for archives of messages encoded in earlier Editions or during transition periods. Of course, this requires that data centers retain copies of older editions of the code, and older versions of the parameter tables.

Each GRIB record intended for either transmission or storage contains a single parameter with values located at an array of grid points, or represented as a set of spectral coefficients, for a single level (or layer), encoded as a continuous bit stream. Logical divisions of the record are designated as "sections", each of which provides

control information and/or data. A GRIB record consists of six sections, two of which are optional:

- 0) Indicator section
- 1) Product Definition section (PDS)
- 2) Grid Description section (GDS) - optional
- 3) Bit Map section (BMS) - optional
- 4) Binary Data section (BDS)
- 5) '7777' (ASCII Characters)

Although the Grid Description section is indicated as optional, it is highly desirable that it be included in all messages. That way there will be no question about just what is the "correct" geographical grid for a particular field.

Most centers require bulletin headers to enable them to receive, identify, and switch messages; NCEP is no exception. In this documentation, certain symbols are used to clarify the contents of octets (groups of eight consecutive binary bits, "bytes" in American usage). If unadorned letters are used, they are symbolic and their meanings are described in the text; a decimal number is simply printed as is; a character or string of characters is represented inside single quote marks. International Alphabet No. 5, which is identical in its essential elements to the U.S. National Standard 7-bit ASCII, is used for character representation in the GRIB code.

Octets are numbered consecutively from the start of each section; bits within an octet are also numbered from left (the most significant bit) to right (the least significant bit). Thus an octet with bit 8 set to the value 1 would have the integer value 1; bit 7 set to one would have a value of 2, etc. The numbering of Tables in the following text corresponds to the description of GRIB in the WMO Manual on Codes 1. Some additional tables not found in the WMO Manual are indicated by letters. These, generally, contain information unique to the NWS or NOAA.

A caveat: The Official International Documentation for GRIB is the just referenced Manual on Codes. This document is, in part, intended to be a guide to the use of GRIB and may not include all of the features currently found in the Manual. It does, however, represent the full set of features used by the National Weather Service, in particular in the AWIPS project, and by the National Centers for Environmental Prediction. The features described here are intended to be a completely consistent subset of the full WMO documentation; if there is any discrepancies the Manual on Codes is the final authority.

DATA PACKING METHODS

The code form represents numeric data as a series of binary digits (bits). Such data representation is independent of any particular machine representation; by convention data lengths are measured in octets. Data are coded as binary integers using the minimum number of bits required for the desired precision. Numeric values may first be scaled by a power of ten to achieve an appropriate decimal precision, a reference value is subtracted from them to reduce redundancy and eliminate negative values, and they may then be further scaled by a power of two to pack them into a pre-selected word length. The two scaling operations are independent; which, or both, are used in any given case depends upon choices made as to the method of packing.

The representation of a single value is such that:

$$Y * 10^D = R + (X * 2^E)$$

where

Y = original or unpacked value;

D = decimal scale factor, to achieve desired precision

(sign bit, followed by a 15-bit integer);

R = reference value (32 bits);

X = internal value (No. of bits varies for each record);

E = binary scale factor for variable bit word length packing

(sign bit, followed by a 15-bit integer).

The reference value (R) is the minimum value of the (possibly) decimally scaled data that is being encoded.

R is placed in the Binary Data section in four octets as a single precision floating-point number:

sAAAAAAAA BBBB BBBB BBBB BBBB

where s = sign bit, encoded as 0 means positive

1 means negative

A...A = 7-bit binary integer, the characteristic

B...B = 24-bit binary integer, the mantissa.

The appropriate formula to recover the value of R is:

$$R = (-1)^s * 2^{-(24)} * B * 16^{(A-64)}$$

This formula is the standard IBM representation for a single precision (real) floating point number. (Consideration is being given to using the IEEE floating point representation in the future, in a later Edition of GRIB.)

If second order (or "complex") packing is used (see the description of that later on) the internal value, X, will be made up of two values, a "local minimum value", X_i , and a "second order packed value", X_j . There will be one X_j for each grid point and a variable number of X_i values. This will all come clear later on when we get to the description of second-order packing.

What follows is a description, slightly simplified, of the process that one would go through to pack a (meteorological) field into a GRIB message, using "simple packing". It includes some explanations of why certain steps are taken, some of the consequences, and what choices have to be made. Some of the choices are interrelated; the relationships should be clear when the explanation is done. The additional features of complex or "second order" packing will be dealt with in a later section.

Given that a full field is available, the first step, if necessary, is to convert the units of the parameter into those shown in Table 2, the SI standard units, also known as the *MKS system*. Some of the units may seem a little peculiar (kg/m^2 , for example, for precipitation - 1 kg/m^2 is equivalent to a water depth of 1 mm); others may seem inappropriate (Pa for pressure, for example, implies substantially greater precision than is typical in meteorological usage; inverse seconds are not nearly precise enough for divergence and vorticity) but they are all self-consistent. The precision of the parameters, as actually packed in a message, can be set to any desired degree through the appropriate use of the power-of-10 ("D") scaling

and the power-of-2 ("E") scaling. Just how this comes about will be described momentarily.

At this point there is a choice to be made. If it is desired to use a pre-selected bit word length for the packed variables, then just proceed on to the next step. However, if a variable bit word length is to be used, where the word length is adjusted to accommodate the data values, then it is necessary to undertake the power-of-ten scaling. The D value should be selected such that, when the original data in the SI units is multiplied by 10^D , the integer part of the result will have enough precision to contain all the appropriate information of the variable.

Anticipating things a little bit, the (scaled) value will be rounded to an integer as a part of the packing process; thus the "significant part" of the value of the variable has to be moved to the left of the decimal point prior to the rounding. Temperature might be scaled with $D=1$, thus changing the units to deci-degrees; pressure, on the other hand, might be scaled with $D=-2$, thus actually reducing the precision to hecto Pascals (mb), a more reasonable meteorological precision; vorticity would be scaled up by $D=8$, and so on.

The second step in the packing operation is to scan through the field, which may or may not have been "D-scaled" at this point, find the minimum value of the parameter, and subtract that minimum - the reference value, R - from all the data points, leaving a residual of non-negative numbers. This step has two benefits. The first of these is convenience - making all the data points non-negative bypasses problems with different computer hardware that represent negatives in various ways: 1's complement, 2's complement, signed positive integers, whatever.

The GRIB message is rendered just that much more machine independent by being non-negative throughout. The second benefit is more consequential: it can result in a substantial compression of the bulletin size without any loss of information content. If a field has an appreciable bias away from zero, the residuals formed by the minimum removal operation will all be much smaller numbers than otherwise. Thus they will need fewer bits to contain them when they are, eventually, packed as integers.

The third step is simply to scan through the field of residuals and find the maximum value. At this point another choice must be made, similar to the one made previously. This time, if a variable bit word length is to be used, then it is necessary to calculate how many bits (per word or per data grid point) are going to be needed to contain that largest data value, when the latter has been rounded to an integer. Recall that at the previous decision point, the variables were power-of-ten ("D") scaled such that a rounding operation will preserve all the significant part of the information.

Discovering how many bits are needed is a simple scan through a table of powers of two, of course. The power-of-two-scaling is not employed and E is set equal to 0. Then go on to the fourth step.

If, alternatively, it is desired to use a pre-selected bit word length for the packed variables, the data must now be scaled, this time by a power of two (the "E" scaling), sufficient to either reduce the maximum value down to just fit into the available number of bits, or enlarge the value to just fit. This latter step takes care of the problem of small numbers where the precision is all in the fractional part of the

number. How much precision is retained, for the eventual rounding, is a function of the pre-selected bit word length and the "typical" range, or maximum value with the minimum removed, of the particular variable.

The choice of bit word length, which is made ahead of time, must be made with full knowledge of the characteristics of the particular variable that is to be packed and a prior assumption of how much precision needs to be retained for the largest likely value. The fourth step is then to round all the values to integers, now that they have all been scaled to appropriate units, and pack them in the specified bit length words.

The last step is then to set up the various identification fields and put the GRIB bulletin in proper form. We shall turn to this "proper form" in the next section.

We have ended up with two alternate ways to construct a GRIB messages: a fixed bit word length method and a variable bit word length method. What are the relative advantages or disadvantages, or at least the differences, of one with respect to the other?

Message length: the fixed word length bulletins are always the same length, for a given parameter; the variable word length bulletins are, naturally, variable. The variation is driven by the range of the value of the parameter over the field (or the maximum value), which can change from day to day. Whether variations in message length is a problem or not depends on the computer systems used to work with the GRIB records.

Precision: The variable word length bulletins have a fixed and unchanging precision, determined by the "D" scaling. This assures that the same information content is available day after day. It is straightforward to change the precision in a familiar manner, that is, simply by orders of magnitude, just by altering the *D* value. This comes at a cost, of course; increasing the precision by a power of 10 adds about 3.3 bits (average) to each data point in the message. The fixed word length bulletins show a variable precision which is case by case data driven and is determined by the "E" (power-of-two) scaling that was used to fit the numbers into the available space. This can happen even with the same data, on the same date, but at adjacent grid areas. If one area shows a low variability and the neighboring one a high variability such that a different power-of-two scaling is needed in the two areas, then, unfortunately, the values on a common boundary will not be exactly equal after they are unpacked. This can be disconcerting and a cause for confusion. It will not happen if D-scaling (only) is employed.

On the other hand, the variable precision can be viewed as a strength: a data field with a low variability will be encoded at a higher precision, thus preserving the character of the field; a high variability field will be represented with less precision, but that is not a problem as the small, and possibly lost, variations will not matter in the presence of the large ones. The precision of the encoded field can be increased by adding bits to the fixed word length, but the degree of change (a power of 2 for each bit) may not be as easy to deal with (or explain to people) as the simple order of magnitude change afforded by the "D" scaling method.

No matter which packing method was employed, a proper GRIB decoding program, that took account of the transmitted values of both "D" and "E", would return the correct unpacked numbers, regardless of which packing method was employed. It would be transparent to the user except for the questions of precision outlined above. For further details we refer to a document located at the following web address:
<ftp://ftp.ncep.noaa.gov/pub/nws/nmc/docs/gribed1/>.

Appendix D: Propagation Area in the Neutral Atmosphere

Objectives: To determine the propagation area in the neutral atmosphere.

Input Parameters:

1. The radius of the Earth denoted by R_e .
2. The local curvature radius, R_c
3. The apodization zone, Dya .
4. The parameters H_{atm} and H_{max} representing the height of the atmosphere and the maximum height for occultations in the neutral atmosphere. Good approximate values for H_{atm} and H_{max} are 130 km and 60 km, respectively.

Output Parameters:

1. The propagation area in the neutral atmosphere limits defined by the four parameters X_{min} , X_{max} , Y_{min} and Y_{max} .

Algorithm

The four parameters X_{min} , X_{max} , Y_{min} and Y_{max} defining the propagation area are found using the following equations. The two parameters X_{min} and Y_{max} are defined as the X-value of the field entering the atmosphere and the maximum Y-value of the occultation. The parameters are given by

$$X_{min} = -\sqrt{(R_e + H_{atm})^2 - R_e^2} \quad (D-1)$$

$$Y_{max} = H_{max} + Dya \quad (D-2)$$

It can be seen from geometrical considerations (Figure 2.10) and ray tracing that the area limiting parameters X_{max} and Y_{min} are given by

$$X_{max} = \vec{E}_x * (\vec{XN} - ER\vec{LC}) \quad (D-3)$$

$$Y_{min} = \vec{E}_y * (\vec{XN} - ER\vec{LC}) - R_c - Dya \quad (D-4)$$

\vec{XN} gives the direction towards the LEO satellite of the ray with the highest X-and smallest Y-values. This is found by ray tracing through the atmosphere.

Appendix E: Forward Propagation from the GPS Satellite to the First Screen

Objectives: To forward propagate the complex field from the GPS satellite to the first screen.

Input Parameters:

1. \vec{R} radius vector from the GPS satellite to a point on the 1. screen where the field is evaluated and a scaling factor E_0 .

Output Parameters:

1. The complex field for the two frequencies along the first screen.

Algorithm

Spherical Wave propagation in vacuum

The wave propagation from the GPS satellite to the 1. screen is assumed to be given by a spherical wave of the form

$$E(\vec{R}) = E_0 \frac{\exp(ik_T |\vec{R}|)}{\sqrt{|\vec{R}|}} \quad (\text{E-1})$$

where \vec{R} is the radius vector from the GPS satellite to the point on the 1. screen at which the field is evaluated. k_T is the free space wave number for either of the two frequencies L1 and L2. E_0 and is a scaling constant given by

$$E_0 = (X_{\min} - X_{GPS})^{1/2} \quad (\text{E-2})$$

X_{\min} is discussed in Appendix D and X_{GPS} is the last of the x-coordinates in the GPS orbit.

Appendix F: Forward Propagation from the First to the Last Screen

Objectives: To forward propagate the complex field from the first to the last phase screen.

Input Parameters:

The complex field along the first screen is calculated using the following input:

1. The complex field for the L1 and L2 frequencies at the first screen.

Output Parameters:

1. The complex field for the L1 and L2 frequencies at the last screen

Algorithm

Wave propagation in the neutral atmosphere using the thin screen approximation

The fields on the screens are known as functions of distances along the screens. The number of points in which the field is known is N . By applying the Fourier transform to this signal one represents the signal in terms of spatial frequencies. If the length of the screens is L then the distance between two samples, called Delta, is given by $\Delta=L/N$.

The Fourier transform of the electromagnetic field, U , is calculated using the following equation

$$\tilde{U}(p_i) = \text{FFT}(U) = \sum_{l=0}^{N-1} e^{-j2\pi li/N} U(l) \quad (\text{F-1})$$

The equation shows that we have N plane waves that propagate along the Y-axis. Let the distance between the screens be Dx . The expression for the field will be determined below.

The number of plane waves NP is given by

$$NP = \text{Min}\left(\frac{N}{2}, \text{INT}\left(\frac{Lk}{2\pi}\right)\right) \quad (\text{F-2})$$

The total number of plane waves is $2*NP$. $\text{INT}(\frac{Lk}{2\pi})$ is the number of waves along the screen with the length, L . In the following equations x_0 denotes the position of the screen at which the field is known, whereas x_1 indicates the position of the screen at which the field is calculated.

For every spatial frequency the following temporary field is calculated

$$\tilde{U}_{\text{tmp}}(x_1, p_i) = e^{j\sqrt{k^2 - (\frac{2\pi}{L}i)^2} Dx} \tilde{U}(x_0, p_i) \quad (\text{F-3})$$

Here $p_i = \frac{2\pi}{L}i$ represents the spatial frequencies (wave vector) along the Y-axis. k is the total length of the wave vector in the medium. Therefore $\sqrt{k^2 - (\frac{2\pi}{L}i)^2}$ must be the wave vector along the X-axis. Applying the inverse Fourier transform to field in the equation above and multiplying by an exponential factor yields the field along the next screen.

$$U(x_1, y) = (e^{jk \cdot Dx \cdot (n-1)}) \text{Fourier}^{-1} \{ \tilde{U}_{\text{tmp}}(x_1, p) \} \quad (\text{F-4})$$

The resolution, i.e., the distance between the points on the screen, is determined from the following equation

$$\Delta y \leq \frac{\lambda}{4\sin(\epsilon_{\text{max}})} \quad (\text{F-5})$$

where ϵ_{max} is the maximum propagation angle from the horizon to be represented without distortion. For the spherical wave this opening angle can be calculated as

$$\epsilon_{\text{max}} = \max(\text{abs}(Y_{\text{max}}/X_{\text{GPS}}), \text{abs}(Y_{\text{min}}/X_{\text{GPS}})) \quad (\text{F-6})$$

The minimum number of point on the screen is

$$N_{\text{min}} = \frac{4L}{\lambda} \sin(\epsilon_{\text{max}}) \quad (\text{F-7})$$

There is also an upper limit for the number of points on the screen given by:

$$N_{\text{max}} = \frac{4L}{\lambda} \sin(\alpha_{\text{max}}) \quad (\text{F-8})$$

where α_{max} is the maximum bending angle found from ray-tracing. If the Doppler phase is greater than $\pi/2$ and the current number is less than N_{max} , then it is necessary to double the number of points on the next screen.

The electro-magnetic field in the equation above must be apodized in order to satisfy the electromagnetic boundary conditions on the screens. The apodization zone is found on the top and bottom of all of the screens in the neutral atmosphere and the field here is given by

$$U_{new} = e^{-((Y-YU)/(Dya/3))^2} U_{old} \text{ for } Y > YU = Y_{max} - 0.75Dya \quad (\text{F-9})$$

and

$$U_{new} = e^{-((YD-Y)/(Dya/3))^2} U_{old} \text{ for } Y < YD = Y_{min} + 0.75Dya \quad (\text{F-10})$$

where Y gives us the position on the screen and Y_{max} and Y_{min} are the Y -coordinate for the largest and smallest position on the screen. Dya is the size of the apodization area on the top and button of the screen. The value of this parameter should be around 5 km. $U_{new}(Y)$ and $U_{old}(Y)$ is the value of the complex field before and after the apodization of the field.

Appendix G: Algorithm for Propagation between Two Non-Parallel Lines

Objectives: To forward propagate the complex field from the last screen to the LEO orbit.

Input Parameters:

The complex field along the LEO orbit is calculated using the following input: It has been assumed in the algorithm, that all data are organized as in a setting occultation, i.e., the first sample is the top most sample.

1. The position vectors \vec{x} of the LEO satellite orbit $(x_L(t), y_L(t))$ in the Unmoving GPS Coordinate System.
2. The coordinate vectors \vec{y} along the last screen (x_S, y_S) .
3. The complex field E_0 along the last screen.

Output Parameters:

1. The complex field E along the LEO orbit.

Constants:

1. The GPS frequencies f_1 and f_2 .
2. The wave number in free space $k_1 = 2\pi / \lambda_1$ and $k_2 = 2\pi / \lambda_2$.

Algorithm

Calculation of the Forward-Propagation Integral

If the electric field, $E_0(\vec{y})$, is known all over the last screen S , the electric field $E(\vec{x})$ can then be found at a given point \vec{x} along the LEO orbit using the following equation.

$$E(\vec{x}) = \left(\frac{k_T}{2\pi} \right)^{1/2} \int_S E_0(\vec{y}) \cos \varphi_{xy} \frac{\exp(ik_T |\vec{x} - \vec{y}| - i\pi/4)}{|\vec{x} - \vec{y}|^{1/2}} dS_y \quad (\text{G-1})$$

In (G-1) k_T is the vacuum wave number for one of the two frequencies L1 and L2. φ_{xy} is the angle between the normal \vec{n}_y to S and the vector $\vec{x} - \vec{y}$ and is given by

$$\cos \varphi_{xy} = \frac{(x_L - x_S)}{\sqrt{(x_L - x_S)^2 + (y_L - y_S)^2}} \quad (\text{G-2})$$

where index L and S are the symbols used for the LEO position and the last screen. The integral (G-1) can be evaluated using a standard numerical integration routine. The integration is performed over a certain part of the last screen determined by the stationary phase technique. For every point, (x_L, y_L) on the LEO orbit the virtual phases (VP's) are calculated on the last phase screen using the following equation

$$VP(i) = k_i * ((x - x_S(i))^2 + (y - y_S(i))^2)^{1/2} + PS(i) \quad (G-3)$$

where PS is the calculated phase on every point (x_S, y_S) on the last screen. The index, i , corresponds to samples on the last screen. The stationary phase is then the smallest value of the virtual phase given by $SP = \min(VP)$.

The (G-1) integral must be solved for every point along the LEO orbit. If the computation time is an important concern then the Fresnel integral can be solved using the stationary phase technique. The standard unwrapping routine, given by the equations below, must be used to calculate the accumulated phase from the phase of the complex signal.

$$Phase(i) = Phase(i-1) + \text{modulo}(Phase(i) - Phase(i-1) + \pi, 2 * \pi) - \pi \quad (G-4)$$

This must be performed for all the samples, i , in the phase array.

The integration limits are deduced by the stationary phase point plus/minus the distances corresponding to a phase change of $10 * \pi$ (DyU and DyL). In general, DyU and DyL are not equal. The diffraction integral can therefore be written as

$$E(\vec{x}) = \left(\frac{k_T}{2\pi} \right)^{1/2} \int_{y_{SP} - DyL}^{y_{SP} + DyU} E_0(\vec{y}) \cos \varphi_{xy} \frac{\exp(ik_T |\vec{x} - \vec{y}| - i\pi/4)}{|\vec{x} - \vec{y}|^{1/2}} dS \quad (G-5)$$

where y_{SP} is the y-coordinate of the stationary phase point.

If the stationary phase point is above or below the last screen, i.e., $y_{SP} > y_{max}$ or $y_{SP} < y_{min}$ the point on the LEO orbit in consideration, it is discarded. If the stationary phase point is within the range of the screen, but one of the integration limits, as described above, extends outside the screen, then the phase is extrapolated linearly and the amplitude is considered constant.

Appendix H: Difference and relative difference plots

In this section difference plots and relative difference plots between the bending angle model and the bending angles calculated using the Radio Holographic/Back propagation methods are presented in the eight figures below. These plots show the combined error of the WOP and the respective retrieval routines.

Medium multipath level ($B=10$)

The four figures below show the difference/relative difference plots in case of a medium multipath level.

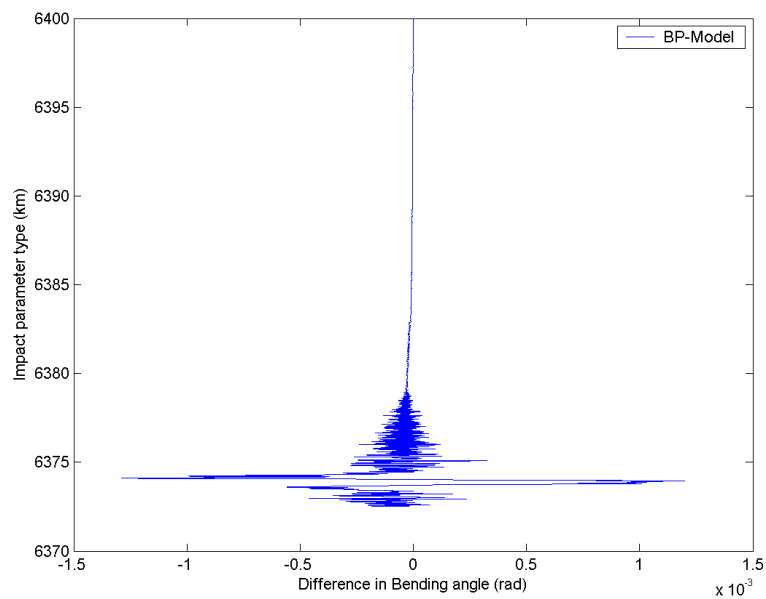


Figure H.0-1: The plot shows (for $B=10$) the difference between the back propagation bending angle and the model bending angle as a function of impact parameter.

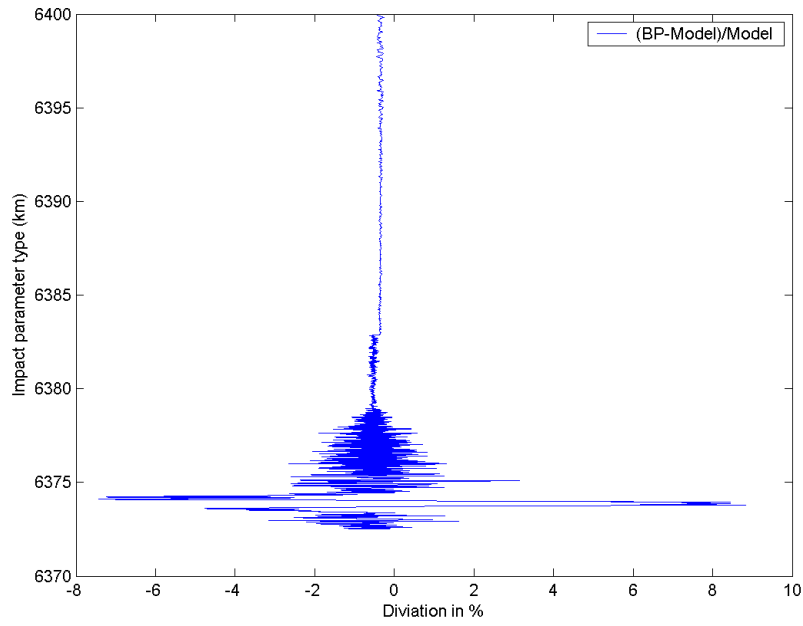


Figure H.0-2: The plot shows (for B=10) the relative difference between the back propagation bending angle and the model bending angle as a function of impact parameter.

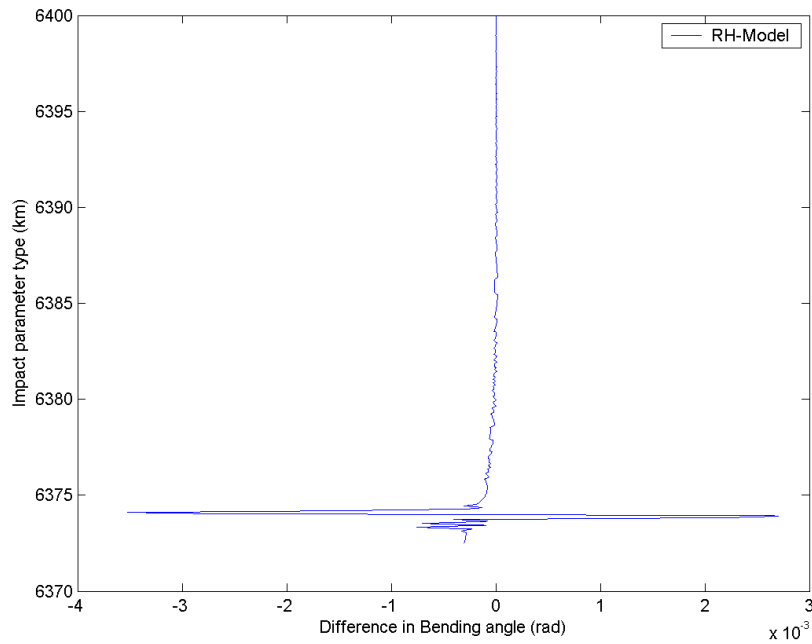


Figure H.0-3: The plot shows (for B=10) the difference between the radio holographic bending angle and the model bending angle as a function of impact parameter.

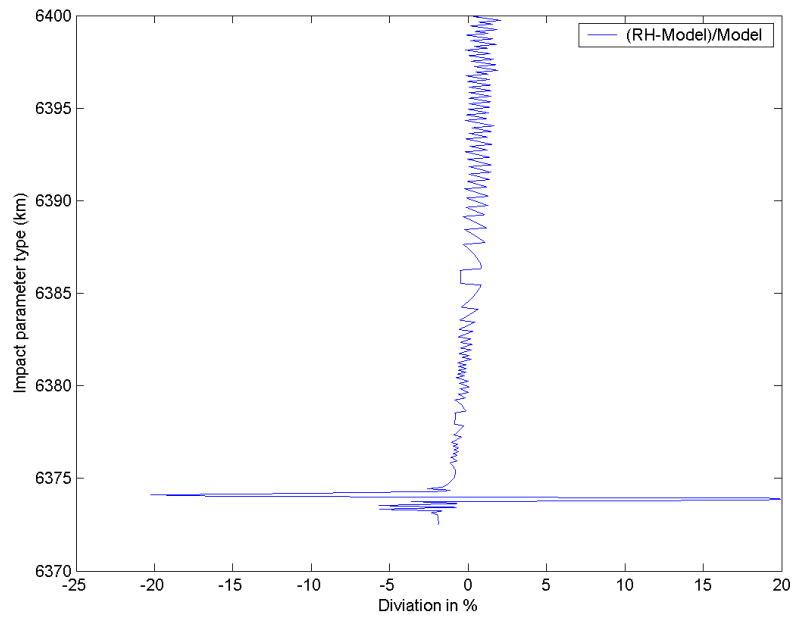


Figure H.0-4: The plot shows (for $B=10$) the relative difference between the radio holographic bending angle and the model bending angle as a function of impact parameter.

High multipath level ($B=20$)

The four figures below show the difference/relative difference plots in case of a high multipath level.

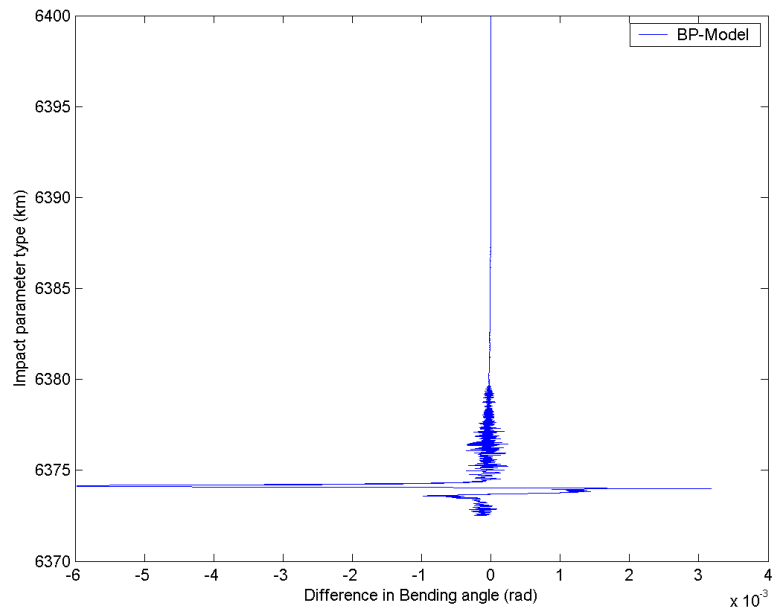


Figure H.0-5: The plot shows (for $B=20$) the difference between the back propagation bending angle and the model bending angle as a function of impact parameter.

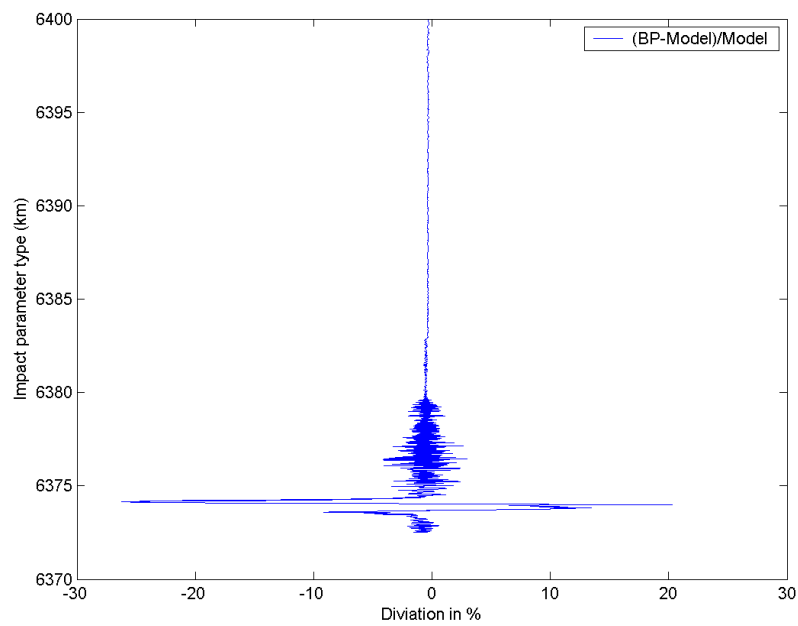


Figure H.0-6: The plot shows (for $B=20$) the relative difference between the back propagation bending angle and the model bending angle as a function of impact parameter.

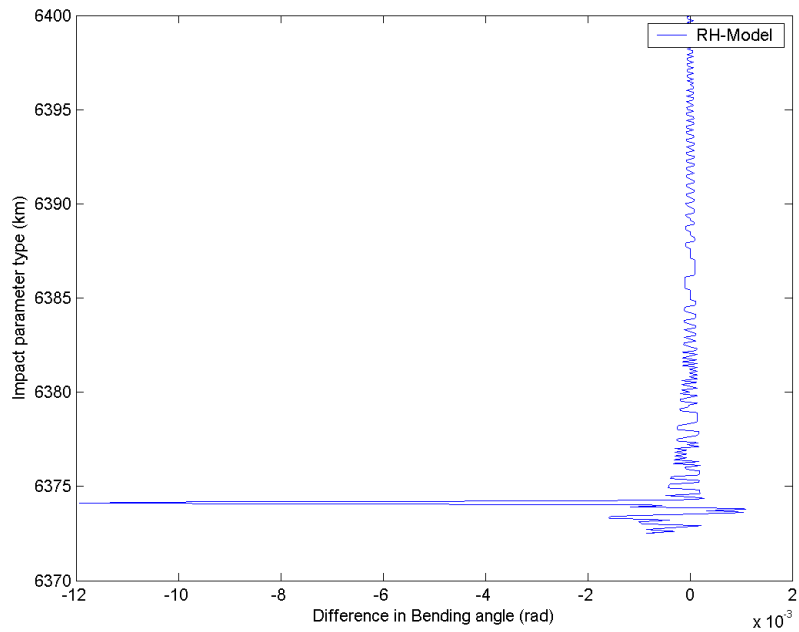


Figure H.0-7: The plot shows (for B=20) the difference between the radio holographic bending angle and the model bending angle as a function of impact parameter.

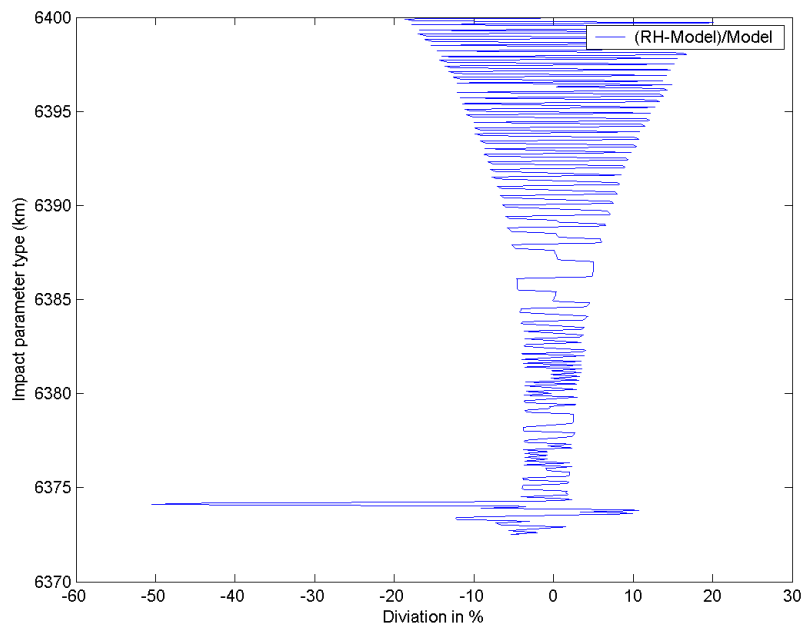


Figure H.0-8: The plot shows (for B=20) the relative difference between the radio holographic bending angle and the model bending angle as a function of impact parameter.

7 References

Chew, W.C., *Waves and Fields in Inhomogeneous Media*, IEEE Press series on Electromagnetic Waves, IEEE Press, New York, 1995.

Fjeldbo, G., J. Kliore, and V.R. Eshleman, *The neutral atmosphere of Venus as studied with the Mariner V radio occultation experiments*, The Astronomical Journal, 76, 123-140, 1971.

Gorbunov, M.E., A.S. Gurvich and L. Bengtsson, *Advanced algorithms of inversion of GPS/MET satellite data and their application to reconstruction of temperature and humidity*, Tech. Rep. 211, Max-Planck-Institute for Meteorology, Hamburg, 1996.

Gorbunov, M.E., and A.S. Gurvich, *Microlab-1 experiment: Multipath effects in the lower troposphere*, Journal of Geophysical Research, 103, 13,819-13826, 1998a.

Gorbunov, M.E., and A.S. Gurvich, *Algorithms of inversion of Microlab-1 satellite data including effects of multipath propagation*, Int. J. Remote Sensing, 19, 2283-2300, 1998b.

Harris, F.J., *On the use of windows for harmonic analysis with the discrete Fourier transform*, Proceedings of the IEEE, 66, p. 51-83, 1978.

International Telecommunication Union, *Propagation in non-ionized media*, J. Comp. Phys, vol. 41, p. 115-131, 1981.

Karayel, E.T., and David P. Hinson, *Sub-Fresnel-scale vertical resolution in atmospheric profiles from radio occultation*, Radio Science, 32, 411-423, 1997.

Kornbluh, L., M. Gorbunov, and L. Bengtsson, *Work package 4, Applications to Climatology and Atmospheric Process Studies*, in ESTEC Radio Occultation Studies 1996-98, TERMA Elektronik AS, Denmark, 1998.

Kuttler, J.R. and Dockery, G.D. *Theoretical description of the parabolic approximation/Fourier split-step method of representing electromagnetic propagation in the troposphere*, Radio Science 26 #2, p.381-393, 1991.

Jensen, A.S., Lohmann, M., Benzon, H.-H., Nielsen, A.S. *Full Spectrum Inversion of Radio Occultation Signals*, To appear in Radio Science.

Levy, M., *Parabolic equation methods for electromagnetic wave propagation*, The Institution of Electrical Engineers, 2000.

Marouf, E.A., G.L. Tyler, and P.A. Rosen, *Profiling Saturn's rings by radio occultation*, Icarus, 68, 120-166, 1986.

McIlveen, R., *Basic Meteorology a Physical Outline*, Van Nostrand Reinhold, Berkshire, England, 1986.

Meincke, M.D., Inversion Methods for Atmospheric Profiling with GPS Occultations, Scientific Report 99-11, DMI, Copenhagen, Denmark, 1999.

Meincke, M.D., Analysis and Definition of Algorithms for Atmospheric Diffraction Effects, DMI Scientific Report, March 2000.

Melbourne, W.E., E.S. Davis, C.B. Duncan, G.A. Hajj, K.R. Hardy, E.R. Kursinski, T.K. Meehan, L.E. Young, and T.P. Yunck, *The Application of Spaceborne GPS to atmospheric limb sounding and global change monitoring*, JPL Publication 94-18, JPL, Pasadena, CA, USA, 1994.

Mortensen, M.D. *The Back-Propagation Method for Inversion of Radio occultation Data*. Scientific Report 98-14, DMI, Copenhagen, Denmark, 1998.

Mortensen, M.D., and P. Høeg, *Inversion of GPS occultation measurements using Fresnel diffraction theory*, Geophysical Research Letters, 25, 2441-2444, 1998a.

Mortensen, M.D., and Høeg, P., *Resolution properties in atmospheric profiling with GPS*, DMI Scientific Report 98-4, DMI, Copenhagen, Denmark, 1998b.

Mortensen, M.D., R. Linfield, and E.R. Kursinski, *Vertical resolution approaching 100 m for GPS occultations of the Earth's atmosphere*, Radio Science, 34, 1475-1484, 1999.

Rocken, C., R.A. Anthes, M. Exner, D. Hunt, S. Sokolovskiy, R. Ware, M. Gorbunov, W. Schreiner, D. Feng, B. Herman, Y.H. Kuo and X. Zou, *Analysis and validation of GPS/MET data in the neutral atmosphere*, Journal of Geophysical Research, 102, 29,849-29,866, 1997.

Roeckner, E., 1995: *Parameterization of cloud radiative properties in the ECHAM4 model*. In: Proceedings of the WCRP Workshop on "Cloud Microphysics Parameterizations in Global Atmospheric Circulation Models", May 23-25, 1995, Kananaskis, Alberta, Canada, WCRP Report No. 90, 105-116, WMO-TD-No. 713.

Syndergaard, S., *Modelling the impact of the Earth's oblateness on the retrieval of temperature and pressure profiles from limb sounding*, Journal of Atmospheric and Solar-Terrestrial Physics, 60, 171-180, 1998.

Tatarski, V.I., *Wave Propagation in a Turbulent Medium*, Dover Publications, Inc., New York, N. Y., p. 299, 1967.

DANISH METEOROLOGICAL INSTITUTE

Scientific Reports

Scientific reports from the Danish Meteorological institute cover a variety of geophysical fields, i.e., meteorology (including climatology), oceanography, subjects on air and sea pollution, geomagnetism, solar-terrestrial physics, and physics of the middle and upper atmosphere.

Reports in the series within the last five years:

No. 98-1

Niels Woetman Nielsen, Bjarne Amstrup, Jess U. Jørgensen:

HIRLAM 2.5 parallel tests at DMI: sensitivity to type of schemes for turbulence, moist processes and advection

No. 98-2

Per Høeg, Georg Bergeton Larsen, Hans-Henrik Benzon, Stig Syndergaard, Mette Dahl

Mortensen: The GPSOS project Algorithm functional design and analysis of ionosphere, stratosphere and troposphere observations

No. 98-3

Mette Dahl Mortensen, Per Høeg:

Satellite atmosphere profiling retrieval in a nonlinear troposphere Previously entitled: Limitations induced by Multipath

No. 98-4

Mette Dahl Mortensen, Per Høeg:

Resolution properties in atmospheric profiling with GPS

No. 98-5

R.S. Gill and M. K. Rosengren

Evaluation of the Radarsat imagery for the operational mapping of sea ice around Greenland in 1997

No. 98-6

R.S. Gill, H.H. Valeur, P. Nielsen and K.Q. Hansen: Using ERS SAR images in the operational mapping of sea ice in the Greenland waters: final report for ESA-ESRIN's: pilot projekt no. PP2.PP2.DK2 and 2nd announcement of

opportunity for the exploitation of ERS data projekt No. AO2..DK 102

No. 98-7

Per Høeg et al.: GPS Atmosphere profiling methods and error assessments

No. 98-8

H. Svensmark, N. Woetmann Nielsen and A.M. Sempreviva: Large scale soft and hard turbulent states of the atmosphere

No. 98-9

Philippe Lopez, Eigil Kaas and Annette Guldborg: The full particle-in-cell advection scheme in spherical geometry

No. 98-10

H. Svensmark: Influence of cosmic rays on earth's climate

No. 98-11

Peter Thejll and Henrik Svensmark: Notes on the method of normalized multivariate regression

No. 98-12

K. Lassen: Extent of sea ice in the Greenland Sea 1877-1997: an extension of DMI Scientific Report 97-5

No. 98-13

Niels Larsen, Alberto Adriani and Guido Donfrancesco: Microphysical analysis of polar stratospheric clouds observed by lidar at McMurdo, Antarctica

No.98-14

Mette Dahl Mortensen: The back-propagation method for inversion of radio occultation data

No. 98-15

Xiang-Yu Huang: Variational analysis using spatial filters

No. 99-1

Henrik Feddersen: Project on prediction of climate variations on seasonal to interannual timescales (PROVOST) EU contract ENV4-CT95-0109: DMI contribution to the final report: Statistical analysis and post-processing of uncoupled PROVOST simulations

No. 99-2

Wilhelm May: A time-slice experiment with the ECHAM4 A-GCM at high resolution: the experimental design and the assessment of climate change as compared to a greenhouse gas experiment with ECHAM4/OPYC at low resolution

No. 99-3

Niels Larsen et al.: European stratospheric monitoring stations in the Arctic II: CEC Environment and Climate Programme Contract ENV4-CT95-0136. DMI Contributions to the project

No. 99-4

Alexander Baklanov: Parameterisation of the deposition processes and radioactive decay: a review and some preliminary results with the DERMA model

No. 99-5

Mette Dahl Mortensen: Non-linear high resolution inversion of radio occultation data

No. 99-6

Stig Syndergaard: Retrieval analysis and methodologies in atmospheric limb sounding using the GNSS radio occultation technique

No. 99-7

Jun She, Jacob Woge Nielsen: Operational wave forecasts over the Baltic and North Sea

No. 99-8

Henrik Feddersen: Monthly temperature forecasts for Denmark - statistical or dynamical?

No. 99-9

P. Thejll, K. Lassen: Solar forcing of the Northern hemisphere air temperature: new data

No. 99-10

Torben Stockflet Jørgensen, Aksel Walløe Hansen: Comment on "Variation of cosmic ray flux and global coverage - a missing link in solar-climate relationships" by Henrik Svensmark and Eigil Friis-Christensen

No. 99-11

Mette Dahl Meincke: Inversion methods for atmospheric profiling with GPS occultations

No. 99-12

Hans-Henrik Benzon; Laust Olsen; Per Høeg: Simulations of current density measurements with a Faraday Current Meter and a magnetometer

No. 00-01

Per Høeg; G. Leppelmeier: ACE - Atmosphere Climate Experiment

No. 00-02

Per Høeg: FACE-IT: Field-Aligned Current Experiment in the Ionosphere and Thermosphere

No. 00-03

Allan Gross: Surface ozone and tropospheric chemistry with applications to regional air quality modeling. PhD thesis

No. 00-04

Henrik Vedel: Conversion of WGS84 geometric heights to NWP model HIRLAM geopotential heights

No. 00-05

Jérôme Chenevez: Advection experiments with DMI-Hirlam-Tracer

No. 00-06

Niels Larsen: Polar stratospheric clouds micro-physical and optical models

- No. 00-07
Alix Rasmussen: "Uncertainty of meteorological parameters from DMI-HIRLAM"
- No. 00-08
A.L. Morozova: Solar activity and Earth's weather. Effect of the forced atmospheric transparency changes on the troposphere temperature profile studied with atmospheric models
- No. 00-09
Niels Larsen, Bjørn M. Knudsen, Michael Gauss, Giovanni Pitari: Effects from high-speed civil traffic aircraft emissions on polar stratospheric clouds
- No. 00-10
Søren Andersen: Evaluation of SSM/I sea ice algorithms for use in the SAF on ocean and sea ice, July 2000
- No. 00-11
Claus Petersen, Niels Woetmann Nielsen: Diagnosis of visibility in DMI-HIRLAM
- No. 00-12
Erik Buch: A monograph on the physical oceanography of the Greenland waters
- No. 00-13
M. Steffensen: Stability indices as Indicators of lightning and thunder
- No. 00-14
Bjarne Amstrup, Kristian S. Mogensen, Xiang-Yu Huang: Use of GPS observations in an optimum interpolation based data assimilation system
- No. 00-15
Mads Hvid Nielsen: Dynamisk beskrivelse og hydrografisk klassifikation af den jyske kyststrøm
- No. 00-16
Kristian S. Mogensen, Jess U. Jørgensen, Bjarne Amstrup, Xiaohua Yang and Xiang-Yu Huang: Towards an operational implementation of HIRLAM 3D-VAR at DMI
- No. 00-17
Sattler, Kai; Huang, Xiang-Yu: Structure function characteristics for 2 meter temperature and relative humidity in different horizontal resolutions
- No. 00-18
Niels Larsen, Ib Steen Mikkelsen, Bjørn M. Knudsen m.fl.: In-situ analysis of aerosols and gases in the polar stratosphere. A contribution to THESEO. Environment and climate research programme. Contract no. ENV4-CT97-0523. Final report
- No. 00-19
Amstrup, Bjarne: EUCOS observing system experiments with the DMI HIRLAM optimum interpolation analysis and forecasting system
- No. 01-01
V.O. Papitashvili, L.I. Gromova, V.A. Popov and O. Rasmussen: Northern polar cap magnetic activity index PCN: Effective area, universal time, seasonal, and solar cycle variations
- No. 01-02
M.E. Gorbunov: Radiological methods for processing radio occultation data in multipath regions
- No. 01-03
Niels Woetmann Nielsen; Claus Petersen: Calculation of wind gusts in DMI-HIRLAM
- No. 01-04
Vladimir Penenko; Alexander Baklanov: Methods of sensitivity theory and inverse modeling for estimation of source parameter and risk/vulnerability areas
- No. 01-05
Sergej Zilitinkevich; Alexander Baklanov; Jutta Rost; Ann-Sofi Smedman, Vasilij Lykosov and Pierluigi Calanca: Diagnostic and prognostic equations for the depth of the stably stratified Ekman boundary layer

No. 01-06

Bjarne Amstrup: Impact of ATOVS AMSU-A radiance data in the DMI-HIRLAM 3D-Var analysis and forecasting system

No. 01-07

Sergej Zilitinkevich; Alexander Baklanov: Calculation of the height of stable boundary layers in operational models

No. 01-08

Vibeke Huess: Sea level variations in the North Sea – from tide gauges, altimetry and modelling

No. 01-09

Alexander Baklanov and Alexander Mahura: Atmospheric transport pathways, vulnerability and possible accidental consequences from nuclear risk sites: methodology for probabilistic atmospheric studies

No. 02-01

Bent Hansen Sass and Claus Petersen: Short range atmospheric forecasts using a nudging procedure to combine analyses of cloud and precipitation with a numerical forecast model

No. 02-02

Erik Buch: Present oceanographic conditions in Greenland waters

No. 02-03

Bjørn M. Knudsen, Signe B. Andersen and Allan Gross: Contribution of the Danish Meteorological Institute to the final report of SAMMOA. CEC contract EVK2-1999-00315: Spring-to-autumn measurements and modelling of ozone and active species

No. 02-04

Nicolai Kliem: Numerical ocean and sea ice modelling: the area around Cape Farewell (Ph.D. thesis)

No. 02-05

Niels Woetmann Nielsen: The structure and dynamics of the atmospheric boundary layer

No. 02-06

Arne Skov Jensen, Hans-Henrik Benzon and Martin S. Lohmann: A new high resolution method for processing radio occultation data

No. 02-07

Per Høeg and Gottfried Kirchengast: ACE+: Atmosphere and Climate Explorer

No. 02-08

Rashpal Gill: SAR surface cover classification using distribution matching

No. 02-09

Kai Sattler, Jun She, Bent Hansen Sass, Leif Laursen, Lars Landberg, Morten Nielsen og Henning S. Christensen: Enhanced description of the wind climate in Denmark for determination of wind resources: final report for 1363/00-0020: Supported by the Danish Energy Authority

No. 02-10

Michael E. Gorbunov and Kent B. Lauritsen: Canonical transform methods for radio occultation data

No. 02-11

Kent B. Lauritsen and Martin S. Lohmann: Unfolding of radio occultation multipath behavior using phase models

No. 02-12

Rashpal Gill: SAR ice classification using fuzzy screening method

No. 02-13

Kai Sattler: Precipitation hindcasts of historical flood events

No. 02-14

Tina Christensen: Energetic electron precipitation studied by atmospheric x-rays

No. 02-15

Alexander Mahura and Alexander Baklanov: Probabilistic analysis of atmospheric transport patterns from nuclear risk sites in Euro-Arctic Region

No. 02-16

A. Baklanov, A. Mahura, J.H. Sørensen, O. Rigina, R. Bergman:
Methodology for risk analysis based on atmospheric dispersion modelling from nuclear risk sites

No. 02-17

A. Mahura, A. Baklanov, J.H. Sørensen, F. Parker, F. Novikov K. Brown, K. Compton:
Probabilistic analysis of atmospheric transport and deposition patterns from nuclear risk sites in russian far east